

Chapter 2

Terahertz and Infrared Quantum Photodetectors

2.1 Introduction

The importance and the application vastity of terahertz and infrared photodetectors are clear for every one working in this field. Infrared photodetectors are interesting components in optical communications, thermal imaging and sensor networking. Recently infrared photodetectors have been the focus of much attention due to its potential use in far-infrared imaging as well as room temperature operation, which is of interest from user's point of view. Conventionally all objects radiate most of its energy in the form of infrared and terahertz waves, for observing objects and physical activity in dark conditions one must monitor the infrared spectra. It is usually customary to use the 3–5 μm infrared window in military applications, 8–15 μm window in thermal imaging and >20 μm in THz applications such as medical diagnostics. More study is done on finding proper material for detecting the infrared spectrum. However the detection of long-wavelength infrared (e.g. 10 μm) radiation requires a small gap ($E_g \approx 0.1$ eV). Such small-bandgap materials are well-known to be more difficult to grow, process, and fabricate into devices than are larger bandgap semiconductors [1]. This problem is more critical in THz wavelengths in a manner that it is actually impossible to detect THz radiations via interband optical transitions. Intersubband transitions are a suitable alternative to cover the infrared and THz spectra. On these lines to remove the present problems, improve the detecting parameters and for integrating it with other optoelectronic devices, optimizing the trade-off between Responsivity and Detectivity, spectra engineering and obtaining to suitable detecting parameters at room temperature, photodetector structures are developed from bulk to quantum wells (QWIP) and dots (QDIP).

In this chapter we study different structures of QW and QD terahertz-infrared photodetectors. The main aim in design of all structures is to overcome the challenging subjects in long-wavelength signal detection. [Section 2.2](#) covers the general concepts and definitions about detector principles. [Section 2.3](#) discusses about the

terahertz and infrared quantum cascade detectors (QCDs) and at the end of this section two novel dual-wavelengths photodetectors will be presented. In [Sect. 2.4](#), a terahertz quantum well photodetector based on two-photon absorption will be introduced. [Section 2.5](#) gives the brief review on quantum dot long-wavelength photodetectors and also a new quantum dot terahertz photodetector based on the concept of defect will be proposed. EIT-based photodetection and possible structures for long-wavelength photodetector based on physical electromagnetically induced transparency phenomena (EIT) will be introduced in [Sect. 2.6](#).

2.2 Detector Principles

Detecting light means generating an electrical signal (current or voltage) as function of the incident light intensity. The incident photons in a photodetector generate electrons. The number of electrons passing through the device is relevant to the number of photons. This relevance is “the overall quantum efficiency” and expressed as [2]:

$$\eta_{\text{tot}} = \frac{N_e}{N_p} \quad (2.1)$$

Since determining the number of electrons and photons is practically almost impossible, measuring the ratio of the output electrical current per incident optical power which is called the responsivity \mathfrak{R} parameter, is preferred:

$$\mathfrak{R} = \frac{I}{P_i} = \frac{\lambda e N_e}{hc N_p} = \frac{\lambda e}{hc} \eta_{\text{tot}} \quad (2.2)$$

where e , h , c and λ are the electron charge, the Planck’s constant, the speed of light and the wavelength of the incident light, respectively. Three probabilities are involved in determining the overall quantum efficiency: the absorption probability of an electron passing through the active region that is defined as the following quantum efficiency format:

$$\eta_{\text{abs}} = 1 - e^{-\alpha d} \quad (2.3)$$

where α is the absorption coefficient and d the thickness and the escape probability, p_e which is the fraction of electrons excited by absorbing incident photons, contributing to electrical current- and the capture probability, p_c are expressed in the gain format (like the photoconductive gain in QWIP):

$$g = \frac{p_e}{N p_c} \quad (2.4)$$

where N is the number of periods in a multiple period QWIP structure.

2.2.1 Noise Affects

The photodetection process is inevitably affected by noise. A part of photodetector output current is correlated to the intensity of the input light (signal current) but the other part of this current has no correlation with the incoming light. This is defined as “Signal-to-noise-ratio” S/N :

$$S/N = \frac{I_{\text{signal}}}{I_{\text{noise}}} \quad (2.5)$$

The power of the input light needed to produce the same signal strength as produced by noise sources is defined as noise equivalent power (NEP):

$$\text{NEP} = \frac{P}{S/N} \quad (I_{\text{noise}} = \Re \cdot \text{NEP}) \quad (2.6)$$

Need to mention that NEP is directly proportional to $\sqrt{A\Delta f}$, which is unrelated to the material properties. Therefore it is more convenient to compare different detectors with the quantity:

$$D^* = \frac{\sqrt{A\Delta f}}{\text{NEP}} \quad (2.7)$$

which is defined as the detectivity. A larger detectivity means a smaller NEP and hence a more sensitive detector. In above equation A is the detector’s surface and Δf the electrical bandwidth. Inserting Eq. 2.6 gives:

$$D^* = \frac{\Re \sqrt{A\Delta f}}{I_{\text{noise}}} \quad (2.8)$$

The normalized detectivity is expressed in units of “Jones” ($\text{cm} \sqrt{\text{Hz}}/\text{W}$). The important origins of noise current in a photodetector are: Johnson noise, $1/f$ noise and shot noise due to current flowing through a device. The shot noise is corresponded to dark current noise (without illumination) or photon noise. The $1/f$ noise becomes unimportant in photodetectors if measuring characteristic frequencies are set high enough. In a resistive device, the thermal motion of electrons makes Johnson noise:

$$P_{\text{noise}} = 4k_B T \cdot \Delta f \quad (2.9)$$

For an ohmic device, the current and voltage noise spectral densities are:

$$i_{\text{noise},J}^2 = \frac{4k_B T \Delta f}{R}, \quad v_{\text{noise},J}^2 = 4k_B T R \Delta f \quad (2.10)$$

where R is the device resistance. For Johnson noise limited case, the detectivity is:

$$D_J^*(\nu) = \Re(\nu) \sqrt{\frac{R_0 A}{4k_B T}} \quad (2.11)$$

In QWIPs, dark current noise and photon noise are rather important than Johnson noise. In QCDs, dark current is absent so Johnson noise is dominant at high temperatures.

The generation-recombination noise mean square current that dark current I_{dark} makes is described by:

$$i_{\text{noise,dark}}^2 = 4eg_{\text{noise}} I_{\text{dark}} \Delta f \quad (2.12)$$

In the conventional photoconductors, there is almost no difference between noise gain g_{noise} and the photoconductive gain, but for QWIPs they are different. For the current limited case the detectivity can be described as:

$$D_{\text{dark}}^*(\nu) = \frac{\Re(\nu)}{\sqrt{ueg_{\text{noise}} J_{\text{dark}}}} \quad (2.13)$$

The background blackbody radiation generates a current, J_{BG} . This current produces noise as well as the dark current. The J_{BG} is given by:

$$J_{\text{BG}} = e \int \eta_{\text{tot}}(\lambda) \frac{d\Phi_{\text{BG}}(\lambda)}{d\lambda} d\lambda = e \int \eta_{\text{tot}}(\nu) \frac{d\Phi_{\text{BG}}(\nu)}{d\nu} d\nu \quad (2.14)$$

where $\frac{d\Phi_{\text{BG}}(\nu)}{d\nu}$ is the background photon flux spectral density. The blackbody emissivity is described as:

$$\begin{aligned} K(\nu, T_{\text{bb}}) d\nu &= \frac{2h\nu^3}{c^2} \frac{1}{e^{\frac{h\nu}{k_B T_{\text{bb}}}} - 1} d\nu \\ K(\lambda, T_{\text{bb}}) d\lambda &= \frac{2hc^2}{\lambda^5} \frac{1}{e^{\frac{hc}{\lambda k_B T_{\text{bb}}}} - 1} d\lambda \end{aligned} \quad (2.15)$$

by

$$\begin{aligned} h\nu \cdot \frac{d\Phi_{\text{BG}}(\nu)}{d\nu} &= \pi \sin^2 \frac{\Theta}{2} \cdot K(\nu, T_{\text{bb}}) \\ \frac{hc}{\lambda} \cdot \frac{d\Phi_{\text{BG}}(\lambda)}{d\lambda} &= \pi \sin^2 \frac{\Theta}{2} \cdot K(\lambda, T_{\text{bb}}) \end{aligned} \quad (2.16)$$

where T_{bb} is the blackbody temperature and Θ is a full cone of view (FOV) angle. Putting J_{dark} and (2.4) in (2.13), we obtain:

$$\begin{aligned} D_{\text{BLIP}}^*(\nu) &= \frac{\Re(\nu)}{\sqrt{ue^2 g_{\text{noise}} \int \eta(\nu') \frac{d\Phi_{\text{BG}}(\nu')}{d\nu'} d\nu'}} \\ &= \frac{\eta(\nu)}{h\nu \sqrt{ug_{\text{noise}} \int \eta(\nu') \frac{d\Phi_{\text{BG}}(\nu')}{d\nu'} d\nu'}} \end{aligned} \quad (2.17)$$

2.2.2 Background Limited IR Performance

Temperature has various effects on the different noise sources. *For* constant \mathfrak{R} temperature increases Johnson noise. Although increasing temperature decreases \mathfrak{R} in semiconductors, Johnson noise likewise increases with temperature. The effect of temperature on the dark current is the same then dark current noise also increases with temperature. The temperature has approximately no effect on photon noise until device temperature below the temperature of the environment.

In photodetectors, there exists a temperature, below which photon noise becomes dominant and above that the other noise sources have dominance. This temperature is indexed by background limited IR performance, T_{BLIP} . Since the different noise sources are independent thus the total detectivity is given by:

$$D_{\text{tot}}^* = \frac{\mathfrak{R}}{\sqrt{\frac{4k_{\text{B}}T}{R_0A} + ueg_{\text{noise}} \left(J_{\text{dark}} + e \int \eta(v') \frac{d\Phi_{\text{BG}}(v')}{dv'} dv' \right)}} \quad (2.18)$$

2.2.3 Quantum Cascade Detectors

In these detectors, there are two options for a light-induced electron: relaxing to ground state, or tunneling into the next period. Following equation is given for responsivity of this type of photodetectors:

$$R = \frac{\lambda e}{hc} \eta_{\text{abs}} \frac{p_{\text{e}}}{N} \quad (2.19)$$

In extracting above equation, the probability of the electron to be captured by the next-period ground state, p_{e} is assumed unity. The escape probability, p_{e} is determined by the fraction of light-induced electrons tunneling to the next period.

2.2.3.1 Model of the Electronic Transport Through QCD Structure and Derivation of the Essential Relations

The zero voltage resistance, R_0A (where R_0 is the resistance of the pixel and A the area of the pixel) is one of the important figures of merit in photovoltaic detectors to characterize the dark current in the absence of optical excitation. It has discussed that due to the well and barrier widths, only interactions between electrons and LO phonons should take into account [3]. On the other hand, due to sufficiently high energy difference between the energy levels, one can omit the effect of interaction between electrons and acoustical phonons [4] and also electron–electron interaction because of subband separation in the cascade structure which is in the range of LO phonon.

The transition rates are evaluated due to the interaction between electrons and optical phonons according to Ferreira and Bastard [5]. Starting from an initial state of wave vector k and energy E in the subband i , the transition rate $S_{ij}^{a,e}(E)$ towards the subband j (in S^{-1}) is obtained through the integration of a matrix element involving a standard electron–optical-phonon Hamiltonian. This integration involves all the possible final states of energy $E \pm \hbar\omega_{\text{LO}}$ in the subband j , where $\hbar\omega_{\text{LO}}$ is the energy of a LO phonon, the plus or minus sign accounting for absorption or emission of LO phonons, corresponding to superscript a or e , respectively. Transitions rates S_{ij}^a and S_{ji}^e are linked by the following equation [3]:

$$S_{ij}^a(E) = S_{ji}^e(E + \hbar\omega_{\text{LO}}) \quad (2.20)$$

The transition rate from an initial state $|i, k_i\rangle$ to all final states $|f, k_f\rangle$ due to longitudinal-optical-phonon emission at $T = 0$ K is equal to [5]:

$$\frac{1}{\tau_i} = \frac{m^* e^2 w_{\text{LO}}}{2\hbar^2 \varepsilon_p} \sum_f \int_0^{2\pi} d\theta \frac{I^{ij}(Q)}{Q} \quad (2.21a)$$

$$Q = (k_i^2 + k_f^2 - 2k_i k_f \cos \theta)^{1/2} \quad (2.21b)$$

where

$$k_f^2 = k_i^2 + \frac{2m^*}{\hbar^2} (\varepsilon_i - \varepsilon_f - \hbar w_{\text{LO}}), \quad (2.22)$$

$$\varepsilon_p^{-1} = \varepsilon_\infty^{-1} - \varepsilon_s^{-1} \quad (2.23)$$

where ε_∞ and ε_s are the high-frequency and static relative permittivities of the hetero-layer. $I^{ij}(Q)$ is defined as:

$$I^{ij}(Q) = \int dz \int dz' \chi_i(z) \chi_j(z) e^{-Q|z-z'|} \chi_i(z') \chi_j(z') \quad (2.24)$$

which is equal to δ_{ij} if $Q = 0$ and which decays like Q^{-1} at large Q values. Since the optical-phonon dispersion is neglected in our calculations, the transition rate for phonon emission at nonzero temperature is obtained from (2.21a, 2.21b) by multiplying the zero-temperature result by $(1 + n)$, where n is the thermal population of optical phonons:

$$n = \left[\exp \left[\frac{\hbar w_{\text{LO}}}{kT} \right] - 1 \right]^{-1} \quad (2.25)$$

The global transition rate G_{ij} between the subband i and subband j is the sum of the two transition rates for absorption of LO phonons (G_{ij}^a), and emission of LO

phonons (G_{ij}^e). In order to calculate the global transition rates G_{ij}^a and G_{ij}^e , all the initial states of energy E are filled at thermal equilibrium by the Fermi–Dirac occupation factor f . The electronic promotion from a subband i to a higher subband j (i.e., $j > i$) is calculated in the following manner. The integration on all these states is now performed on the subband i :

$$G_{ij}^a = \int_{E_j - \hbar\omega_{LO}}^{+\infty} S_{ij}^a(E) f(E) [1 - f(E + \hbar\omega_{LO})] n_{\text{opt}} D(E) dE \quad (2.26)$$

$$G_{ij}^e = \int_{\varepsilon_j + \hbar\omega_{LO}}^{+\infty} S_{ij}^e(E) f(E) [1 - f(E + \hbar\omega_{LO})] (1 + n_{\text{opt}}) D(E) dE \quad (2.27)$$

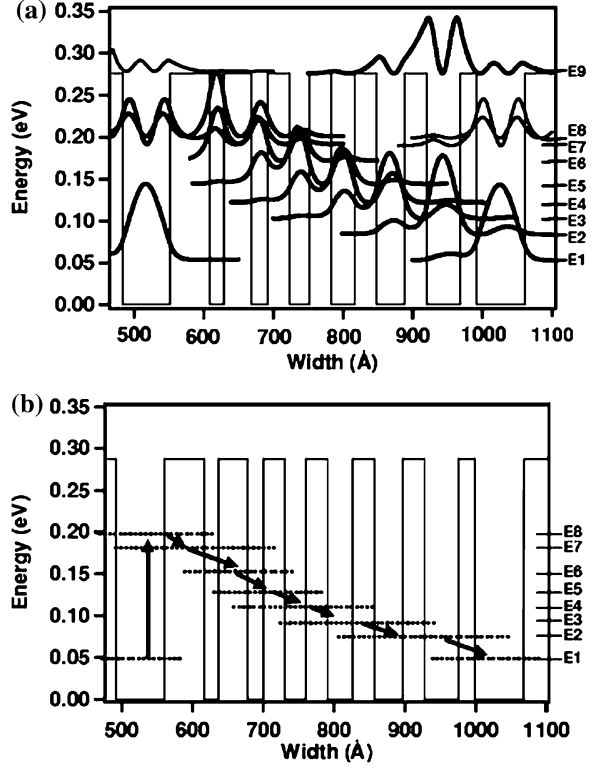
$f(E)$ and $f(E + \hbar\omega_{LO})$ are the Fermi–Dirac occupation factors at E and $(E + \hbar\omega_{LO})$, $D(E)$ is the two-dimensional density of state of the subband i and ε_j is the minimum of energy of the subband j . Of course, similar expressions can be written in the case of electronic transfers from a subband i to a lower subband j and n_{opt} is the Bose–Einstein statistic function which accounts for the phonon population.

In order to continue the modeling discussion, we consider the QCD structure introduced by Koeniguer et al. [3] which is presented in Fig. 2.1.

Two consecutive cascades a and b are represented in Fig. 2.2. Figure 2.1 present the most significant transitions where the intracascade and intercascade transitions are separately illustrated in parts (a) and (b), respectively where the solid-line arrows show the main transfer rates between one cascade and the following one and the dashed-line arrows represent other minor transitions. The typical value of transitions rates between two neighboring levels are between a few 10^{20} and $10^{25} \text{ m}^{-2} \text{ s}^{-1}$, corresponding to transition times between a few ps and a few tens of ps for a temperature of 80 K. These transitions are now limited to a few $10^{18} \text{ m}^{-2} \text{ s}^{-1}$ at the same temperature (and a corresponding transition time greater than 1 μs due also to the low amount of electron promotion to higher subbands for satisfying the Fermi–Dirac distribution). This shows that the electronic mobility is higher inside a cascade than between two consecutive cascades by several orders of magnitude. Finally, the resistance of a QCD is completely determined at 80 K by a few intercascade cross transitions, namely $E_1^A \rightarrow E_5^B$ and $E_1^A \rightarrow E_6^B$. The optimization of a QCD requires decreasing these transitions rates, thus increasing the resistance and decreasing the noise. This is possible by a separation of the wave functions, but at the expense of a lower optical matrix element, and a lower response. All the challenge of the QCD design consists of mastering this trade off.

The global current density can be evaluated by counting the electronic transitions between the two consecutive cascades. As a consequence, transition rates from cascade A to cascade B (two successive period) are not equal to the

Fig. 2.1 Presentation of a period of a typical QCD structure. **a** Conduction band diagram and wave function associated with each energy level of a period and **b** Principle of a detection [3]



reciprocal transitions rates from cascade *B* to cascade *A*. This global current density is given by:

$$J = q \sum_{i \in A} \sum_{j \in B} [G_{ij}(V) - G_{ji}(V)] \quad (2.28)$$

Let us consider two subband *i* and *j* associated, respectively, with cascades *A* and *B*. The introduction of two quasi-Fermi levels implies the differentiation of the two Fermi occupation factors in Eqs. 2.25 and 2.26. G_{ii}^a and G_{ji}^e can be evaluated by:

$$G_{ij}^a(V) = \int_{\varepsilon_j - \hbar\omega_{LO}}^{+\infty} S_{ij}^a(E) f_A(E) [1 - f_B(E + \hbar\omega_{LO})] n_{opt} D(E) dE \quad (2.29)$$

$$G_{ij}^e(V) = \int_{\varepsilon_j}^{+\infty} S_{ij}^e(E) f_B(E) [1 - f_A(E + \hbar\omega_{LO})] (1 + n_{opt}) D(E) dE \quad (2.30)$$

where f_A and f_B are the Fermi-Dirac occupation factors associated with quasi-Fermi level E_F^A and E_F^B . Considering Eq. ($S_{ij}^a(E) = S_{ji}^e(E + \hbar\omega_{LO})$) the difference is then equal to:

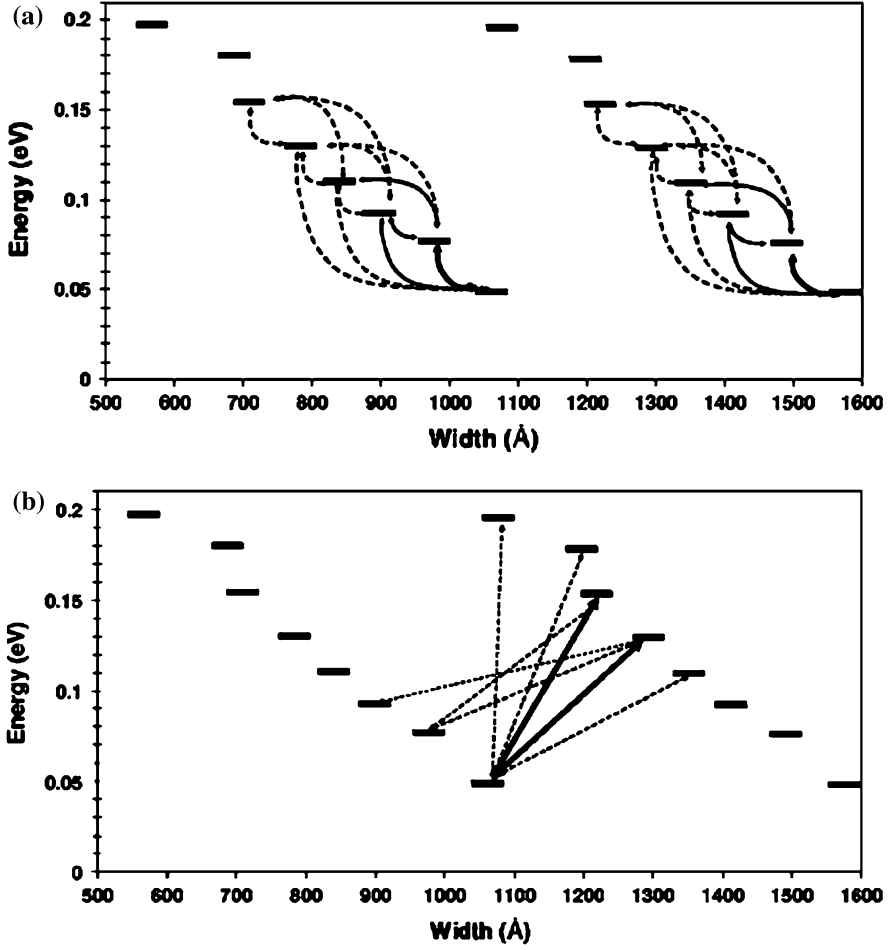


Fig. 2.2 Major transition rates of two consecutive cascades of the real device at 80 K. **a** The main transition rates inside each cascade (only the transition rates greater than $10^{20} \text{ m}^{-2} \text{ s}^{-1}$ are represented) and **b** the main transitions between the cascades: *solid lines* concern the major transition (greater than $4 \times 10^{18} \text{ m}^{-2} \text{ s}^{-1}$), whereas *dashed lines* represents the other main transitions (greater than $1 \times 10^{18} \text{ m}^{-2} \text{ s}^{-1}$ and lower than the major transitions) [3]

$$G_{ij}^a(V) - G_{ij}^e(V) = \int_{\varepsilon_j - \hbar\omega_{\text{LO}}}^{+\infty} S_{ij}^a(E) a(E) [1 - \gamma(E)] dE \quad (2.31)$$

where

$$\begin{aligned} a(E) &= n_{\text{opt}} f(E) [1 - f_B(E + \hbar\omega_{\text{LO}})] D(E), \\ \gamma(E) &= \frac{f_B(E + \hbar\omega_{\text{LO}}) [1 - f_A(E)] (1 + n_{\text{opt}})}{f_A(E) [1 - f_B(E + \hbar\omega_{\text{LO}})] n_{\text{opt}}} \end{aligned} \quad (2.32)$$

Without any applied voltage, the term $a(E)$ is equal to $a^{eq}(E)$ given by:

$$a^{eq}(E) = n_{\text{op}} f(E) [1 - f(E + \hbar\omega_{\text{LO}})] D(E) \quad (2.33)$$

Expressing the Fermi–Dirac functions, $\gamma(E)$ is simplified into:

$$\gamma(E) = \exp\left(\frac{E_F^B - E_F^A}{k_B T}\right) = \exp\left(\frac{-qV}{k_B T}\right) \quad (2.34)$$

where T is the temperature of the sample and k_B the Boltzman constant.

We recall that in the context of infrared photovoltaic detection, applied biases are very small. The Johnson noise is related to the resistance at 0 V: R_0 . In this calculation, it is then justified to linearize:

$$1 - \gamma(E) \approx \frac{q}{k_B T} V \quad (2.35)$$

This leads directly to the linear $I(V)$ behavior of the structure at low bias, through the multiplication by the constant a^{eq} (calculated with no applied voltage). For little variations of the voltage, the difference can be approximated by the following equation:

$$\begin{aligned} G_{ij}^a(V) - G_{ji}^e(V) &\approx \int_{e_j - \hbar\omega_{\text{LO}}}^{+\infty} S_{ij}^a(E) \alpha^{eq} \frac{qV}{k_B T} dE \\ &\approx G_{ij}^a(V = 0V) \frac{qV}{k_B T} \end{aligned} \quad (2.36)$$

Finally, global current density is so evaluated by the formula:

$$J = q \sum_{i \in A} \sum_{j \in B} G_{ij} \frac{qV}{k_B T} \quad (2.37)$$

where the term G_{ij} is defined by the sum of G_{ij}^a and G_{ji}^e calculated without any applied voltage. $R_0 A$ can be finally deduced from the last equation:

$$R_0 A = \frac{k_B T}{q^2 \sum_{i \in A} \sum_{j \in B} G_{ij}} \quad (2.38)$$

The linear absorption coefficient, $\alpha(\omega)$ for the intersubband transitions can be clearly calculated as follows [6]:

$$\begin{aligned} \alpha(\omega) &= \frac{\omega \mu c e^2}{n_r} |M_{fi}|^2 \frac{m^* k_B T}{L_{\text{eff}} \pi \hbar^2} \text{Ln} \left\{ \frac{1 + \exp[(E_F - E_i)/k_B T]}{1 + \exp[(E_F - E_f)/k_B T]} \right\} \\ &\times \frac{\hbar/\tau_{\text{in}}}{(E_f - E_i - \hbar\omega)^2 + (\hbar/\tau_{\text{in}})^2} \end{aligned} \quad (2.39)$$

where $E_{\text{fi}} = (= \Delta E) = E_f - E_i$, E_i and E_f denote the energy levels for initial and final states, respectively. Also, M_{fi} , μ , L_{eff} , n_r and τ_{in} are the dipole matrix element between initial and final states, the permeability, the spatial extent of electrons in subbands, the refractive index and the intersubband relaxation time, respectively.

For all types of quantum detectors [7] the responsivity is given by:

$$R = \eta \frac{\lambda e}{hc} \quad (2.40)$$

where η is the collection efficiency involving the photon absorption probability and the photoexcited electron transfer probability and λ the wavelength. One can assume the parameter η to be the external quantum efficiency of the device which corresponds to the ratio between the number N_c (electrons stored in the capacitor of the readout circuit) and the number N_{ph} (incident photons during the same time): $\eta = N_c/N_{\text{ph}}$. Introducing the number N_e of excited electrons in the whole QCD structure (that is in the N periods), the external quantum efficiency can be written as the product of two ratios: $\beta = N_c/N_e$ and $\alpha = N_e/N_{\text{ph}}$.

$$\eta = \frac{N_c N_e}{N_e N_{\text{ph}}} \quad (2.41)$$

β gives the proportion of the excited electrons which are finally stored in the external capacitor with respect to the quantity of infrared-excited electrons: β is the so-called photoconductive gain composed of $N = 40$ periods, 40 excited electrons are needed to generate one electron only in the readout circuit. This defines a maximum photoconductive gain of $1/40 = 2.5\%$. α is the ratio between the number of excited electrons in the entire device, which corresponds to the total number of absorbed photons in the entire structure, and the total number of incident photons: α is the absorption coefficient, also called quantum efficiency in the community of mid-IR detectors.

From responsivity and resistivity values, we can deduce the Johnson noise limited detectivity given by:

$$D^* = R(\lambda) \sqrt{\frac{R_0 A}{4kT}} \quad (2.42)$$

where $R(\lambda)$ is the peak responsivity, R_0 is the device resistance at null bias, A is the mesa area and T the temperature of the sample.

2.2.4 Effects of Number of Periods and Doping Density on the Detector Parameters

Quantum efficiency in a multiple period QWIP structure is expressed as [2]:

$$\eta_{abs} = 1 - e^{-N\alpha_{2D}\frac{\sin^2 \Theta}{\cos \Theta}} \quad (2.43)$$

where N is the number of periods. If we assume, that η_{abs} is much smaller than 1, the e^{-x} can be approximated by $1 - x$. Therefore we have:

$$\eta_{abs} = N\alpha_{2D}\frac{\sin^2 \Theta}{\cos \Theta} \propto N \quad (2.44)$$

Thus responsivity will be:

$$\mathfrak{R} \propto \eta_{abs} \frac{1}{N} \propto N \times \frac{1}{N} = \text{constant} \quad (2.45)$$

As seen in above equation, the responsivity is independent of the number of periods, N . However the noise gain changes with N as:

$$g_{\text{noise}} \propto 1/N \quad (2.46)$$

Therefore the background photon limited detectivity D_{BLIP}^* varies as:

$$D_{\text{BLIP}}^* = f(\mathfrak{R}, g_{\text{noise}}) \propto \sqrt{N} \quad (2.47)$$

In a QCD, responsivity is again constant but the device resistance R_0 will increase with N and hereby the Johnson noise limited detectivity, D_J^* will change as:

$$D_J^* \propto \sqrt{N} \quad (2.48)$$

It should be mentioned that D_{BLIP}^* the same behavior. Stacking N periods of a detector structure together means putting N current (noise) sources in series leads reduces the total noise by the \sqrt{N} . Increasing the number of periods does not change the BLIP temperature T_{BLIP} , but increases the total detectivity D_{tot}^* by \sqrt{N} .

In a similar way it is shown for small absorption, the absorption and then responsivity rises linearly in doping density, n_s as:

$$\mathfrak{R} \propto n_s \quad (2.49)$$

The background photon limited detectivity D_{BLIP}^* changes as:

$$D_{\text{BLIP}}^* \propto \sqrt{n_s} \quad (2.50)$$

Although in QWIP, the dependence of dark current on doping density is explicit, but since the transport system in QCD contains the large number of electronic states so there is no a simple and clear expression for the device conductance $G = 1/R_0$. Howbeit the population of the different states is determined by doping, the overlap of the states wavefunctions mainly determines the detector overall performance. Koeniguer et al. [3] have reported a model for a QCD structure, to simulate the n_s dependence of R_0A and therefore D_J^* .

2.2.5 Quantum Dot Infrared Photodetectors

In what follows, the calculation of detector parameters of this photodetectors is described. The peak responsivity in quantum dot infrared photodetectors (QDIP) is given by:

$$R_p^o = \left(\frac{e}{h\nu}\right)\eta_x p_c g, \quad (2.51)$$

where $h\nu$ and g are photon energy and optical gain which is given by Beck [8] in terms of the fill factor F , capture probability p_c and number of QD layers N , respectively and given as:

$$g = \frac{1 - \frac{p_c}{2}}{FNp_c}, \quad (2.52)$$

Also, the absorption quantum efficiency η_x can be expressed in term of high-field domain length ℓ as follows:

$$\eta_x = (1 - e^{-2\alpha\ell}) \quad (2.53)$$

Finally escape probability is expressed in the following relation:

$$p_e = \left[1 + \frac{\tau_t(v)}{\tau_r}\right]^{-1}, \quad (2.54)$$

where τ_r and τ_t are recapture life time and tunneling time which is given by Levine [9] in terms of the dot size L_D , phase velocity of an electron near the first excited state v and transmission coefficient $T(v)$, respectively as:

$$\tau_t = \frac{2L_D}{vT(v)} \quad (2.55)$$

The dark current in a QDIP, as a function of applied bias V is given by [10]:

$$I_{\text{dark}}(V) = ev_d(V)n_{\text{total}}(V)A \quad (2.56)$$

where $v_d(V)$ is the average electron drift velocity in the barrier material, n_{total} is the concentration of electrons excited out of the quantum dots by the thermionic emission and tunneling, and A is the detector area. Here:

$$v_d(V) = \frac{\mu F(V)}{\sqrt{1 + \frac{\mu F(V)}{v_s}}}, \quad (2.57)$$

$$n_{\text{total}}(V) = n_{3D}(V) + n_{\text{dot}}(V), \quad (2.58)$$

where the three-dimensional electron density $n_{3D}(V)$ can be estimated by Liu [11] in terms of the barrier effective mass m_b and thermal activation energy

$E_a (= hc/\lambda_{\text{cut-off}})$, which equals the energy difference between the top of the barrier and the Fermi level in the dot as:

$$n_{3D} \simeq 2 \left(\frac{m_b k_B T}{2\pi\hbar^2} \right) e^{\frac{E_d}{k_B T}} \quad (2.59)$$

Also, the zero-dimensional electron density which can tunnels through the barrier $n_{\text{dot}}(V)$ was calculated in [12] and illustrated in Eq. 2.60.

$$n_{\text{dot}}(V) = \int_0^{V_{02}} N_{\text{dot}}(E) f(E) T(E, V) dE \quad (2.60)$$

In the calculation of Eq. 2.59, we assumed that the transmission coefficient $T(V)$ is unit for $E > V_{02}$. In Eq. 2.60, N_{dot} is density of states of the quantum dots. The total noise for a photodetector can be expressed as sum of generation-recombination (shot) and the Johnson (thermal) noise terms. The Johnson noise is not included in the calculation, since it is generally much less than the shot noise [13–15]. The photoconductor current shot-noise can now be obtained using the optical gain g (valid for small quantum dot capture probability, i.e., $p_c \cong 1$):

$$i_n = \sqrt{4eI_{\text{dark}}g\Delta f}, \quad (2.61)$$

where Δf is the bandwidth. Now the specific detectivity D^* of QDIP at different temperature and applied biases is obtained from the peak responsivity and current shot-noise [12] as follows:

$$D^* = R_p^o \sqrt{A_{\text{eff}} \Delta f} / i_n, \quad (2.62)$$

where A_{eff} is the absorption effective cross-section area. Finally one can calculate the noise-equivalent temperature difference NE ΔT as [14]:

$$\text{NE}\Delta T = i_n k T_B^2 \lambda / \left[hc A_{\text{eff}} \sin^2(\Omega/2) \int_{\lambda_1}^{\lambda_2} R(\lambda) W(\lambda) d\lambda \right] \quad (2.63)$$

where Ω is optical field of view, T_B is the black body temperature, λ_1 and λ_2 are the integration limits that extend over the responsivity spectrum and $W(\lambda)$ is the blackbody spectral density which is obtained as:

$$W(\lambda) = (2\pi c^2 h / \lambda^5) (\exp(hc/\lambda k T_B) - 1) \quad (2.64)$$

2.3 Terahertz and Infrared Quantum Cascade Detectors

Quantum cascade structures are relatively new structure in the field of QWIP which are introduced to reduce the dark current owed to the bias-free operation (photovoltaic operation mode). Thus the capacitor loading problem in the focal

plane arrays due to the dark current and the dark current noise problem are minimized.

Quantum well infrared photodetectors (QWIPs) have been developed in the recent years from the fundamental-physics point of view towards fabrication of large area focal plane arrays [1, 16, 17]. In principle, the QWIPs operate in two electronic transport modes: photoconductive and photovoltaic. The first operation mode requires external bias voltage to conduce the electrical current where the excited electrons tunnel out of the quantum wells in the presence of the electric field and are gathered as a measure of incident light. The limiting factor in this mode of operation is the presence of dark current which bound the device performance to low temperatures. The typical applied electric fields are about several 10 kV/cm which are the direct result of a trade-off between high quantum efficiency (the capture probability of photo-excited carriers) and low noise. The problem of dark current is a motivation for developing low dark current and appropriate quantum efficiency (the second operation mode).

Beside the mentioned problems, the carrier transport mechanism in photoconductive mode involves both 2D and 3D electron states in well and continuum, respectively, between which the modeling of carrier transition has its own theoretical complications [18, 19]. The diffusion of electrons from 3D to 2D states (and vice versa) is a particularly difficult theoretical problem. That is why most models use adjustable parameters such as the capture time [20] or the capture probability, affecting the photoconductive gain [21].

The second types of photodetectors, i.e., photovoltaic photodetectors, do not require external bias voltage and thus suffer very little or even no dark current. Therefore, there is no generation-recombination noise in the dark condition (and therefore the capacitors in the focal plane arrays are not filled by dark current).

A conceptual schematic of a photovoltaic photodetector structure fabricated by Kastalasky et al. [22] is presented in Fig. 2.3a. The operation principle of this device is based on electron capture from a miniband which terminates with a blocking barrier. Since the electron current is blocked by the blocking barrier in the lower miniband, only electrons of higher energies (in the upper miniband) have enough energy to pass through the barrier and thus the photo-induced current is created without need to bias voltage. Goossen et al. [23] have introduced a different structure (Fig. 2.3b) in which the device capacitance depends to the carriers flowing through the depletion layer. A quantum well-based structure with asymmetrically doped double barriers composed of GaAs/AlAs/AlGaAs material compositions is schematically plotted in Fig. 2.3c [24]. The photo-excited electrons from the lower to the upper miniband tunnel out of the quantum well with a finite probability through the AlAs barrier. There are two probabilities whether the excited electrons transport to left or right side. The spatial field in the AlGaAs layers causes an electric current to the right side and most of carriers are relaxed in their path to the quantum well place in the right-hand side of $\text{Al}_{0.3}\text{Ga}_{0.7}\text{As}$ layer. The general concept of this transport mechanism is illustrated in Fig. 2.3d. Figure 2.3e also presents a similar structure to the structure in Fig. 2.3c but with a reduced barrier height. The photovoltaic operation of this structure is driven by a

Fig. 2.3 Transport mechanism of photovoltaic infrared detectors involving intersubband transitions: **a** superlattice with blocking barrier, **b** single quantum well with surface depletion layer, **c** asymmetrically doped double-barrier quantum well, **d** general subband configuration for photovoltaic detection, and **e** modulation-doped single-barrier quantum well [27]

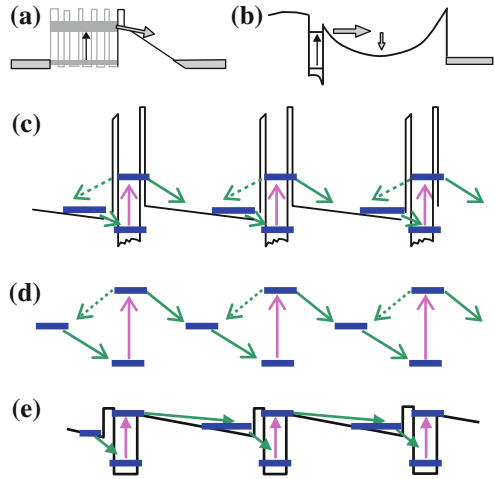
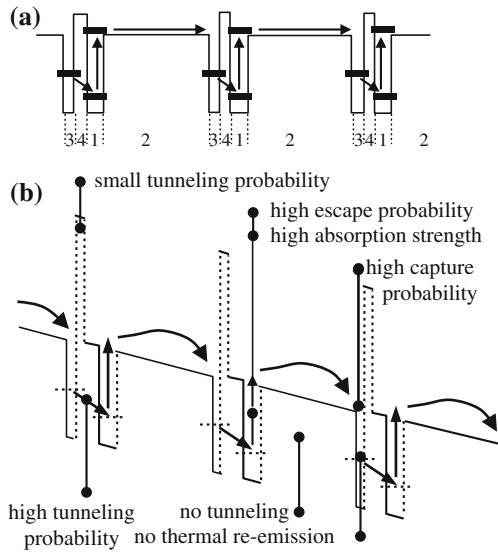


Fig. 2.4 **a** Schematics of the four-zone approach for photovoltaic Intersubband photo-detection; potential distribution (*I* emission zone, 2 drift zone, 3 capture zone, and 4 tunneling zone) and basic operation (arrows). **b** Bandedge distribution of a four-zone QWIP in an electric field and considerations for optimization [27]



tunneling barrier and a modulation doped induced internal electric field [25, 26]. The detectivity parameter of this structure is three times lower than the reported values for photovoltaic infrared photodetector operating at the same wavelength (10.5 μm). Low detectivity of this structure may be relates to the non-optimized internal electric field.

A new four-zone structure for QWIP has been proposed by Schneider et al. (Fig. 2.4) where each period of the active region consists of four independent zones: (1) excitation zone, (2) drift zone, (3) capture zone and (4) tunneling zone [28, 29]. The photo-excited carries in the excitation zone are transported in the

quasi-continuum band edge of the drift region. Then the carriers are relaxed to the capture zone and fill the quantum well by tunneling. This contributes to a photocurrent without any external bias voltage.

Quantum cascade structure are of the well-known structures for effective transport mechanism. A photovoltaic intersubband quantum cascade photodetector (QCD) has been introduced in Ref. [30] which operates without any bias voltage and hence suffers no dark current. The optical and electrical transport specifications of these structures confirm the suitability for small pixel-large array applications. The main design purpose of the QCD is creation of a bias-free photo-induced electron displacement through the cascaded quantum states. Thus, a comprehensive study is required to get familiar with the carrier transport process in these structures. Generally quantum cascade devices have been described with kinetic model band making use the Monte Carlo simulation [31].

2.3.1 Dual Color Mid-Infrared Quantum Cascade Photodetector in a Coupled Quantum Well Structure [32]

Beside the positive and negative points of the mentioned structures, simultaneous detections of two or more wavelength can be an interesting feature. Several applications are predicted for multi-wavelength detection such as reducing the number of false positives through detection of infrared radiations of an object [33]. Also, dual-wavelength imaging in terahertz and mid-IR region is another interesting feature of multi-wavelength detection [34].

In this section, we introduce a QCD structure which is capable of detecting two simultaneous wavelengths (9.94 and 5.88 μm).

Figure 2.5 shows the respective QCD structure. This structure is composed of 40 periods of coupled AlGaAs/GaAs QWs. The first QW is n-doped in order to populate its first level of energy E_1 in the conduction band with electrons. The second well is as the capturing well, attached to main active well. The absorption of a photon at energy $h\nu = E_6 - E_1$ and $h\nu = E_7 - E_1$ transfers an electron from ground state towards sixth and seventh excited states. The first transition will be transported after coupling in the second well of the transport path constructed by superlattice structure. The second transition will be captured to the second well by release of a LO phonon and will be transported through the same transport path constructed by superlattice structure.

Table 2.1 provides the global transition rates G_{1j} for novel QCD structure, the number of transitions per second and per square meter from the fundamental level 1 to the level j , with $j = \{2, \dots, 7\}$, in the neighboring cascade. For temperatures 80, 120, 250 K, the results have been obtained.

Figure 2.6 presents a typical example chosen to illustrate the quality of the modeling: the experimental R_0A of the device as a function of $1000/T$, where T is the temperature of the sample.

Fig. 2.5 The schematic of dual-wavelength QCD structure (size of considered layers from left to right in Å are: 22,**65**,22,**40**,5,10,10,10,5,**36**, 22,**42**,22,**50**,22,**65**,22. The under lined layer, denotes doped well to $5 \times 10^{-5} \text{ cm}^{-2}$ and bold layers denote quantum wells) [32]

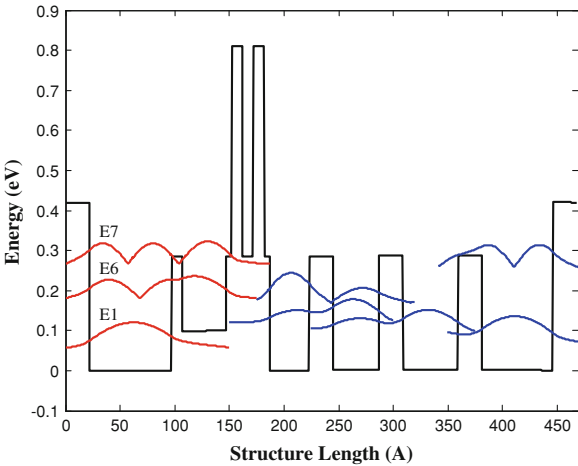


Table 2.1 Values of some transition rates in relation to the main electronic transition represented on Fig. 2.5

$G_{1,j}$ ($\text{m}^{-2} \text{ S}^{-1}$)	80 K	120 K	250 K
$1 \rightarrow 2$	$5.7932\text{e} + 015$	$3.8970\text{e} + 017$	$3.5614\text{e} + 019$
$1 \rightarrow 3$	$3.8508\text{e} + 017$	$2.5900\text{e} + 019$	$2.3630\text{e} + 021$
$1 \rightarrow 4$	$4.3563\text{e} + 018$	$2.9307\text{e} + 020$	$2.6815\text{e} + 022$
$1 \rightarrow 5$	$1.3963\text{e} + 021$	$9.3969\text{e} + 022$	$8.6427\text{e} + 024$
$1 \rightarrow 6$	$1.4009\text{e} + 024$	$9.4284\text{e} + 025$	$8.6775\text{e} + 027$
$1 \rightarrow 7$	$2.2470\text{e} + 024$	$1.5110\text{e} + 026$	$1.3733\text{e} + 028$

Fig. 2.6 R_0A (product of the resistance at 0 V by the area of the pixel) as a function of $1,000/T$ [32]

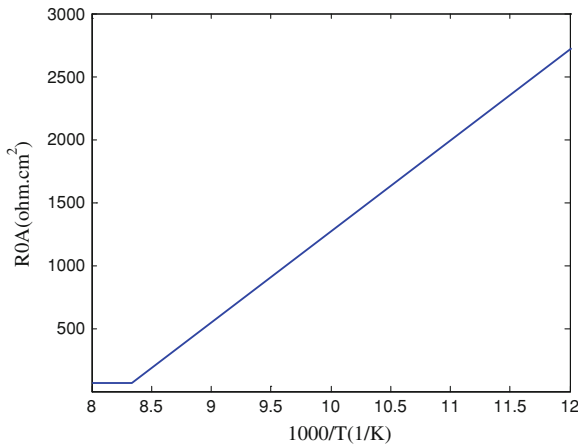


Fig. 2.7 Absorption spectrum at 120 K temperature [32]

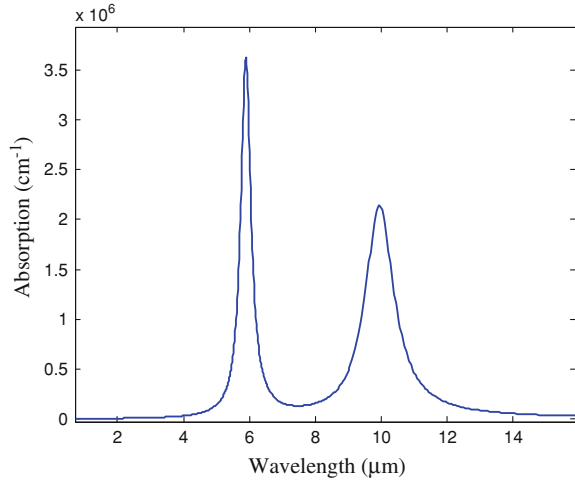


Figure 2.7 shows the absorption spectra performed at 120 K temperature. The two peaks can be easily linked to an intersubband transition between two energy levels and the different transitions are identified on this figure: the peak at 9.94 μm and other at 5.88 μm corresponds to the transition from level E1 (ground state) to levels E6 and E7 (sixth and seventh excited states), respectively.

Figure 2.8 illustrates the responsivity spectra calculated at 120 K for two wavelengths. We found two responsivities: $R_{\text{peak},1} = 67.5$ mA/W, $R_{\text{peak},2} = 118.5$ mA/W, at $\lambda = 6.82$ μm and at $\lambda = 12.35$ μm, respectively.

The detectivity spectrum at 120 K for two wavelengths is shown in Fig. 2.9. Taking $R_0A = 70 \Omega \text{cm}^2$ we obtained at 120 K: $D^*(\lambda = 12.35) = 1.2 \times 10^8$ J, $D^*(\lambda = 6.85) = 6.89 \times 10^7$ J.

Fig. 2.8 Responsivity spectrum at 120 K for two wavelengths [32]

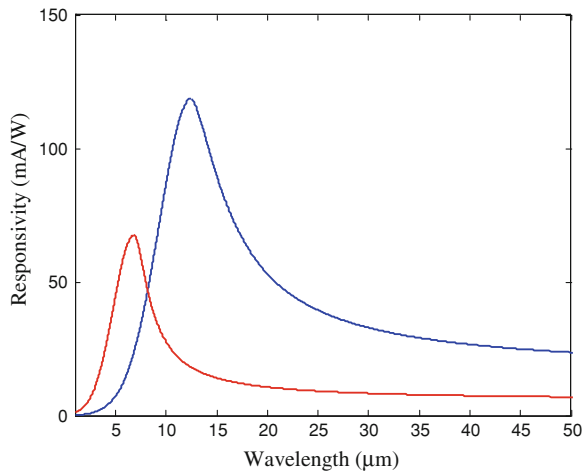


Fig. 2.9 Detectivity spectrum at 120 K for two wavelengths [32]

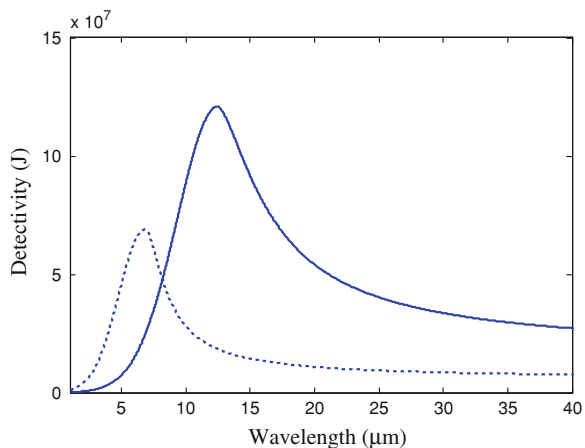
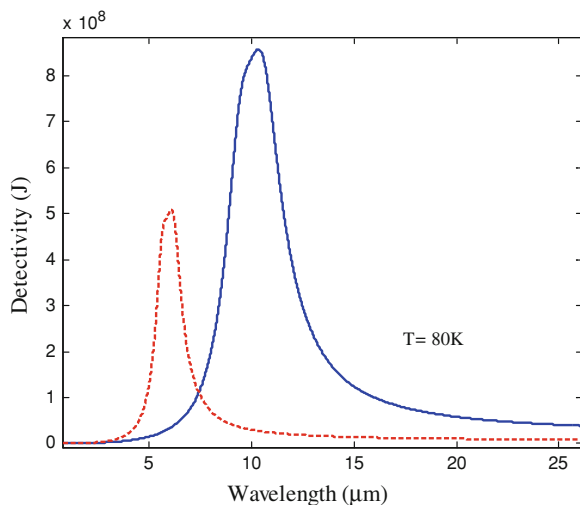


Fig. 2.10 Detectivity spectrum at 80 K for two wavelengths [32]

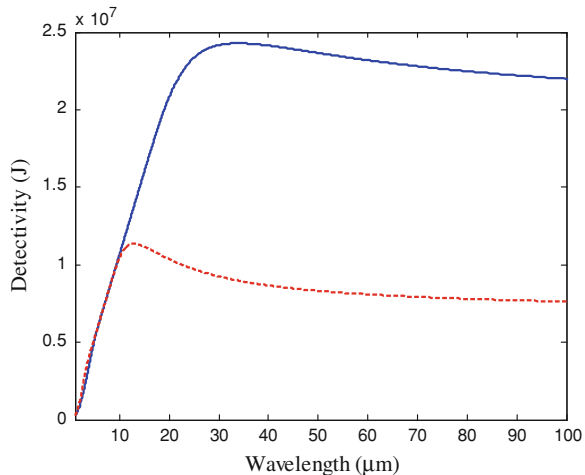


For two different temperatures (80, 250 K) the detectivity spectrum for two wavelengths are represented in Figs. 2.10 and 2.11, respectively.

2.3.2 A Dual-Color IR Quantum Cascade Photodetector with Two Output Electrical Signal

Recently, there has been a great deal of interests in the fabrication of multicolor detectors to enhance the performance of detection, in particular, for discrimination

Fig. 2.11 Detectivity spectrum at 250 K for two wavelengths

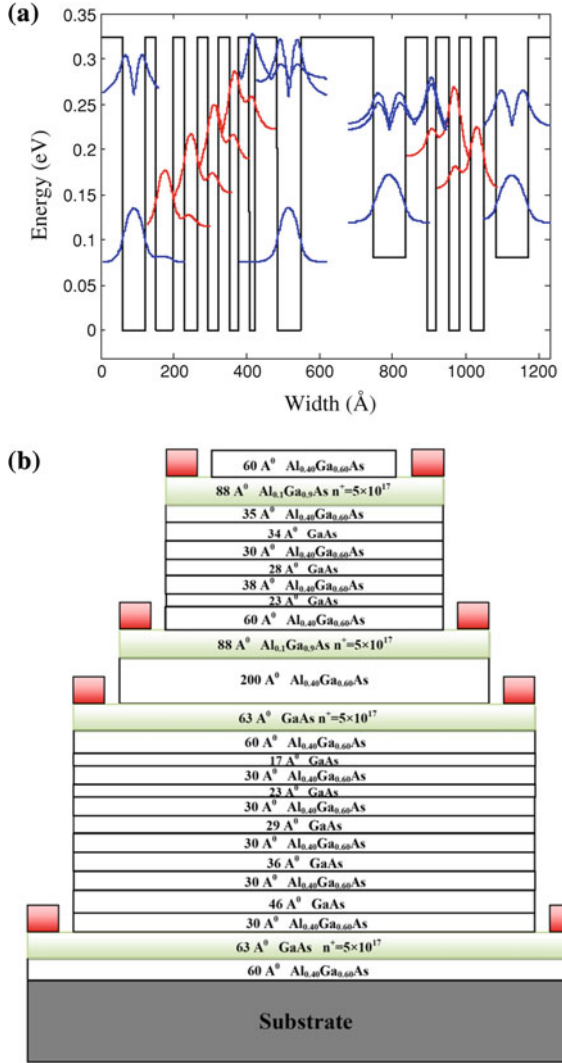


of objects and imaging under varying atmospheric conditions [35]. As mentioned before the different wavelength regions are associated with different practical applications, detecting an object's infrared emission at multiple wavelengths can be used to reduce the number of false positives. The possibility to have dual wavelength operation is also very attractive in the THz and mid-IR regions for applications like dual wavelength imaging [34]. In order to get response in several wavelength ranges in QWIPs, there are several procedures. One approach is to build several stacks of square quantum wells with different peak response wavelengths [36–43]. The response due to different wavelengths can be achieved either by contacting each stack separately in a constant bias or by controlling the bias across the stacks to sequentially activate different stack. The other approach is to use asymmetric or coupled quantum well structures where the transitions from the ground state to several excited states are allowed [44–46]. The advantage of the latter approach is that it requires only one set of quantum wells which makes the fabrication relatively simpler. In this case, the photoexcited carriers are extracted by controlling the bias across the device. In spite of all achieved developments in multi-color detection, there are several important deficiencies such as bias-dependant wavelength detection, difficulties in simultaneous detection of wavelengths and identical output current path associated with all detected wavelengths.

In this section, we introduce a detector structure based on quantum cascades which is able to detect two different wavelengths simultaneously through two independent output current paths. The two under consideration structures consists of own left and right paths that each path can detect specified wavelength with associated active region. In first structure, the N consecutive periods in each path was studied however, for second structure, we have considered only one period with single main active region for both left and right parts.

The first proposed structure for DC-QCD consists of two separated N -period GaAs/AlGaAs heterostructures containing specified active regions and subsequent

Fig. 2.12 **a** Conduction band profile and associated wave functions for first structure in one period and **b** 3D schematic of the QCD device structure



transport ladders in each period to detect wavelengths in completely independent output current paths. A 200 Å $\text{Al}_{0.40}\text{Ga}_{0.60}\text{As}$ layer is used as spacer layer between two sections. The energy levels and associated wave functions for considered structure as well as 3D view of the QCD structure are illustrated in Fig. 2.12 in one period of the device. All QWs and barriers are made of GaAs and $\text{Al}_{0.40}\text{Ga}_{0.60}\text{As}$, respectively (except for active region of right path which is composed of $\text{Al}_{0.1}\text{Ga}_{0.9}\text{As}$). The layer widths in one period from left to right (active region and ladder) in the left path starting with active well layer are: 63/60/17/30/23/30/29/30/36/30/46/30 and 63 Å, respectively.

The right path (in the right-hand side of thick $\text{Al}_{0.40}\text{Ga}_{0.60}\text{As}$ layer) consists of N successive periods with layer widths of 88/60/23/38/28/30/34/35/88 Å, respectively in one period starting with the active well. The peak detection energies of the DC-QCD, which corresponds to the intersubband transition energies between ground and first excited state in each active region was calculated to be 185 meV (6.74 μm) for left path and 107 meV (11.70 μm) for right path.

The second proposed structure for DC-QCD consists of only one active region (stepped quantum well) and with two transport ladders that extract the photo-excited carriers through two side of active well. Figure 2.13 represents the conduction band profile, energy levels and the wave functions associated with each energy level for considered structure.

Barriers, QWs and two steps are made in $\text{Al}_{0.40}\text{Ga}_{0.60}\text{As}$, GaAs and $\text{Al}_{0.22}\text{Ga}_{0.78}\text{As}$, respectively. The layer sequence in Å starting from the first quantum well from left to right is as follows: 63/36/46/32/36/32/29/36/21/33/18/60/42/52/30/60/25/30/30/30/38/30/48/30/64. The intersubband transition energies between ground-first excited state and ground-second excited state in active region were calculated to be 140 meV (8.88 μm) and 223.7 meV (5.56 μm), respectively. The advantage and disadvantage of such structure with only one period are discussed at the end of section. Figures 2.14 and 2.15 presents the resistivity at 0 V (R_0A) as a function of $1000/T$ for right and left path of two proposed structure, respectively.

The short width for right paths in two structures leads to high intercascade transition rates, so the values of R_0A are low for these two paths in comparison with left parts with high values of R_0A . Figure 2.16 presents the linear absorption coefficient, $\alpha(w)$ for the intersubband transitions of considered structures.

Figure 2.17 depicts the peak responsivity for two different structures of proposed DC-QCD.

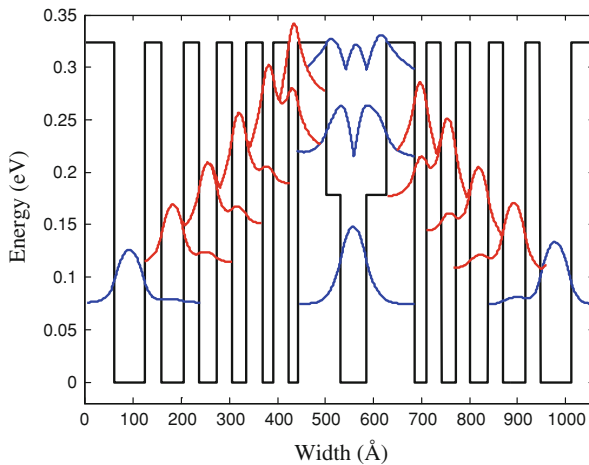
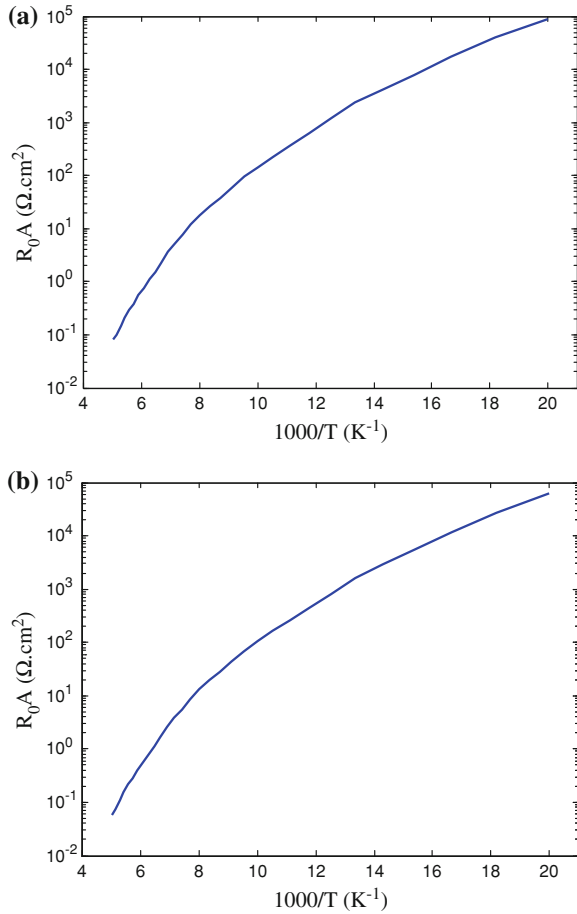


Fig. 2.13 Conduction band profile and wavefunctions for second structure

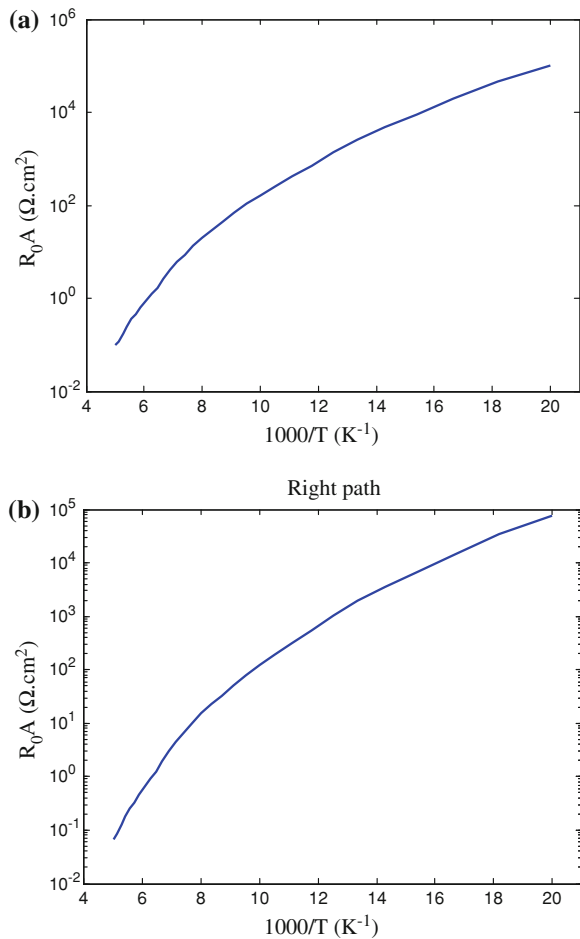
Fig. 2.14 R_0A for **a** Left path and **b** right path of the first structure (T is the sample temperature)



Finally, from responsivity and resistivity, it can deduce the Johnson noise limited detectivity. Figure 2.18 presents detectivity spectrum for one period of two considered structures in $T = 80$ K.

The extracted R_0A figures for right and left paths of first and second structures are considered for only one period but the whole resistance of the device is directly proportional to N ($R_{0A_{\text{Total}}} = N \times R_{0A_{\text{one-period}}}$) and decrease exponentially with doping concentration. So, for second structure, the obtained R_0A is N times smaller than the device resistance for the first structure, resulting in lower induced potential. On the other hand, the detectivity parameter is relative to N ; it means that the detectivity for the first structure is \sqrt{N} times larger than for the second structure. Since the main limitation of quantum cascade detectors is a low response with respect to photoconductive detectors, the main challenge is to design a structure with higher response keeping the same dark current level. This goal is not achievable by increasing the doping concentration since the resistance of the

Fig. 2.15 R_0A for **a** left path and **b** right path of second structure



device decreases dramatically with doping concentration. Another approach is the reduction of the number of periods. In this way, an improvement is expected and high responsivity values are achievable for such structures with small number of periods. So, in quantum cascade based detectors, there is a tradeoff between detector parameters meaning that good structure design leads to proper performance of the devices.

2.4 Terahertz Quantum Well Photodetector Based on Two-Photon Absorption [47, 48]

Nonlinear coefficient for second-order susceptibility resulting from intersubband transitions in QWs increases with three orders of magnitude in comparison with host material GaAs [49]. In particular, for two-photon intersubband transitions,

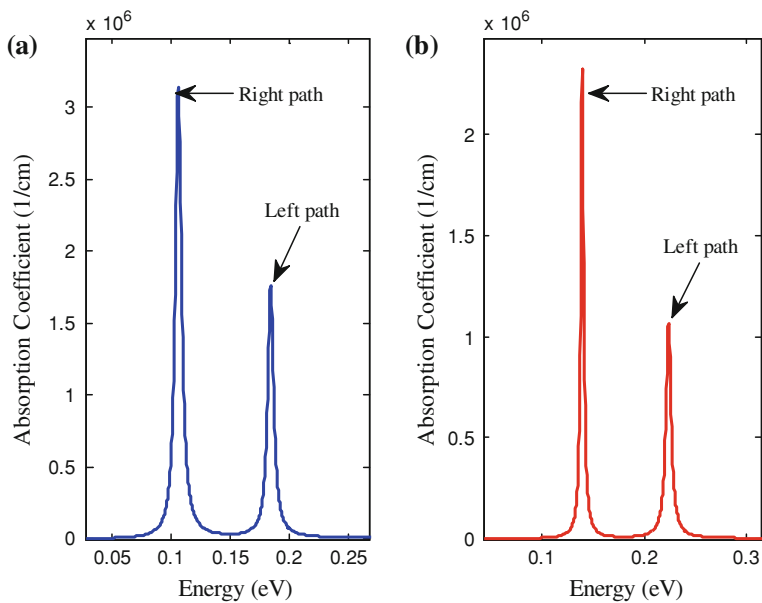


Fig. 2.16 Absorption coefficient as a function of energy **a** for first structure and **b** for second structure ($T = 120$ K)

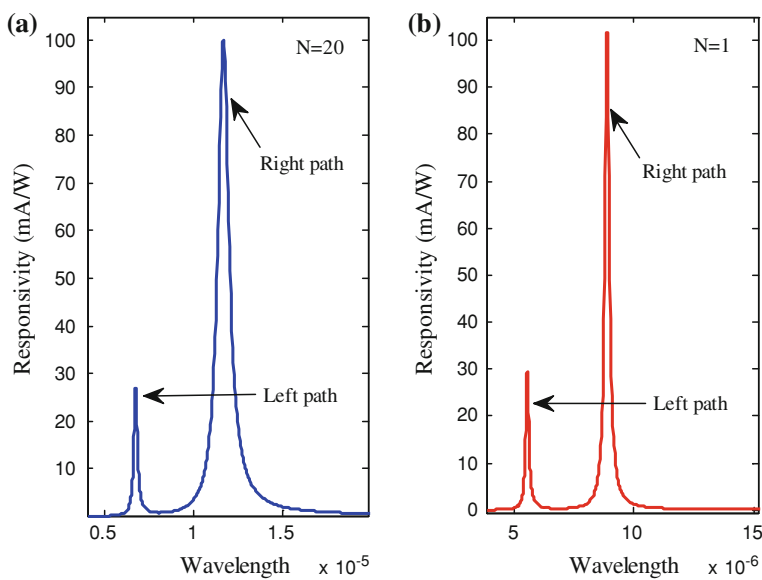


Fig. 2.17 Responsivity spectrum as a function of wavelength **a** for first structure and **b** for second structure ($T = 120$ K)

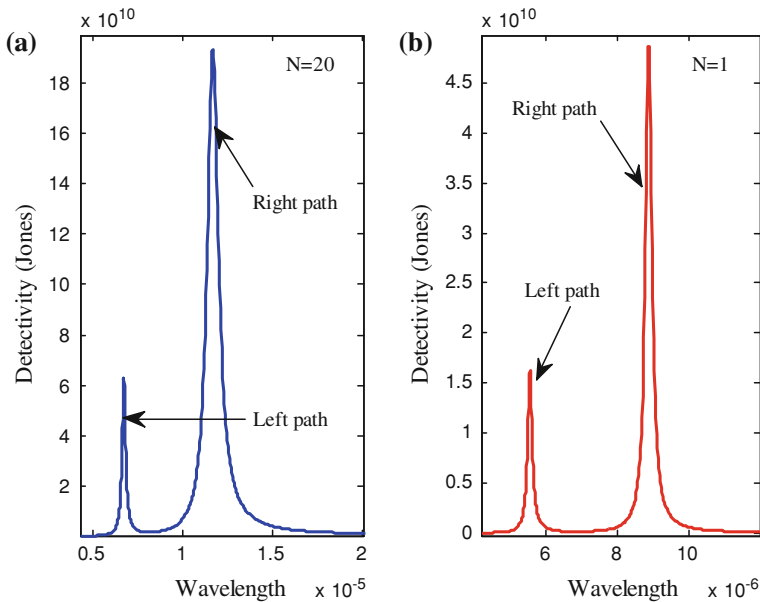


Fig. 2.18 Detectivity spectrum as a function of wavelength **a** for first structure and **b** for second structure ($T = 80$ K)

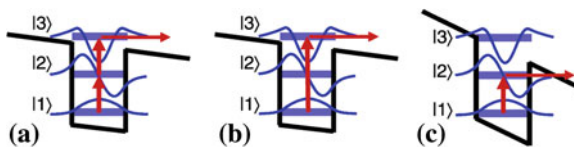


Fig. 2.19 Band diagrams for **a** quadratic detection associated with transitions $|1\rangle \rightarrow |2\rangle$ and $|2\rangle \rightarrow |3\rangle$, **b** linear detection by transition $|1\rangle \rightarrow |3\rangle$, and **c** linear detection involving $|1\rangle \rightarrow |2\rangle$ assisted by tunneling [47]

nonlinearities are six orders of magnitude stronger than the bulk GaAs [50, 51]. The QWIP which is exploited for this, designed for wavelengths at 8–12 μm with two bound subbands $|1\rangle$, $|2\rangle$, and one equidistant continuum resonance $|3\rangle$ where an electron is excited into the continuum by two infrared photons and hence produced photocurrent is a quadratic function of the incident power (Fig. 2.19a) [50]. This nonlinear behavior introduces a new quadratic detector device in contrast with the linear power dependence QWIPs [52]. Excellent sensitivity for quadratic detection has been achieved, with nonlinear optical signals appearing at power densities as low as 0.1 W/cm^2 [50]. Since the parasitic time constants arising from the device capacitances or resistances are not influencing the

nonlinear process, temporal resolution of two-photon QWIPs is only restricted by the sub-ps intersubband and phase relaxation times.

Lately too much attention has been paid for nonlinear THz detectors because of their applications in femtosecond lasers based THz technology and room temperature based nonlinear detection [53–55].

The structure of two-photon THz-QWIP is made of an active region (consisting 20 GaAs QWs of 18 nm width with central Si-doping of $1 \times 10^{17} \text{ cm}^{-3}$ and 70 nm width $\text{Al}_{0.05}\text{Ga}_{0.95}\text{As}$ barriers) sandwiched between two n-type GaAs contact layers with 400 and 700 nm thicknesses. As usual the coupling of the THz radiation into the active region was accomplished using 45° facets [52]. Computations for the chosen structural parameters reveal an operation wavelength slightly less than $50 \text{ } \mu\text{m}$ [47].

By using the linear photocurrent spectroscopy which is carried out by a FTIR spectrometer at low temperature and various bias voltages, spectral properties were analyzed (Fig. 2.20). Considering the linear excitation from the ground state into the continuum for the 0.1 V bias voltage the photocurrent begins in at photon energies around 380 cm^{-1} (Fig. 2.19b: the parity forbidden selection rule is not satisfied due to the applied electric field and the state $|3\rangle$ being in the continuum) and eventually this leads to an increase of photocurrent around the cutoff energy. At the 0.5 V bias voltage a significantly steeper increase in the cutoff energy (due to the odd parity of the applied electric field) along with moves towards the lower energies is observed. Because of two-photon excitation being negligible at the low intensities as well as the state $|2\rangle$ being completely confined in the QW at this field, no signal is generated at the energy of the $|1\rangle \rightarrow |2\rangle$ transition. However at 0.94 and 1.5 V bias voltages, the barrier leakage at the energy of $|2\rangle$ (due to Fowler–Nordheim tunneling into the continuum) allows that carriers can escape from the second state of QW with finite probability (Fig. 2.19c) thus induces a pronounced

Fig. 2.20 Linear photocurrent spectra of two-photon THz-QWIP at different bias voltages [48]

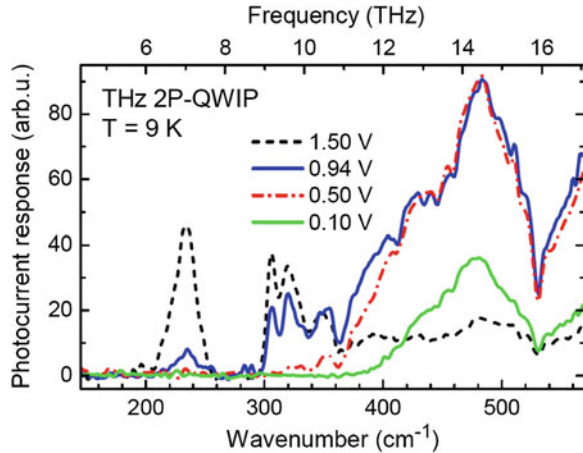
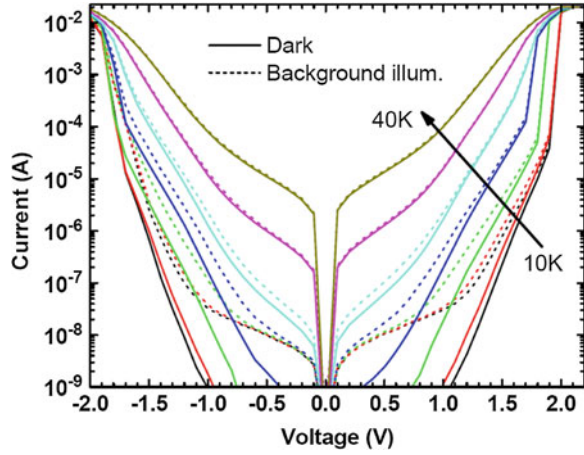


Fig. 2.21 Current–voltage curves of THz two-photon QWIP at temperatures from 10 to 40 K with and without background illumination [48]



peak at 235 cm^{-1} ($42.5 \text{ }\mu\text{m}$). The Reststrahlen band (due to strong optical-phonon induced absorption in the GaAs substrate) suppresses the response towards higher energies. A significant photoresponse between the Reststrahlen band and the $|1\rangle \rightarrow |3\rangle$ transition energy is occurred above 300 cm^{-1} . It is worth mentioning that there are a number of narrow dips in the spectral shape above the Reststrahlen band which are caused by two-photon absorption, typical for THz QWIPs, whereas a Fano lineshape is observed if the active region is involved in the two-photon transition [56].

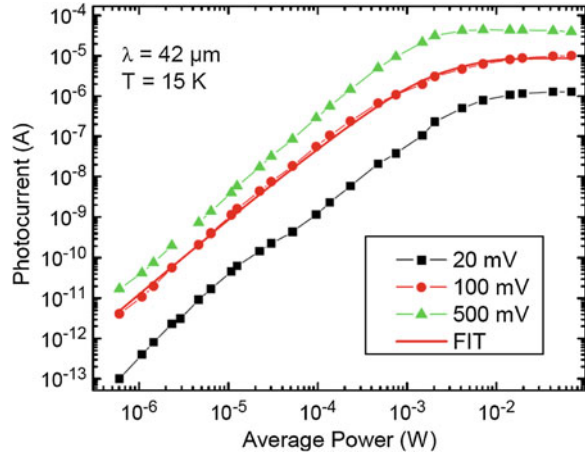
Based on the investigations of I – V curves at varying temperatures for two-photon THz-QWIP (Fig. 2.21), the detector is still BLIP (background limited performance) at 25 K if the bias is less than 1 V.

Quadratic detection is being investigated through the measuring of the photocurrent as a function of incident power where a free-electron laser (FEL) excites the transition at a wavelength of $42 \text{ }\mu\text{m}$. The two-photon THz-QWIP is biased at 500 mV and below in order to suppress the tunneling-induced linear photocurrent contribution. The final state of the two-photon transition is aligned with the continuum. Figure 2.22 shows the photocurrent I versus the incident power P of the FEL where the photocurrent increases quadratically with the incident power, followed by saturation behavior. The intensity dependence is described by the equation [57]:

$$I = SP^2 W\left(\frac{I_{\text{Sat}}}{SP^2}\right) \quad (2.65)$$

where S represents the quadratic contribution to the photocurrent, I_{Sat} the saturation current, and W Lambert's W -function. This is an approximation where the photoconductive gain depends linearly and the dark current exponentially on the local electric field inside the active region.

Fig. 2.22 Measured intensity dependence of the photocurrent at 20, 100, and 500 mV bias, including a fit for 100 mV [48]



2.5 Quantum Dots THZ-IR Photodetector

2.5.1 An Overview of Quantum Dot

The introduction of quantum wells in the early 1970s was a turning point in the direction of research on electronic structures [58]. A quantum well is a very thin layer of a semiconductor sandwiched between two layers of another semiconductor with wider energy gaps. The motion of electrons in a quantum-well structure is bound in two directions if the thickness of the quantum well layer is of the order of the de Broglie wavelength [15].

In the 1980s the interest of researchers shifted toward structures with further reduced dimensionality: one-dimensional confinement (quantum wires) [59] and zero-dimensional confinement (quantum dots). Localization of carriers in all three dimensions breaks down the classical band structure of a continuous dispersion of energy as a function of momentum. Unlike quantum wells and quantum wires, the energy level structure of quantum dots is discrete.

To demonstrate useful QD-based devices several requirements need to be fulfilled [60]:

1. Small QD size and sufficiently deep localizing potential for observation of zero-dimensional confinement.
2. High density of QDs and a high filling factor.
3. Low dislocation density material.

The QD size should not exceed a lower and an upper size limit dictated by the population of energy levels. The minimum QD size is the one that ensures existence of at least one energy level of an electron or a hole or both. For instance, for the InAs/AlGaAs system, the critical diameter of the QDs is $\sim 3\text{--}5$ nm, whereas this value is about 1 nm for the GaN/AlN system [15].

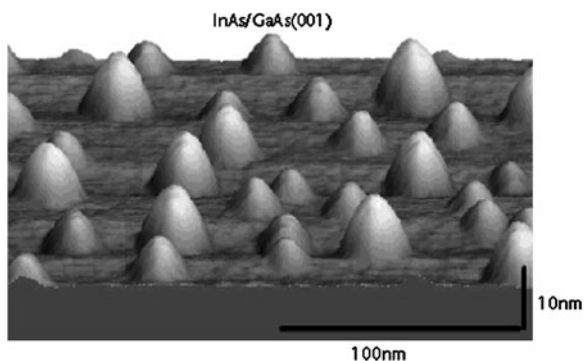
Several methods have been used for fabrication of QD structures. Depending on the thicknesses associated with the potential confinement, the energy of the intersublevel transitions can exhibit resonances varying from the mid-infrared to the far infrared spectral range [61]. Post-growth patterning of quantum dots and transferring of the pattern to the semiconductor layer by etching was one of the earliest implemented methods [62]. Another method is selective growth of a compound semiconductor with a narrower bandgap on the surface of another semiconductor with a wider bandgap.

These techniques have been successfully applied to study the transport properties of quantum dots [63]. First observations of intersublevel transitions in the far infrared have been reported in the early 1990s, either in InSb-based electrostatically defined quantum dots [64] or in structured two-dimensional electron gas [65]. In the latter cases, the intersublevel transitions were resonant in the far infrared because of the large lateral sizes of the quantum dots.

One of the most popular ways to realize quantum dots is to rely on a spontaneous formation process. This can be achieved in the so-called Stranski–Krastanow growth mode [66] that occurs during the epitaxial growth between lattice-mismatched semiconductors. The quantum dot formation is driven by the strain accumulated in the epitaxial layer. Above a given critical thickness of the wetting layer (WL), islands with scales ranging in the nanometer range are spontaneously formed. This growth mode can be successfully obtained by different growth techniques, including molecular beam epitaxy, chemical vapor deposition, or metal–organic chemical vapor deposition. To date, the most studied type of self-assembled quantum dots is the InAs/GaAs system, which can be considered as a model system [67]. An atomic force microscope image of the InAs island size distribution is shown in Fig. 2.23 [15].

However, since the key parameter which governs the growth is the lattice-mismatch between the semiconductors (7% in the case of InAs on GaAs), self-assembled quantum dots can be easily obtained with other materials like germanium and silicon [68]. The interest for self-assembled quantum dots relies not only on the easy formation process but also on their potential applications

Fig. 2.23 An atomic force microscope image of InAs islands on GaAs(001) [15]



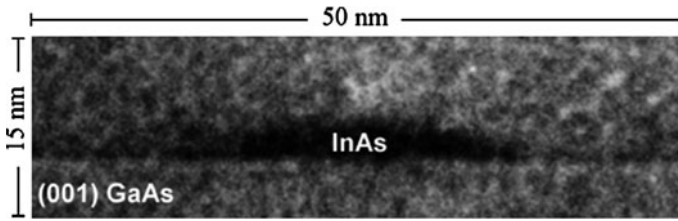


Fig. 2.24 Cross section image of an InAs quantum dot embedded into a GaAs matrix obtained by transmission electron microscopy [62]

due to their compatibility and their possible integration with standard III–V and IV–IV electronics.

The shape, size and compositions of the quantum dots can be significantly modified during regrowth or post-growth annealing or by applying complex growth sequences [15]. In the case of the InAs/GaAs heterosystem, self assembled quantum dots with various shapes have been reported in the literature; including lens shaped quantum dots [69] square-based pyramids [70] or elongated pyramids [71]. Different aspect ratios, defined as the height divided by the base or diameter, have also been reported. The lens-shaped quantum dots are usually rather flat, with an aspect ratio of the order of 1:10, with typical dimension of 2.5 nm height and 25 nm diameter [69]. The pyramids exhibit facets with higher index planes and higher aspect ratios (1:2). Transmission electron microscopy (TEM) structural characterizations show that the InAs dots grown on GaAs roughly have a lens-shaped geometry with a low aspect ratio of ~ 0.1 as seen in Fig. 2.24 [61].

The composition, the strain-relaxation, the interdiffusion and the segregation are strongly dependent on the growth parameters, like the temperature, the ratio between the III–V elements fluxes, the capping procedure etc. It is therefore very difficult to compare quantitatively the results which have been reported in the literature so far. The electronic spectrum of the dots is dependent on all these parameters, and in turn is expected to vary from one system to another.

One drawback of the self-assembled quantum dots as compared to lithography-defined quantum dots is their size distribution, which can put a limitation for device application. The size dispersion, which is inherent to the Stranski–Krastanow growth mode formation, is generally of the order of a few percent around the mean size. The mean size can evidently be varied during the growth process, which opens in turn a route to tune the energy of the confined energy levels [61].

Multiple-layer stacking of islands is often required when implementing QDs in the active region of optical devices to obtain enough interaction between the confined electrons and the electromagnetic field. In this case, a spacer layer determines the size and density of QDs. Below a certain thickness of the spacer (GaAs in this example), the islands align themselves according to the bottom layer and their size increases as we move toward the upper layers. Increasing the thickness of the spacer may result in independent growth of islands with nearly constant size and density in different layers [15].

However another route to tailor the electronic spectrum of the dots is to rely on the electronic coupling that can be achieved by vertical coupling of the quantum dots. This vertical coupling is possible due to the vertical alignment driven by the strain-field induced by one quantum dot. Electronic coupling between stacked layers provides more flexibility for wave function engineering in quantum dots, as it is routinely achieved with quantum wells. The stacking of quantum dots corresponds to the transition between artificial atoms to artificial molecules [61].

Intersublevel transitions offer also great opportunities for the development of new devices in the mid-infrared. By analogy with quantum well intersubband photodetectors, one of the first device applications that have been proposed was the realization of quantum dot infrared photodetectors for infrared detection and imaging. Clearly, one of the anticipated advantages of using quantum dots instead of quantum wells is related to the difference in capture and relaxation mechanisms between the dots and the wells. This should result in an improved responsivity, a lower dark current and a higher operation temperature. Besides, the polarization selection rule for intersublevel absorption differs between quantum dots and quantum wells. Normal incidence operation can therefore be expected with quantum dots. Quantum dots allow also the study of original structures and geometries like lateral quantum dot photodetectors which cannot be investigated with quantum wells [15].

2.5.2 An Overview of Quantum Dots Photodetectors

Detection of terahertz wave like any other electromagnetic radiation may be done by coherent or incoherent techniques. Coherent detection systems such as Schottky diode mixers, nonlinear optical crystals or coatings and gated photoconductive antennas, or switches usually accomplished along with frequency conversion. The coherent techniques despite of good sensitivity need a high degree of sophistication and instrumentation. Incoherent detectors involve heat based devices such as bolometers or those made with pyroelectric crystals. These types of detectors are generally slow and operate at low temperatures. Detectors based on Semiconductor materials (such as doped Ge detectors [72] and photoconductive detectors triggered by femtosecond optical pulses [73]) and heterojunction (such as heterojunction interfacial work function internal photoemission detectors [74], and high-electron mobility transistors operating in the plasma-wave regime [75]) have been also studied and characterized. More recently, quantum-confinement based detectors [76] consist of quantum-well infrared photodetectors (QWIPs) and quantum dot infrared photodetectors (QDIPs) have generated interest. It was observed that a QDIP consisting of a multilayered self-organized In(Ga,Al)As/Ga(Al)As quantum dot active region can detect a broad range of infrared (IR) wavelengths [77–80]. Mid-infrared photoconductivity at around 3 μm has also

been studied for delta-doped InAs/AlGaAs quantum dots for subbands to continuum transitions [81, 82].

The advantages of QDIPs result from three-dimensional carrier confinement in quantum dots. The associated advantages include:

- (1) Intrinsic sensitivity to normal incidence light.
- (2) Long lifetime of photoexcited electrons due to reduced electron–phonon scattering.
- (3) Low dark current due to three-dimensional quantum confinement and reduced thermionic emission.

Intersubband absorption in zero-dimensional quantum dot structures has advantages in optical applications compared with two-dimensional quantum well structures. This is due to their sharp delta-like density of states, the reduced intersubband relaxation times and so lower detector noises in these nanostructures [81, 82]. Intersubband absorption of GaAs-based quantum dot structures has been extensively investigated in recent years. For example, infrared absorption has been reported for charged InGaAs quantum dots for wavelengths higher than 20 μm , and for doped InAs dots in the range of 10–20 μm , respectively. Long-wavelength infrared detection is one of the major applications of self-assembly grown semiconductor quantum dots [83]. Most of long-wavelength infrared detectors are generally limited to the peak position wavelength range of 4–9 μm [84, 85]. A study of the intersubband absorption in InAs/GaAs quantum dots has been done in [84]. The long-wavelength infrared intersubband absorption in $\text{In}_{0.3}\text{Ga}_{0.7}\text{As}/\text{GaAs}$ multiple quantum dots is reported in [83]. With variation of the number of monolayers (between 10 and 60), the peak position wavelength varies in range $\lambda \sim 8.6\text{--}13 \mu\text{m}$. While these QDs have been demonstrated successfully in mid-infrared wavelength photodetectors, the promise of new applications at longer wavelengths in the far-infrared (30–300 μm) or terahertz (1–10 THz) region of the spectrum is providing motivation to extend their operating wavelength [86].

The first observation of mid-infrared photoconductivity with InAs quantum dots was reported in 1997 [61, 81]. Far infrared photoconductivity (17 μm) in self-organized InAs quantum dots was reported in 1998 [87]. The photoresponse remained however very noisy due to the high temperature of the measurement (90 K) and could not be observed for a bias larger than 0.5 V. A short wavelength InGaAs photodetector with InGaP barriers is investigated by Kimet et al. [88]. The photoconductivity was measured at normal incidence. At the peak wavelength of 5.5 μm , the responsivity was 130 mA/W and the detectivity was $4.74 \times 10^7 \text{ cm Hz}^{1/2}/\text{W}$ at 77 K. This figure of merit remains however lower more than two orders of magnitude as compared to GaAs/AlGaAs QWIPs operating at the same wavelength. The reported InAs/GaAs QDIP in [89] has peak at 10 μm and operates at normal incidence. A peak detectivity of $7 \times 10^9 \text{ cm Hz}^{1/2}/\text{W}$ is achieved at 30 K. This value remains much weaker than the achieved value with state of the art quantum well infrared photodetectors. The detectivities of 6×10^8 , $5 \times 10^8 \text{ cm Hz}^{1/2}/\text{W}$ are obtained at room temperature and 80 K, respectively at 9 μm for far infrared photodetector using self-assembled InAs quantum dots [90].

Several groups have reported some results for QDIPs with AlGaAs barriers. Liu et al. have embedded 50 layers of InAs quantum dots with $\text{Al}_{0.33}\text{Ga}_{0.65}\text{As}$ barriers. The reported results have shown that the AlGaAs barriers induce blue shift. At 80 K, a responsivity of 0.1 A/W has observed at 5 μm and bias voltages of ~ 3 V [91]. Another approach consists on using an $\text{Al}_{0.3}\text{Ga}_{0.7}\text{As}$ current blocking barrier between the contacts and the active region where detectivity values, $D^* \sim 3 \times 10^9 \text{ cm Hz}^{1/2}/\text{W}$ at 100 K, were measured for a peaked photoresponse around 3.75 μm [92, 93]. Using AlGaAs blocking barriers, a detectivity of $D^* \sim 10^{10} \text{ cm Hz}^{1/2}/\text{W}$ at 77 K with a photoresponse peaked at 6.2 μm and a 0.7 V bias is reported with responsivity of 14 mA/W [94]. The same authors have reported an InAs QDIP that utilize $\text{In}_{0.15}\text{Ga}_{0.85}\text{As}$ strain-relief cap layers [95]. This device exhibit normal-incidence photoresponse peaks at 8.3 or 8.8 μm for negative or positive bias, respectively. At 77 K and -0.2 V bias, the responsivity is 22 mA/W and the peak detectivity D^* is $3.2 \times 10^9 \text{ cm Hz}^{1/2}/\text{W}$. The highest responsivities have been achieved using lateral quantum dot infrared photodetectors where the carrier transport is shifted to a neighboring channel with high electron mobility. Lee et al. [96] have reported a responsivity of 4.7 A/W at low temperature (10 K) for a 9 V applied bias for the first time.

Recently, Chu et al. [97] have demonstrated an 11 A/W responsivity associated with a resonant photoresponse around 186 meV (6.65 μm) using an InGaAs channel layer. A Ge quantum dot photodetector has been demonstrated using a MOS tunneling structure [98]. The responsivities of presented photodetector in the case of five-period Ge quantum dot are 130, 0.16 and 0.08 mA/W at wavelengths of 820, 1,300 and 1,550 nm, respectively. The device with 20-period Ge quantum dot introduces the responsivity of 600 mA/W at 850 nm and the reported room temperature dark current density is 0.06 mA/cm². The optimized growth of multiple (40–70) layers of self-organized InAs quantum dots separated by GaAs barrier layers in order to enhance the absorption of quantum-dot infrared photodetectors (QDIPs) is investigated in [80]. In devices with 70 quantum-dot layers, at relatively large operating biases (smaller than 1.0 V), the dark current density and the peak responsivity are 10^{-5} A/cm^2 and ~ 0.1 – 0.3 A/W measured for temperature ranges 150–175 K, respectively. The peak detectivity varies in the range of $(6 \times 10^9$ – $10^{11} \text{ cm Hz}^{1/2}/\text{W})$ for temperature range (100–200 K).

A resonant tunneling quantum-dot infrared photodetector has investigated theoretically and experimentally in [12]. In this device, the transport of dark current and photocurrent are separated by the incorporation of a double barrier resonant tunneling heterostructure for each quantum-dot layer. The proposed device uses $\text{In}_{0.4}\text{Ga}_{0.6}\text{As}$ –GaAs quantum dots and has implemented using molecular beam epitaxy. The introduced system was designed to operate at room temperature and 6 μm . Also the measured data exhibit a strong photoresponse peak at 17 μm . The dark current in the tunneling based devices are almost two orders of magnitude smaller than those in conventional devices. Measured dark current values are $1.6 \times 10^{-8} \text{ A/cm}^2$ at 80 K and 1.55 A/cm^2 at 300 K for 1 V applied bias. Measured values of peak responsivity and specific detectivity are 0.063 A/W and $2.4 \times 10^{10} \text{ cm Hz}^{1/2}/\text{W}$, respectively, under a bias of 2 V, at 80 K

for the 6 μm response. For the 17 μm response, the measured values of peak responsivity and detectivity at 300 K are 0.032 A/W and $8.6 \times 10^6 \text{ cm Hz}^{1/2}/\text{W}$ under 1 V bias.

In In(Ga)As/GaAs quantum dots, the intersublevel energy spacings or the energy difference between the dot and continuum states is normally 40–60 meV, which corresponds to the mid-IR and FIR wavelength ranges. In the other words, the upper cutoff wavelength for detection with QDIPs is limited to less than 25 μm [79]. Therefore, the dot heterostructure and/or the dot size need to be engineered for detection at longer wavelengths and in the terahertz range. Bhattacharya and his coworkers [99] have reported the performance characteristics of tunnel QDIPs, incorporating $\text{In}_{0.6}\text{Al}_{0.4}\text{As}$ /GaAs self-organized quantum dots of reduced size in the active region, which exhibit spectral response with peak and cutoff wavelengths of 50 and 75 μm ($\sim 4.0 \text{ THz}$), respectively. The conduction band diagram of an $\text{In}_{0.6}\text{Al}_{0.4}\text{As}$ /GaAs quantum dot layer and the associated resonant tunnel heterostructure for this structure are shown in Fig. 2.25a.

A single 60 Å thick $\text{Al}_{0.1}\text{Ga}_{0.9}\text{As}$ barrier is incorporated before each dot layer to form a quantum well with well-defined final states for the photoexcited electrons.

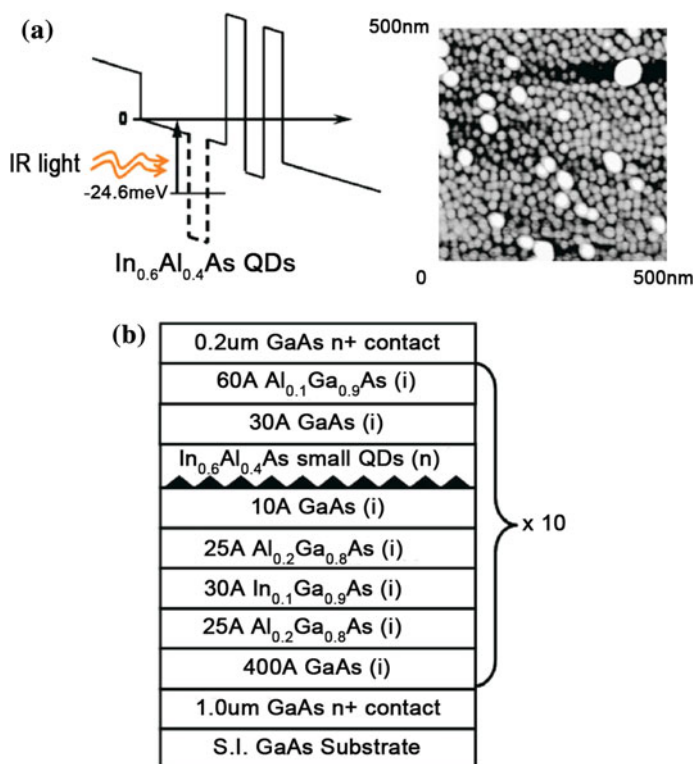


Fig. 2.25 **a** Single period conduction band schematic diagram and AFM image of $\text{In}_{0.6}\text{Al}_{0.4}\text{As}$ /GaAs dots; **b** schematic heterostructure of T-QDIP grown by molecular beam epitaxy [99]

The width of the well region and the composition of the barrier can be varied to tune the final states in resonance with the resonant state of the double barrier heterostructure. For detection of terahertz radiation, the energy spacing between the confined state in the dot and the quasibound states in the well has to be of the order of 10 meV or less. This transition is illustrated in Fig. 2.25a. To achieve this, the $\text{In}_{0.6}\text{Al}_{0.4}\text{As}/\text{GaAs}$ quantum dots have been grown in the active region of the devices, instead of the more conventional InAs dots. Incorporation of Al into the dot material serves two purposes. First, due to the larger band gap of InAlAs, compared to InAs, the bound state energies are closer to the GaAs barrier energy, and hence to the quasibound states in the well. Second, due to the smaller migration rate of Al atoms on the growing surface during epitaxy, the Al-containing islands (dots) are smaller in size compared to InAs dots and the dot confined states are higher in energy.

In this study, the density of $\text{In}_{0.6}\text{Al}_{0.4}\text{As}$ dots ($\sim 3 \times 10^{11} \text{ cm}^{-2}$) is generally an order of magnitude larger than that of InAs dots, which helps to absorb more of the incident radiation. The schematic heterostructure of T-QDIP is shown in Fig. 2.25b.

The energies of the bound states are indicated in Fig. 2.25a. The quantum dots are also doped with Si such that the bound states are occupied.

The dark current density of the device, with the smaller sized InAlAs dots as a function of bias voltage and temperature, is shown in Fig. 2.26. The dark current densities at a bias of 1 V are 4.77×10^{-8} , 2.03×10^{-2} , and 4.09 A/cm^2 at 4.2, 80, and 150 K, respectively. These values are very low compared to other terahertz detectors [74, 100]. This low dark current density is due to the existence of the double barrier tunnel heterostructure. For comparison, the dark current densities in a device with larger sized dots, measured at 80 K, are also included. It is apparent that devices with larger dots are more suitable for high temperature operation.

The spectral response of the tunnel-QDIP with smaller dots at 4.6 K, with bias of 1.0 V, is shown Fig. 2.27a. The peak responsivity is about 0.45 A/W and the wavelength corresponding to this peak is around 50 μm which agrees with the

Fig. 2.26 Measured dark current density as a function of bias and temperature [99]

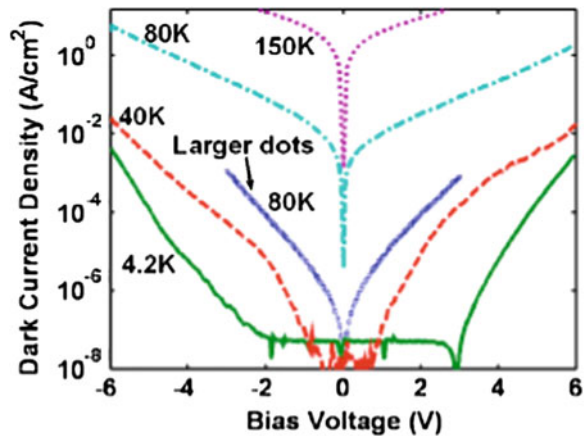
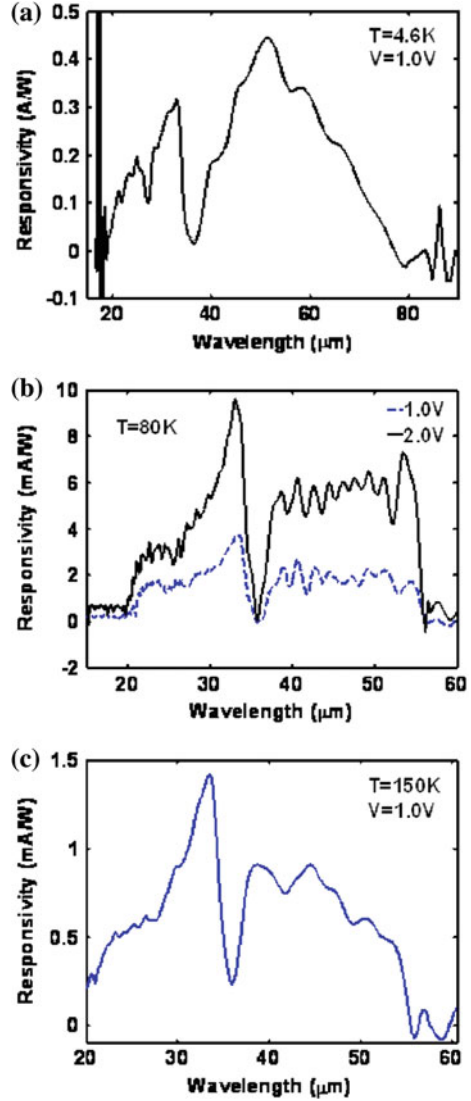


Fig. 2.27 Measured spectral responsivity of T-QDIP at **a** 4.6 K, **b** 80 K, and **c** 150 K under bias of 1 V [99]



calculated energy difference between the QD bound state and the quasibound state in the well of 24.6 meV (50.4 μm). The cutoff wavelength is $\sim 75 \mu\text{m}$, which corresponds to ~ 4.0 THz. The transition between the dot state and the state in the well is expected to be sensitive to normal incidence or s -polarized radiation. This has been verified earlier in QDIPs [79]. In the dot-well system, the states in the well are no longer z confined, but also have a radial component. The dark region (dip) in the spectral response centered at (36 μm) is due to longitudinal optical phonon absorption in GaAs. This same phenomenon has been observed by other GaAs based detectors [74, 101]. The spectral response appears to be fairly broad.

The transition is believed to be from the dot bound states to quasibound states in the well and the spectral width of such transitions will not match the observed full width at half maximum (FWHM) of $\sim 35 \mu\text{m}$, which corresponds to 23 meV. The observed linewidth is attributed to size nonuniformity of the self-organized dots which give rise to linewidths of $\sim 30\text{--}40$ meV in the interband photoluminescence spectra. Figure 2.27b, c show responsivity spectra at higher temperatures from a device with the larger sized $\text{In}_{0.6}\text{Al}_{0.4}\text{As}$ dots. The long-wavelength response is shifted to shorter wavelengths. The device can be operated at a temperature of 150 K, which is high compared to other photon-based terahertz detectors. In order to achieve 1–3 THz operation at reasonably high temperature the dot size needs to be reduced, the size uniformity improved, and the tunnel heterostructure needs to be further optimized to keep the dark current low. The dot size can be reduced by increasing the Al content in the dots and by reducing the growth temperature.

The specific detectivity (D^*) of the devices at different temperatures and applied biases is obtained from the peak responsivity R_p and noise density spectra S_i . The latter is measured with a dual channel fast Fourier transform (FFT) signal analyzer, which displays a FFT spectrum of voltage versus frequency, and a low noise preamplifier. A thick copper plate is used as a radiation shield to provide the dark conditions for the measurements. The value of D^* is calculated from:

$$D^* = R_p A^{1/2} / S_i^{1/2} (\text{cm Hz}^{1/2} / \text{W}) \quad (2.66)$$

where A is the illuminated area of the detector. The measured D^* values are 1.64×10^8 and $4.98 \times 10^7 \text{ cm Hz}^{1/2} / \text{W}$ at 4.6 and 80 K, respectively, under a bias of 1 V.

Hofer and his coworkers have done a work [101] with goal of obtaining emission from interdot transitions in the THz region from quantum dots [102] and from quantum dot cascade emitters [103]. They reported a quantum dot photodetector with two response peaks due to interdot transitions and dot-continuum transitions. Two samples have been used for the investigations. One has 30 dot layers (sample A) and other has 20 layers (sample B). The dot layers of both samples are embedded into a GaAs Matrix of 10 nm width which—for sample B—is Si-doped so that each dot is filled with about one electron. Sample B is provided additionally with thin AlAs layers of 1 nm thickness, 1 nm spaced from the dots to restrict the vertical current (Fig. 2.28). From the relatively small distance between the dots the states in the dots must couple vertically [104].

The measurements show a nonlinear asymmetric behavior with turn-on-voltages of 0.5 and -0.14 V for sample A and 0.66 and -2.5 V for sample B. The dark current is of the order of mA. Sample B shows a smaller dark current than sample A due to the AlAs barriers. The 300 K photoluminescence data-depicted in Fig. 2.29 show for both samples sharp peaks at 994 meV and at 1,021 meV with a FWHM of 57 and 54 meV whereas the intensity for sample B is 7 times higher than for sample A. This can be attributed to the AlAs barriers which improve the carrier capture.

Fig. 2.28 Schematic band diagram showing the structure of the samples [101]

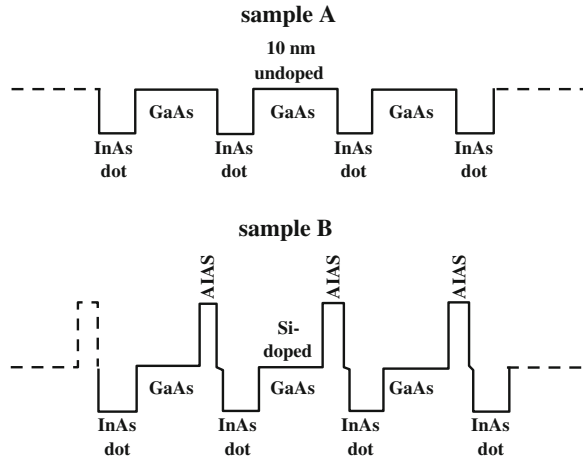
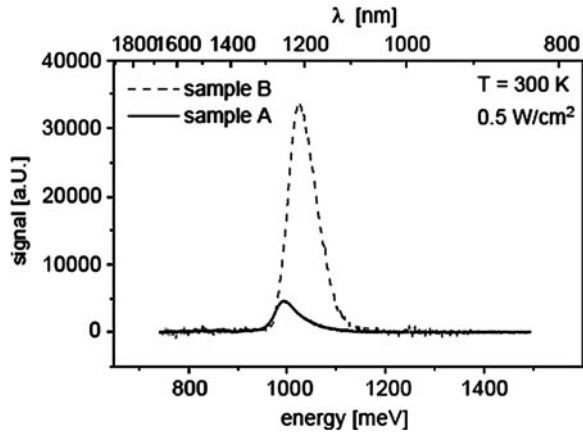


Fig. 2.29 Room temperature photoluminescence spectrum. The peaks show the ground state dot recombination [101]



The spectral dependence of the photoresponse of the detector structure is measured using a standard FTIR spectrometer with a glow-bar infrared source. The samples are measured in normal incidence geometry. In Fig. 2.30 the measured transition from the ground state of the quantum dots to the continuum of samples B and A is depicted. As it is expected the higher transition energy for sample B compared to sample A can be seen since the electrons have to be excited into the higher lying lowest miniband of the AlAs–GaAs superlattice.

In fact, there is an energy difference of 27 meV between the peaks of the two samples. This is in exact agreement with the calculation of the miniband dispersion relation done in the envelope function approximation [105]. The lowest energy level of the first miniband lays 27 meV above the GaAs band edge. Sample B shows also a large signal at zero bias which we ascribe to the built in field between the ionized donors next to the dots and the electrons in the dots. The GaAs matrix of sample A is not doped. Therefore there is no photoresponse signal at the

Fig. 2.30 Photoresponse signal of samples A and B due to ground state-continuum transitions in the quantum dots at different bias voltages, $T = 10\text{ K}$ [101]

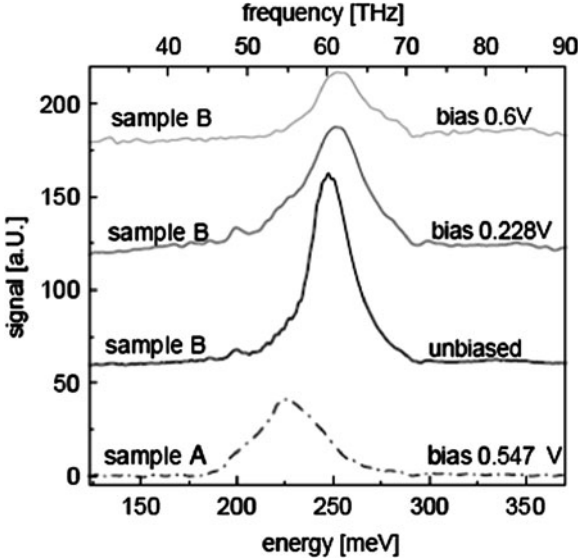
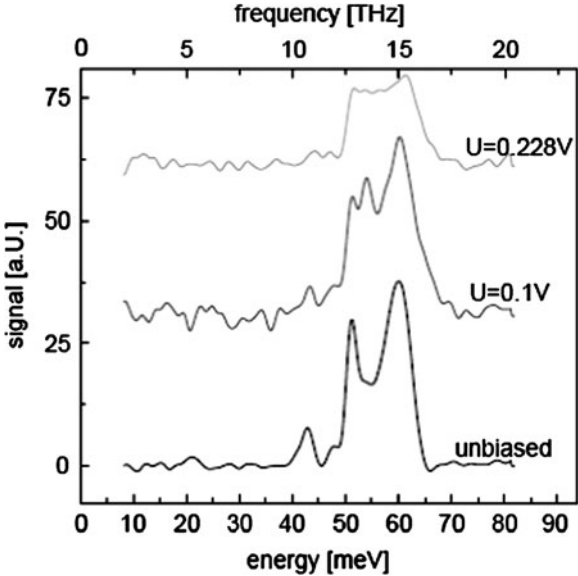


Fig. 2.31 Photoresponse signal of sample B due to interdot transitions in the quantum dots at different bias voltages, $T = 10\text{ K}$ [101]



unbiased state. Figure 2.30 shows for sample B that the signal is getting smaller at higher bias voltages. This is due to the higher dark current which makes the signal smaller. Measurements in a lower frequency range show a broad peak with several features around 55 meV—Fig. 2.31—which can be interpreted as interdot transitions (see also Pan et al. [106]).

The strong normal incidence response supports the interpretation that the observed peaks are from optical transitions in the quantum dots rather than from the two-dimensional wetting layer. Sample A does not show this peak due to the larger dark current in this sample. In contrast to Chu et al. [107] and Pan et al. [106], in this report interdot transitions and bound to continuum transitions for the same sample possible due to the GaAs–AlAs superlattice miniband which reduces the dark current and noise of the detector [108, 109].

For detecting virus, explosives and bio-images with their molecular vibration frequency locating at the 0.1–30 THz frequency range [110–114], a detector which can detect far infrared wavelength is necessary. Although QDIPs have advantages on detecting infrared light, the detection range is limited to the middle infrared (from several micrometers to tens of micrometer). The quantum ring infrared photodetectors (QRIPs) have the potential of high response speed, longer life time, low dark and noise current, and much better three-dimensional confinement than those of QDIPs; it also exhibits the far infrared wavelength detection ability [115]. Lee and his coworkers [116] have demonstrated the In(Ga)As quantum ring terahertz photodetector which has a cutoff wavelength at 175 μm .

In this work QDs and QRs are grown on semi-insulating (100) GaAs substrate using VG V80H MKII solid source MBE equipped with valved cracker sources under As_2 beam. The structure consisted of 800 nm n+ GaAs/50 nm GaAs/2ML InAs QD annealing at 520°C for 10 s/1.14 nm GaAs capping layer/50 nm GaAs/400 nm n+ GaAs (Fig. 2.32). After two steps annealing (Fig. 2.33), the QR structure is completed (Fig. 2.34). The first annealing step of InAs QD is to make the QDs with uniform size and density. The second annealing step after the deposition of GaAs capping layer is to let the In atoms out-diffuse from the central QDs and form the QRs.

The thickness of the GaAs capping layer is the important factor for the QRIPs detection wavelength [116].

Figure 2.35 shows PL spectra of various samples with different GaAs capping layer thickness. The thinner the capping layer, the closer the PL peak energy is to the GaAs bandgap. It means that there is opportunity to detect the long wavelength infrared radiation.

Fig. 2.32 QRIP device structure [116]

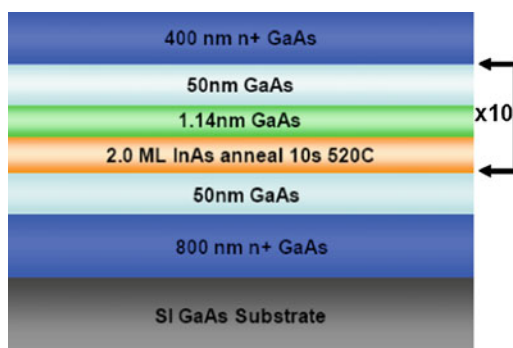


Fig. 2.33 Two steps annealing process to form the quantum ring [116]

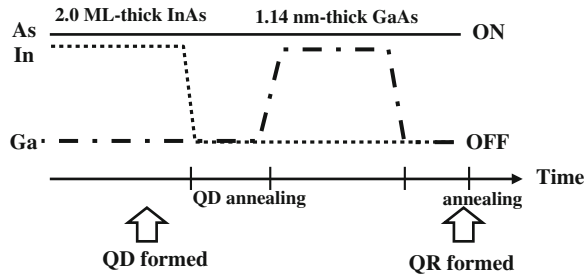


Fig. 2.34 Formation of the quantum ring from the quantum dot [116]

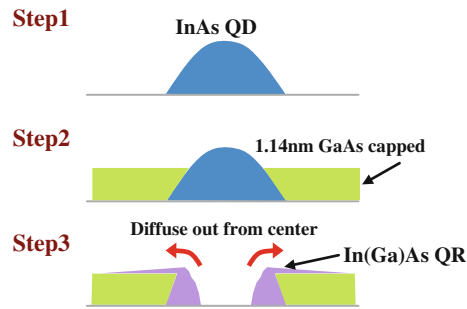


Fig. 2.35 PL Spectra of QD with different GaAs capping layer thickness [116]

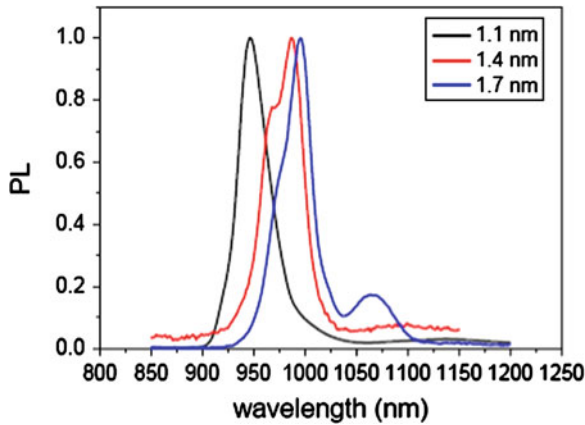
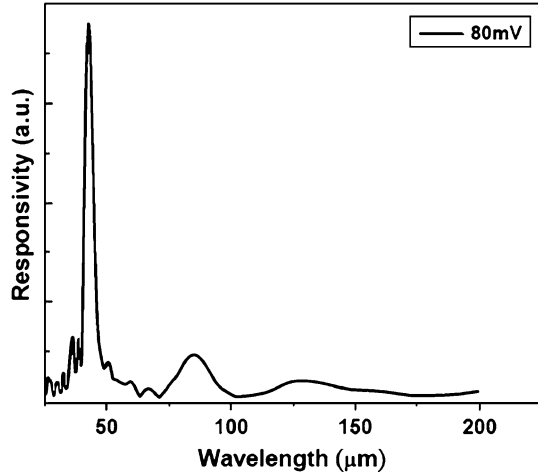


Figure 2.36 shows the responsivity of QRIP at a bias of 80 mV and temperature 8 K. It is very clear from the figure that the QRIPs can detect infrared signal at three ranges, i.e., 45–75, 75–100 and 100–175 μm .

The overview presented above about QDIP shows that there are several challenges in terahertz spectra photodetection which can be categorized as follow:

1. In general, the detection range of QDIPs is limited to mid-infrared.
2. In order to achieve terahertz operation in dot-well system, the dot size needs to be reduced.

Fig. 2.36 Repsonivity of QRIP with 1.14 nm GaAs capping layer thickness [116]



3. Using the 2D states in quantum terahertz photodetection systems leads to decreasing the optical gain and so responsivity.
4. The practical realization of terahertz quantum dot photodetector needs some efforts to be done.

2.5.3 Ultra-High Detectivity Room Temperature THz-IR Photodetector Based on Resonant Tunneling Spherical Centered Defect Quantum Dot

There are several interesting published works to overcome the existing problems in terahertz and long wavelength photodetection. One of the important features of these devices is the ability of detectors in operating at room temperature. Unfortunately, there have not been a suitable proposal for working in room temperature and holding acceptable other characteristics until now. For this reason in this part we describe a quantum dot-based structure for operating at room temperature as well as other high-level characteristics.

According to traditional quantum size effect idea, operating in intersubband-long-IR wavelengths requires large size of quantum structure which leads to low sheet density of quantum dots in each layer in optoelectronic devices. On the other hand, the absorption peak weakens when the resonant frequency is shifted to lower energies (long wavelengths). The maximum reported value for absorption coefficient is about $1.7 \times 10^4 \text{ cm}^{-1}$ at 45 μm resonant wavelength [117]. It is obvious that these problems degrade device performances [118]. So it will be interesting to obtain long wavelength transition resonances without increasing the size of the quantum structure and increasing of the absorption peak in lower energies [119]. We show that with introducing a defect in center of quantum dot, it will be

possible to increase the absorption coefficient of the proposed structure without increasing the dot size [119–123].

The next motivation of this section is to explore the possibility of extending the detection wavelength of QDIP to terahertz wavelengths. Improving the QDIPs' performance depends fundamentally on minimizing the leakage (dark) current which plagues all light detectors. Three major factors contribute to the existence of the dark current. First factor is the sequential tunneling from between quantum wells through the barrier layer. The tunneling actually has to be mediated by a 'third party', such as a phonon or another electron and is fairly independent of temperature and is thought to dominate below 30 K. Especially in the quantum dot structures, this term is much negligible due to phonon bottleneck effect. Secondly, there is thermally assisted tunneling or field induced emission, which involves thermal excitation within the well followed by tunneling into the continuum. The final contribution is called thermionic emission in which there is direct excitation into the continuum band. It is found that both of the sequential tunneling and the thermionic emission contributions to the dark current increase as the wavelength of the detector extends from the mid- to the far-infrared [86, 124].

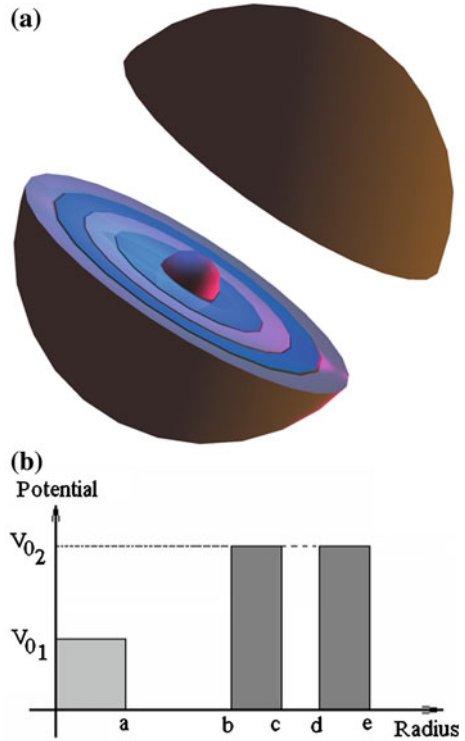
In conventional bound-continuum terahertz photodetectors, the electron energy level will be closer to the top of the quantum well. In fact, the energy of the incoming photons may be of the order of the thermal broadening of the electron distribution. Therefore all the mentioned contributions to the dark current may be expected to increase [86, 124].

Intersubband transitions in GaN-based hetrostructures have been the topic of extensive researches for their advantages. Broad wavelength range and high-temperature operation are available in these structures [10]. In this part, we introduce a GaN-based resonant tunneling spherical centered defect quantum dot (RT-SCDQD) to increase the responsivity, decrease the dark current and enhancement of the detectivity in THz range. It will be shown that the responsivity increases due to increasing the absorption coefficient in SCDQD structure. Since the deep intersublevel transitions, which are achievable in wide conduction band offset material (GaN/AlGaN), increase the activation energy, so the second and third terms of the dark current are going to be decreased. In order to collect the electrons from deep excited level, a double barrier structure, which resonances with this level is jointed to the quantum dot structure. This structure cancels the escape of ground state electrons through the tunneling, leading to ultra small ground state dark current.

2.5.3.1 Centered Defect Quantum Dot-Based Photodetector Structure and Simulations

The introduced basic cell structure, resonant tunneling spherical centered defect quantum dot (RT-SCDQD), for room temperature THZ IR-photodetector is illustrated in Fig. 2.37a [125]. In this structure, we consider a spherical quantum dot with radius b . Then a spherical defect with radius a inserted in center of dot

Fig. 2.37 Potential distribution of RT-SCDQD, **a** 3-D scheme and **b** potential distribution [125]



[119]. Finally a resonant tunneling double barrier is attached to the system. Also, for mathematical evaluation of the structure potential distribution of the introduced structure is illustrated in Fig. 2.37b. The introduced structure is based on AlGaIn/GaN heterostructure.

The introduced centered defect quantum dot structure (Fig. 2.38a) may be implemented with a method based on current implementation technologies (MBE, Ion implantation and Stranski–Krastanov) [126]. In this method, first, a thin layer with thickness of $2 \times$ dot radius (GaN) is grown on the substrate by MBE (Fig. 2.38b). Then a $\sim 200 \text{ nm} \times 200 \text{ nm}$ window is introduced on grown dot layer by masking technique. Defect material particles (Ga + N + Al) are bombarded to considered defect region in dot by ion implantation technique. The temperature in annealing form is applied for defect construction. By applying controlled temperature and due to the inherent strain between layers and substrate, the layers can become separated as quantum dot islands just like Stranski–Krastanov mode (Fig. 2.38c).

In this section mathematical formulation for description of the electrical and optical properties of RT-SCDQD is presented. For this purpose effective mass approximation in spherical coordinate is considered. The Schrödinger equation in the case of slowly varying envelope approximation in spherical coordinate is given as follows.

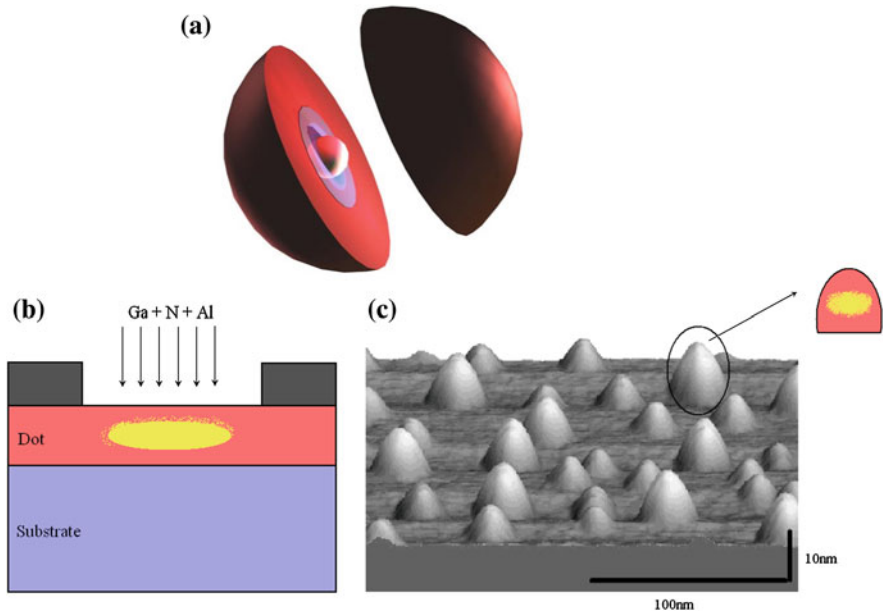


Fig. 2.38 **a** SCDQD structure, **b** Ion implantation of defect, and **c** forming of defected quantum dot islands [119, 126]

$$\left\{ -\frac{\hbar^2}{2m_i^*} \left[\frac{1}{r} \frac{\partial^2}{\partial r^2} r + \frac{1}{r^2 \sin \theta} \frac{\partial}{\partial \theta} \left(\sin \theta \frac{\partial}{\partial \theta} \right) + \frac{1}{r^2 \sin^2 \theta} \frac{\partial^2}{\partial \phi^2} \right] + V_i(r) \right\} \Psi(r, \theta, \phi) = E \Psi(r, \theta, \phi) \quad (2.67)$$

where

$$m_i^* = \begin{cases} m_0^* & 0 < r < a \\ m_1^* & a < r < b \\ m_2^* & b < r < c \\ m_3^* & c < r < d \\ m_4^* & d < r < e \\ m_5^* & e < r \end{cases} \quad \text{and} \quad V_i(r) = \begin{cases} V_{01} & 0 < r < a \\ 0 & a < r < b \\ V_{02} & b < r < c \\ 0 & c < r < d \\ V_{02} & d < r < e \\ 0 & e < r \end{cases}$$

are effective mass and potential distribution, respectively. Using the standard method based on separation of variables the following solution for wave function is proposed.

$$\Psi_{n\ell m} = R_{n\ell}(r) Y_{\ell m}(\theta, \phi) \quad (2.68)$$

Considering the proposed solution for wave function, the angular dependent term as spherical harmonics is given in the following [127].

$$Y_{\ell m}(\theta, \phi) = (-1)^m \left[\frac{(2\ell + 1)(\ell - m)!}{4\pi(\ell + m)!} \right]^{\frac{1}{2}} P_{\ell}^m(\cos \theta) e^{im\phi}, \quad (2.69)$$

After substituting of Eq. 2.68 into 2.67 and mathematical manipulation the radial part of the wave function is solution of the following differential equation.

$$r^2 \frac{d^2 R}{dr^2} + 2r \frac{dR}{dr} + \left\{ \frac{2m_i^*}{\hbar^2} [E - V_i(r)] r^2 - \ell(\ell + 1) \right\} R = 0. \quad (2.70)$$

Solution of Eq. 2.70 for $E < V_{01}$ is given as:

$$R = \begin{cases} [C_{01} i_l(k_0 r)] \sqrt{\frac{2}{\pi}} & 0 < r < a \\ [C_{11} j_l(k_1 r) + C_{12} n_l(k_1 r)] \sqrt{\frac{2}{\pi}} & a < r < b \\ [C_{21} i_l(k_2 r)] \sqrt{\frac{2}{\pi}} + [C_{22} k_l(k_2 r)] \sqrt{\frac{2}{\pi}} & b < r < c \\ [C_{31} j_l(k_3 r) + C_{32} n_l(k_3 r)] \sqrt{\frac{2}{\pi}} & c < r < d \\ [C_{41} i_l(k_4 r)] \sqrt{\frac{2}{\pi}} + [C_{42} k_l(k_4 r)] \sqrt{\frac{2}{\pi}} & d < r < e \\ [C_{51} j_l(k_5 r) + C_{52} n_l(k_5 r)] \sqrt{\frac{2}{\pi}} & e < r \end{cases}, \quad (2.71)$$

Also, for $E < V_{01}$, we have:

$$R = \begin{cases} [C_{01} j_l(k_0 r)] \sqrt{\frac{2}{\pi}} & 0 < r < a \\ [C_{11} j_l(k_1 r) + C_{12} n_l(k_1 r)] \sqrt{\frac{2}{\pi}} & a < r < b \\ [C_{21} i_l(k_2 r)] \sqrt{\frac{2}{\pi}} + [C_{22} k_l(k_2 r)] \sqrt{\frac{2}{\pi}} & b < r < c \\ [C_{31} j_l(k_3 r) + C_{32} n_l(k_3 r)] \sqrt{\frac{2}{\pi}} & c < r < d \\ [C_{41} i_l(k_4 r)] \sqrt{\frac{2}{\pi}} + [C_{42} k_l(k_4 r)] \sqrt{\frac{2}{\pi}} & d < r < e \\ [C_{51} j_l(k_5 r) + C_{52} n_l(k_5 r)] \sqrt{\frac{2}{\pi}} & e < r \end{cases}, \quad (2.72)$$

where

$$\begin{cases} \kappa_0 = \sqrt{\frac{2m_0^*(V_{01}-E)}{\hbar^2}} & 0 < r < a \\ \kappa_0 = \sqrt{\frac{2m_0^*(E-V_{01})}{\hbar^2}} & 0 < r < a \\ \kappa_1 = \sqrt{\frac{2m_1^*E}{\hbar^2}} & a < r < b \\ \kappa_2 = \sqrt{\frac{2m_2^*(V_{02}-E)}{\hbar^2}} & b < r < c \\ \kappa_3 = \sqrt{\frac{2m_3^*E}{\hbar^2}} & c < r < d \\ \kappa_4 = \sqrt{\frac{2m_4^*(V_{02}-E)}{\hbar^2}} & d < r < a \\ \kappa_4 = \sqrt{\frac{2m_5^*E}{\hbar^2}} & e < r \end{cases}.$$

In above equations n , ℓ , and m are integer values. Now, for extraction of the eigenvalues, eigenfunctions and the transmission coefficient of the proposed system, the obtained solution for the Schrödinger equation should satisfy the following normalization and boundary conditions.

$$\begin{aligned}
 & \int_0^{\infty} dr r^2 R_{n\ell}^2(r) = 1 \\
 & \begin{cases} R_{0 < r < a}(a) = R_{a < r < b}(a) \\ \left. \frac{1}{m_0^*} \frac{dR_{0 < r < a}}{dr} \right|_{r=a} = \left. \frac{1}{m_1^*} \frac{dR_{a < r < b}}{dr} \right|_{r=a} \\ R_{a < r < b}(b) = R_{b < r < c}(b) \\ \left. \frac{1}{m_1^*} \frac{dR_{a < r < b}}{dr} \right|_{r=b} = \left. \frac{1}{m_2^*} \frac{dR_{b < r < c}}{dr} \right|_{r=b} \\ R_{b < r < c}(c) = R_{c < r < d}(c) \\ \left. \frac{1}{m_2^*} \frac{dR_{b < r < c}}{dr} \right|_{r=c} = \left. \frac{1}{m_3^*} \frac{dR_{c < r < d}}{dr} \right|_{r=c} \\ R_{c < r < d}(d) = R_{d < r < e}(d) \\ \left. \frac{1}{m_3^*} \frac{dR_{c < r < d}}{dr} \right|_{r=d} = \left. \frac{1}{m_4^*} \frac{dR_{d < r < e}}{dr} \right|_{r=d} \\ R_{d < r < e}(e) = R_{e < r}(e) \\ \left. \frac{1}{m_4^*} \frac{dR_{d < r < e}}{dr} \right|_{r=e} = \left. \frac{1}{m_5^*} \frac{dR_{e < r}}{dr} \right|_{r=e} \end{cases} ,
 \end{aligned}$$

Now, based on the boundary conditions, we develop and use the transfer matrix method (TMM) to obtain the transmission coefficient for the proposed system. For this purpose, we rewrite the boundary conditions in the form of dynamic matrices as follows

$$\begin{aligned}
 \begin{bmatrix} C_{11} \\ C_{12} \end{bmatrix} &= P_{1,2} \times \begin{bmatrix} C_{21} \\ C_{22} \end{bmatrix} \\
 \begin{bmatrix} C_{21} \\ C_{22} \end{bmatrix} &= P_{2,3} \times \begin{bmatrix} C_{31} \\ C_{32} \end{bmatrix} \\
 \begin{bmatrix} C_{31} \\ C_{32} \end{bmatrix} &= P_{3,4} \times \begin{bmatrix} C_{41} \\ C_{42} \end{bmatrix} \\
 \begin{bmatrix} C_{41} \\ C_{42} \end{bmatrix} &= P_{4,5} \times \begin{bmatrix} C_{51} \\ C_{52} \end{bmatrix},
 \end{aligned} \tag{2.74}$$

where

$$\begin{aligned}
 & p_{u,u+1} = D \\
 & \times \left[\left(n'_i(\kappa_u r) i_i(\kappa_{u+1} r) - \frac{m_u^* \kappa_{u+1}}{m_{u+1}^* \kappa_u} n_l(\kappa_u r) i'_l(\kappa_{u+1} r) \right) \left(\frac{\pi}{2} \right) \left(n'_i(\kappa_u r) k_l(\kappa_{u+1} r) - \frac{m_u^* \kappa_{u+1}}{m_{u+1}^* \kappa_u} n_l(\kappa_u r) k'_l(\kappa_{u+1} r) \right) \right] \\
 & \left[\left(\frac{m_u^* \kappa_{u+1}}{m_{u+1}^* \kappa_u} j_i(\kappa_u r) i'_l(\kappa_{u+1} r) - j'_l(\kappa_u r) i_l(\kappa_{u+1} r) \right) \left(\frac{\pi}{2} \right) \left(\frac{m_u^* \kappa_{u+1}}{m_{u+1}^* \kappa_u} j_i(\kappa_u r) k'_l(\kappa_{u+1} r) - j'_l(\kappa_u r) k_l(\kappa_{u+1} r) \right) \right] \begin{cases} \text{if } u = 1 \Rightarrow r = b \\ \text{if } u = 3 \Rightarrow r = d \end{cases} \\
 & D = 1 / (j_l(\kappa_u r) n'_l(\kappa_u r) - j'_l(\kappa_u r) n_l(\kappa_u r))
 \end{aligned}$$

for odd values of u and

$$p_{u,u+1} = D \times \left[\begin{array}{l} \left(\frac{\pi}{2} \right) \left(k'_l(\kappa_u r) j_l(\kappa_{u+1} r) - \frac{m_u^* \kappa_{u+1}}{m_{u+1}^* \kappa_u} k_l(\kappa_u r) i'_l(\kappa_{u+1} r) \right) \left(\frac{\pi}{2} \right) \left(k'_l(\kappa_u r) n_l(\kappa_{u+1} r) - \frac{m_u^* \kappa_{u+1}}{m_{u+1}^* \kappa_u} k_l(\kappa_u r) n'_l(\kappa_{u+1} r) \right) \\ \left(\frac{m_u^* \kappa_{u+1}}{m_{u+1}^* \kappa_u} i_l(\kappa_u r) j'_l(\kappa_{u+1} r) - i'_l(\kappa_u r) i_l(\kappa_{u+1} r) \right) \left(\frac{m_u^* \kappa_{u+1}}{m_{u+1}^* \kappa_u} i_l(\kappa_u r) n'_l(\kappa_{u+1} r) - i'_l(\kappa_u r) n_l(\kappa_{u+1} r) \right) \end{array} \right] \left| \begin{array}{l} \text{if } u=2 \Rightarrow r=c \\ \text{if } u=4 \Rightarrow r=e \end{array} \right.$$

$$D = 2 / (\pi (i_l(\kappa_u r) k'_l(\kappa_u r) - i'_l(\kappa_u r) k_l(\kappa_u r)))$$

for even values of u , respectively.

Thus, after multiplication of all matrices obtained in previous relations, one can find the following transfer matrix describing input–output relation of the proposed structure.

$$\begin{bmatrix} C_{11} \\ C_{12} \end{bmatrix} = M \times \begin{bmatrix} C_{51} \\ C_{52} \end{bmatrix}, \quad (2.75)$$

where $M = P_{1,2} \times P_{2,3} \times P_{3,4} \times P_{4,5}$.

In order to calculate the transmission coefficient of resonant double barrier, for description of the forward and backward traveling waves for obtaining of the propagation matrices, we must explain the Bessel Functions interms of the Hanckel forms as follows:

$$\begin{aligned} C_{11} j_l(\kappa_1 r) + C_{12} n_l(\kappa_1 r) &= \alpha_{11} H_l^{(1)} + \alpha_{12} H_l^{(2)} \\ C_{51} j_l(\kappa_5 r) + C_{52} n_l(\kappa_5 r) &= \alpha_{51} H_l^{(1)} + \alpha_{52} H_l^{(2)}, \end{aligned} \quad (2.76)$$

Considering $j_l(x) = \frac{1}{2} (H_l^{(1)}(x) + H_l^{(2)}(x))$, $n_l(x) = \frac{1}{2i} (H_l^{(1)}(x) - H_l^{(2)}(x))$ [127] and Eq. 2.76 the transfer matrix relation (Eq. 2.75) can be converted as follows:

$$\begin{bmatrix} \alpha_{11} \\ \alpha_{12} \end{bmatrix} = \Gamma \times \begin{bmatrix} \alpha_{51} \\ \alpha_{52} \end{bmatrix}, \quad (2.77)$$

where

$$\Gamma = \left(\frac{1}{2} \right) \begin{bmatrix} (M_{11} + M_{22}) + i(M_{12} - M_{21}) & (M_{11} - M_{22}) - i(M_{12} + M_{21}) \\ (M_{11} + M_{21}) + i(M_{12} - M_{22}) & (M_{11} + M_{22}) - i(M_{12} - M_{21}) \end{bmatrix}.$$

So, the transmission coefficient can be obtained as follows:

$$T(E) = \frac{1}{|\Gamma_{11}|^2}. \quad (2.78)$$

After extraction of the sublevel energies, their corresponding wave functions and the transmission coefficient are obtained. Also, the linear absorption coefficient ($\alpha(\omega)$) for the intersublevel transitions can be clearly calculated by computing the optical susceptibility through the density matrix approach [85, 117, 128] as follows:

$$\alpha(\omega) = \frac{4\pi\omega e^2}{V_0 \hbar c \epsilon_0 \sqrt{\epsilon_r}} \sum_{i,j} |d_{ij}|^2 \times \{f(E_i) - f(E_j)\} \times \frac{\gamma_{ij}}{\gamma_{ij}^2 + (\omega - \omega_{ij})^2} \quad (2.79)$$

where ω , e , V_0 , c , ϵ_0 , ϵ_r , $|d_{ij}| (= |\langle \psi_j | r | \psi_i \rangle|)$, $f(E)$, γ_{ij} ($1/\tau_{ij}$), ω_{ij} are photon frequency, electron charge, volume of quantum dot, speed of light, permittivity of vacuum, relative permittivity of semiconductor, dipole transition matrix element (electron transition $i \rightarrow j$), Fermi–Dirac distribution, relaxation rate (inverse of relaxation time), and transition frequency (resonance frequency between two electronic states), respectively. In above equation Lorentzian broadening is considered [83, 128]. The Fermi energy level is obtained by inverse numerical solution of the following equation [129].

$$N_d = \frac{2}{V_0} \sum_i \{1 + \exp[(E_i - F_c)/k_B T]\}^{-1}, \quad (2.80)$$

where N_d , V_0 , E_i , F_c , k_B and T are electron density, volume of spherical dot, sublevel energy, Fermi energy level, the Boltzman constant and temperature, respectively. To determine precisely the Fermi energy level in calculating the above equation, all of the energy levels within a dot should be included.

The simple schematic view of the QDIP based on RT-SCDQD cells is shown in Fig. 2.39. The RT-SCDQD layers are separated by un-doped GaN spacer layers.

The material and structural parameters of the proposed RT-SCDQD based THZ IR-photodetector are given in Table 2.2 [15, 130–132].

In the following, optical and electrical simulated results of the introduced RT-SCDQD based THZ IR-photodetector are presented and discussed. The simulation consists of two parts. First, we investigate the linear absorption coefficient of the introduced SCDQD structure and the effect of parameters of the introduced defect on enhancement of the absorption coefficient is studied. In this study the effect of defect size on the energy levels, wave functions, dipole matrix element and absorption coefficient is discussed. In the second section we describe the performance of the RT-SCDQD photodetector. The effect of defect and double

Fig. 2.39 Schematic view of the QDIP structure based on RT-SCDQD [102]

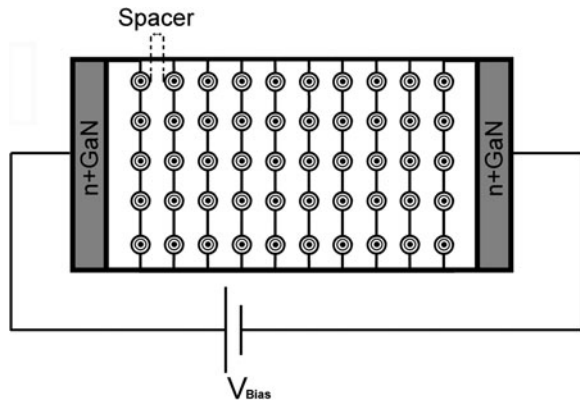


Table 2.2 Material and structural parameters of RT-SCDQD based THZ IR-photodetector [15, 130–132]

$\text{Al}_x\text{Ga}_{1-x}\text{N}$ parameters	Unit	Value
Electron effective mass (m^*)	m_0	$0.252x + 0.228$
Band gap ($E_g(x)$)	eV	$6.13x + (1 - x) \times 3.42 - x(1 - x)$
Band offset ($\Delta E_c(x)$)	eV	$0.7 \times [E_g(x) - E_g(0)]$
Typical Relaxation time (τ)	fs	100
Number density of carriers (N_w)	m^{-3}	1×10^{24}
Electron mobility (μ)	cm^{-2}/Vs	2×10^3
Electron saturation velocity (v_s)	m/s	2×10^5
Recapture life time (τ_r)	s	1×10^{-12}
Surface density of QD (Σ_{QD})	$1/\text{m}^2$	1×10^{14}
Band width (Δf)	Hz	1
Radius of detector (r)	μm	200
Relative dielectric constant (ϵ_r)	–	$8.5x + 10.4(1 - x)$
Number of QD layers (N_{QD})	–	10
Capture probability (p_c)	–	0.001
Fill factor (F)	–	0.35

barrier resonant tunneling structure on improvement of responsivity and detectivity is provided.

In Fig. 2.40, we illustrate the effect of defect size on ground and first excited states. The defect mole fraction is considered as a parameter. It is observed that with increasing of the defect size the energy levels are increased but difference between the energy levels is decreased. The illustrated decreasing in difference of energy levels with increasing defect size is related to the fact that the ground energy level is affected more than the first excited level [119]. Finally with increasing of the mole fraction difference between energy levels also is decreased.

Fig. 2.40 Energy levels (ground and first excited states) versus defect sizes (\AA) with different mole fraction of introduced defect ($b = 70 \text{ \AA}$, $xb = 0.3$) [125]

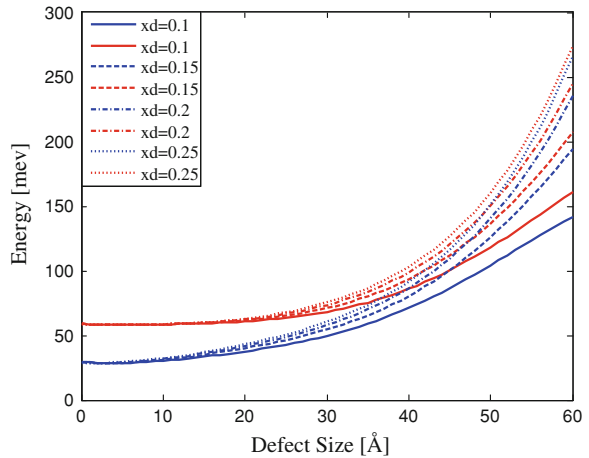
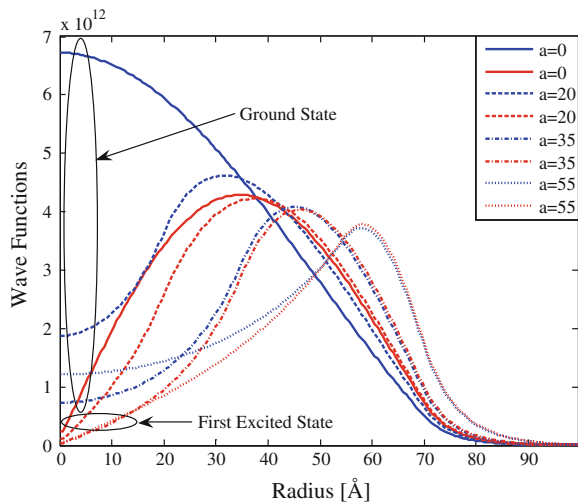


Fig. 2.41 Wave functions (ground and first excited states) versus dot radius (\AA) with different defect sizes ($b = 70 \text{ \AA}$, $xb = 0.3$, $xd = 0.15$) [125]



The electron wave function of the structure is illustrated in Fig. 2.41. The wave function inside defect with increasing of defect size is decreased. With increase of defect size, peak of the wave function is shifted to the right hand side within distance between defect and dot. This phenomenon is due to potential barrier effect on electron wave function that is concluded to shifting of the maximum probability of electron [119].

In the Fig. 2.42, the effect of defect size and mole fraction on dipole transition matrix element is investigated. As it is observed with increasing the defect size and also defect height the dipole transition matrix element is increased [119]. Decreasing of the matrix element in large defect size is owing to tunneling leakage

Fig. 2.42 Dipole transition matrix element ($\langle \psi_f | r | \psi_g \rangle$) versus defect width ($b = 70 \text{ \AA}$, $xb = 0.3$) [125]

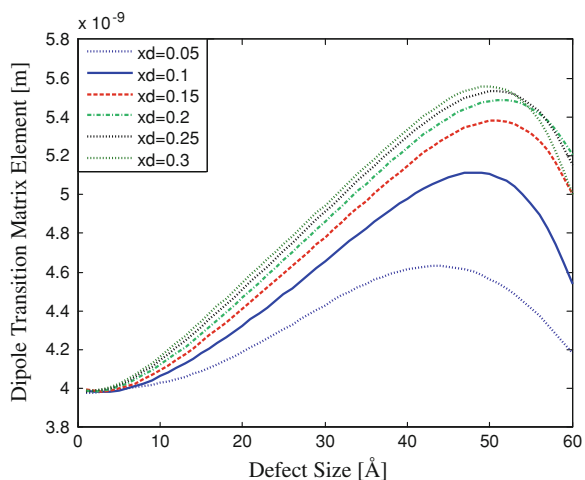
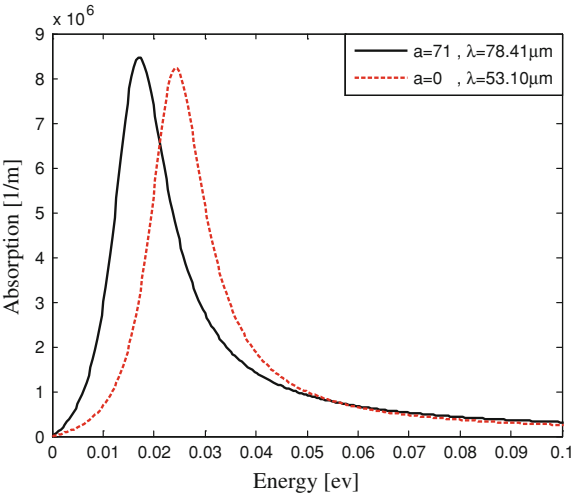


Fig. 2.43 Absorption coefficient (Ground state → First excited state) versus pump photon energy
($b = 80$, $x_b = 0.3$, $x_d = 0.1$)
[125]



of the wave functions into dot barrier and defect. So, there is an optimum value of defect size for maximum matrix element.

In Fig. 2.43 the effect of defect size on SCDQD absorption coefficient is presented. The absorption coefficient is calculated for ground to first excited state transition. It is shown that with increasing of the defect size, the absorption peak is increased and a red shift is observed. The observed red shift is due to pushing the energy levels up and decreasing the difference between energy levels. As it mentioned before, increasing the defect size increases the dipole transition matrix element and hence increases the peak of absorption coefficient. It is noticeable that the absorption peak increases despite of shifting to lower energies.

Table 2.3 shows the absorption coefficient peak in different defect and dot sizes for the same resonance wavelength. It is found that with the larger defect size, higher absorption coefficient is achievable in small dot size.

As it is observed the SCDQD has large absorption coefficient at long wavelength in the small quantum dot size, thus we use this structure as a basic THZ IR-photodetector cell (Fig. 2.39).

Now based on the proposed basic cell in the following, we present simulated results of the THZ-IR photodetector system. Table 2.4 illustrates the optimal parameters used for obtaining characteristics of the THZ-IR photodetector.

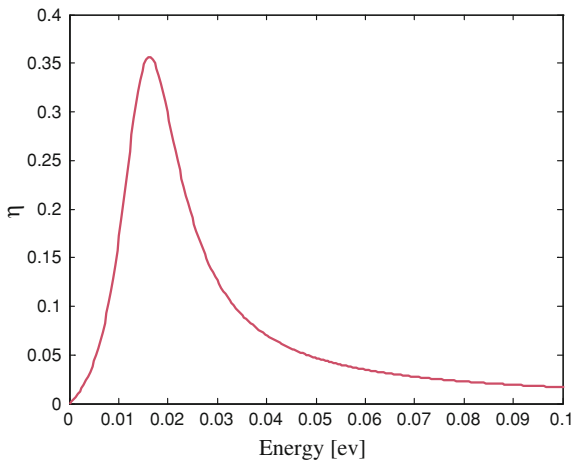
Table 2.3 Absorption coefficient peaks (Ground state → First excited state) for different SCQD-structural parameters
($x_b = 0.3$, $x_d = 0.1$) [125]

Structure parameters			Absorption(1/m)
$a(\text{\AA})$	$b(\text{\AA})$	$\lambda(\mu\text{m})$	
55	70	83.53	7.34×10^6
40	70	82.98	6.79×10^6
30	79	82.09	5.68×10^6
20	90	80.62	3.04×10^6
0	100	80.59	1.05×10^6

Table 2.4 Design parameters for simulation of THZ IR-photodetector based on RT-SCDQD [125]

Structure parameter	Unit	Value
<i>a</i>	M	55×10^{-10}
<i>b</i>	M	70×10^{-10}
<i>c</i>	M	90×10^{-10}
<i>d</i>	M	110×10^{-10}
<i>e</i>	M	130×10^{-10}
Defect mole fraction (<i>x_d</i>)	–	0.1
Barrier mole fraction (<i>x_b</i>)	–	0.3
Operation temperature	K	83
Spacer layer width	M	130×10^{-10}
Applied voltage	V	2

Fig. 2.44 Absorption quantum efficiency of RT-SCDQD based THZ-IR photodetector versus photon energy [125]



Absorption quantum efficiency versus photon energy is illustrated in Fig. 2.44. It is shown that there is a maximum value at 83 μm. It is clear that there is direct relationship between maximum value of the absorption coefficient and the quantum efficiency.

The calculated tunneling probability for the RT-SCDQD basic cell is illustrated in Fig. 2.45. The proposed double barrier parameters are designed such that the resonance energy to be close to first excited state of the quantum dot.

Responsivity of the introduced structure is illustrated in Fig. 2.46. It is observed that the reported large value related to the following factors.

1. For the proposed structure the calculated quantum efficiency is increased considerably due to larger absorption coefficient.
2. Probability of electron escaping is increased in the proposed system owing to decrease of the collection time of electron using resonant double barrier.
3. Optical gain for the proposed photodetector is increased considerably due to inherent properties of quantum dots.

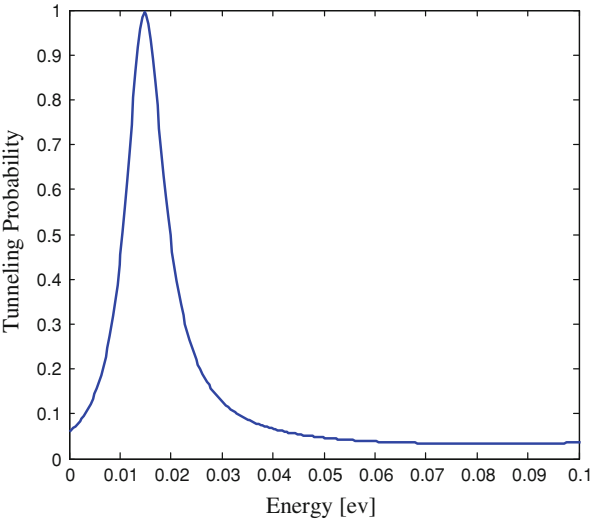
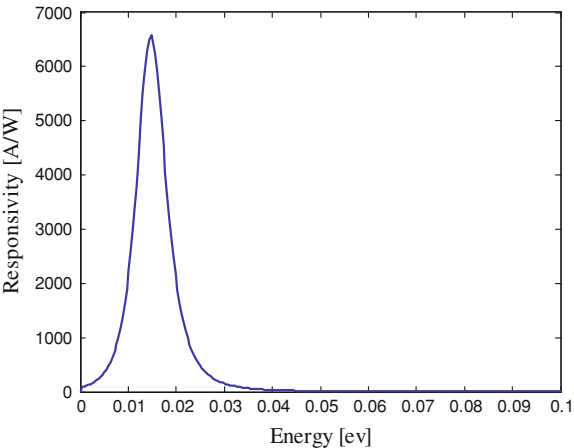


Fig. 2.45 The tunneling probability of RT-SCDQD versus photon energy [125]

Fig. 2.46 Responsivity of RT-SCDQD based THZ-IR photodetector versus photon energy [125]



Dark current curves of RT-SCDQD based THZ-IR photodetector versus bias voltage at various temperatures is illustrated in Fig. 2.47. It is shown that with increasing of the temperature the appeared dark current is increased strongly. This increase in the dark current basically related to thermionic effect.

For the proposed system the detectivity is illustrated in Fig. 2.48. The illustrated detectivity is considerable higher than reported values in similar situations.

The calculated detectivity and NE Δ T parameters of proposed structure (RT-SCDQD-THZ-IR photodetector) are compared with conventional structure (QD-THZ-IR photodetector) in Table 2.5. It is shown that the proposed complete

Fig. 2.47 Dark current curves of RT-SCDQD based THZ-IR photodetector versus bias voltage at various temperatures [125]

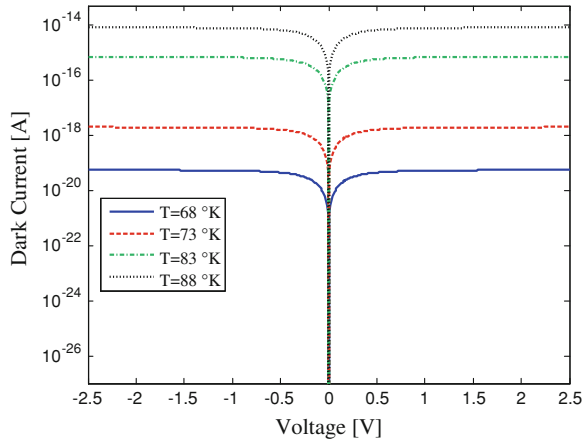
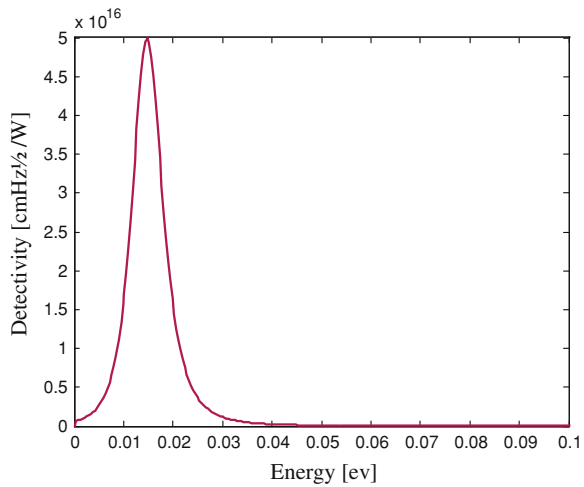


Fig. 2.48 Detectivity of RT-SCDQD based THZ-IR photodetector versus photon energy [125]



structure considerably has large detectivity, low NE ΔT and narrow spectra compared the other case. The small line width of escaping probability which is consequence of the resonant tunneling double barrier as it is obvious in Fig. 2.45 yield to narrow line width in RT-SCDQD IR-photodetector detectivity spectra.

The reported ultra high value of detectivity and low value of NE ΔT are related to two basic effects. One is responsivity which in the proposed structure is increased due to enhancement of the absorption coefficient in SCDQD compared other quantum dots without defect. Second effect related to decrease of the dark current in the proposed structure. Decreasing of dark current in the proposed structure is done owing to the following reasons.

1. Increasing of the barrier height, concluding to decrease of the thermionic term in the dark current. This subject may be introduce some difficulty in electron

Table 2.5 Calculated detectivity, noise-equivalent temperature difference and full-width at half of the maximum of proposed RT-SCQD_THZ IR-photodetector and conventional QD_THZ IR-photodetector at 83 and 300 K [125]

Structure parameter	D^* [cm Hz ^{1/2} /W] 83 K 83 μ m	D^* [cm Hz ^{1/2} /W] 300 K 83 μ m	NE \cdot T	FWHM (μ m)
Conventional QD structure (QD-THZ-RPD)	2.03×10^{10}	5.92×10^7	5.55×10^{-2}	46
Structure (RT-SCDQD-HZ- IRPD)	5×10^{16}	2.29×10^9	1.02×10^{-7}	106

Table 2.6 Design parameters for simulation of proposed RT-SCQD_THZ IR-photodetector and conventional QD_THZ IR-photodetector [125]

Structure parameter	Unit	Proposed QD structure (RT-SCDQD-THZ-IRPD)	Conventional QD structure (QD-THZ-IRPD)
A	M	55×10^{-10}	–
B	M	70×10^{-10}	95×10^{-10}
C	M	90×10^{-10}	–
D	M	110×10^{-10}	–
E	M	130×10^{-10}	–
Defect mole fraction (x_d)	–	0.1	–
Barrier mole fraction (x_b)	–	0.3	0.1
Operation temperature	K	83	83
Spacer layer width	M	130×10^{-10}	40×10^{-10}
Applied voltage	V	2	10

collection in photodetector, which is removed using double barrier element that resonances with first excited state of dot.

2. Using double barrier element in the proposed system, introduces ultra low ground state dark current also.

Finally the proposed photodetector is examined at room temperature. It is observed that the calculated result shows interesting value which illustrates capability for working at room temperature (Table 2.5). This is so interesting and well large value compared previous reported results. The proposed structure illustrates ultra high value compared traditional bound to continuum transition based THZ photodetectors [124]. It can be understood that in this structure we decreased considerably the dark current owing to tuning of intersubband transition to mid conduction band offset to decrease thermal effect (variation of Fermi level and thermionic emission from level to continuum band) and finally extraction and collection of electrons through resonant tunneling double barrier structure. Also, it should be mentioned that the proposed defect in quantum dot increased considerably responsivity of the structure.

Parameters of the proposed structure and conventional structure are given in Table 2.6 for comparison.

In this section the proposed structure for basic block of IR photodetectors were evaluated completely and different features investigated. It was shown that the proposed unit cell have excellent advantages for room temperature photodetectors.

2.5.4 Terahertz Photodetector Based on Intersublevel Optical Absorption in Coupled Quantum Dots

In a quantum dot infrared photodetector (QDIP) [77], electronic transitions between energy states can lead to terahertz radiation detection [99]. When the layers are closely spaced in the coupled quantum dot devices, the level splitting takes place due to vertical electronic correlation. This feature plays an important role in determining the electronic and optical properties of multiple self-assembled quantum dots. The multi-confined levels can be explained by the appearance of level splitting due to vertical electronic correlation. There are four important factors that contribute to level splitting: quantum–mechanical coupling (happen when the QDs are stacked closely together), strain (system does not contain a symmetry plane parallel to the base of the QDs and strain does not affect the two QDs in the same way), piezoelectric potentials (origins from the nonzero off-diagonal shear-strain tensor elements) and finally indium migration during the epitaxial growth.

In the field of infrared photodetector, the absorptions in strongly vertically coupled QDs are based on the inter-subband transitions due to the energy level splitting in the same QDs, have many advantages as following. Firstly, two-color inter-subband absorptions based on the energy level splitting can be easily controlled by adjusting the thickness of spacer. Two-color inter-subband absorptions based on the different size of QDs are limited by the random distribution of QDs and it is difficult to control the absorption peaks. Large-size QDs consequently lead to little full factor and low quantum efficiency. Secondly, the structure of vertically coupled QDs has much stronger normal incidence absorption [133] than that of uncoupled QDs. Thirdly, most devices suffer from low gain or responsivity resulting from the presence of only one quantum dot plane or different size of QDs but these problems could be ameliorated with improving shape and size uniformity of quantum dots and also by adding more quantum-dot planes, so we can use quantum dots planes with coupling in vertical direction. Finally, the coupled quantum dots are too much attractive as the base of the detector structures for detecting the terahertz electromagnetic spectrum [134]. The associated infrared absorption would correspond in this case to an intersublevel transition between the splitting energy levels of vertically coupled dots.

Figure 2.49 shows the schematic view of two typical QDs-stacks that each of them consists of two InAs quantum dots (pyramid or dome shaped) with 0.3-nm-thick wetting layer.

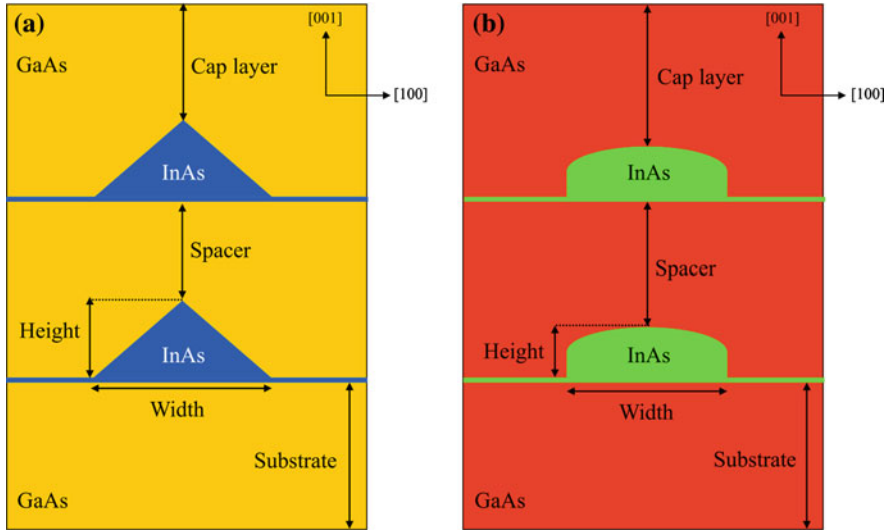
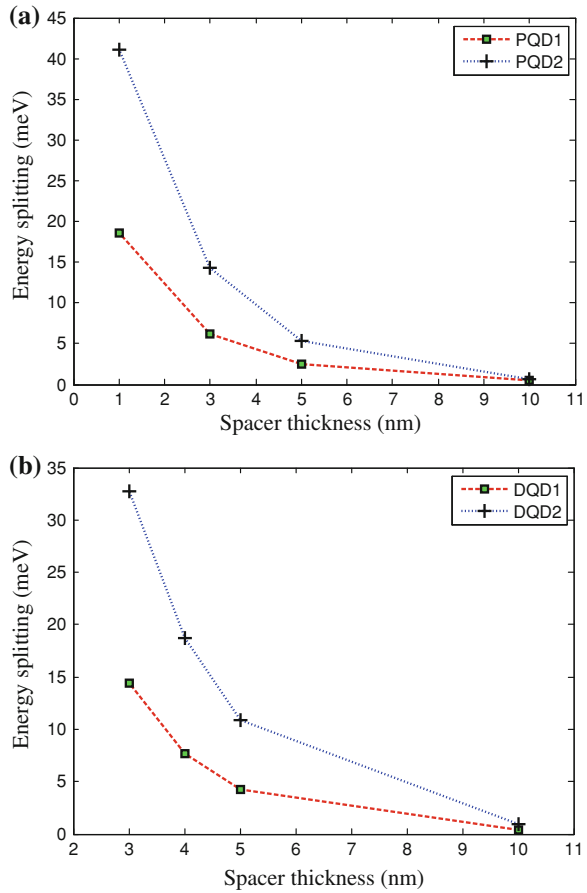


Fig. 2.49 Cross section of the two coupled quantum dot structures with pyramid and dome shaped QDs

In order to theoretically understand the nature of the electronic and optical properties of coupled quantum dots, a first step is to determine the strain distribution in the dot structures and in the matrix material, as the next step, the calculated strain serves as an input to electronic structure calculations. The driving force for vertically self-organized growth is known to be the interacting strain fields induced by the islands. The strain modifies the effective confinement volume in the device, distorts the atom bonds in length and angles, and hence modulates the local band structure and the confined states. The hydrostatic component of strain, for example, usually shifts the conduction and valence band-edges of semiconductors; biaxial strain, on the other hand, modifies the valence bands by splitting the degeneracy of the light- and heavy-hole bands; therefore the strain distribution profoundly affects the electronic and optical properties of the assembly of dots by modifying the energies and wave functions of the electron and hole confined states.

Simulation results show that the top dots increase the strain of the lower dots. This strain increasing is more in dome shaped quantum dots. Because of the special geometry type of dome shaped QD, the upper dot completely cover the lower dot that leads to increasing the coupling effect between quantum dots. Calculated results indicate that the magnitudes of the strain components depend on the geometries and the spacer thicknesses between coupled quantum dots. Because of the presence of strain, the lattice constant is changed and the symmetry of the crystal is reduced, so the bandstructure of semiconductors is generally altered. By taking into account the influence of the strain distributions

Fig. 2.50 Energy level splitting for **a** pyramid shaped QDs (PQD1: base; 15 nm \times height; 7 nm, PQD2: base; 12 nm \times height; 5 nm). Energy level splitting for **b** dome shaped QDs (DQD1: base; 16 nm \times height; 5 nm, DQD2: base; 13 nm \times height; 3 nm) based structures as a function of spacer thickness



and solving the three-dimensional, effective mass single band Schrödinger equation, the energy levels and wavefunctions in coupled quantum dots may be calculated. Here, only the effects of the quantum–mechanical coupling and strain in energy level splitting have been considered and main focus is about electron ground state splitting. Figure 2.50 shows the level splitting for two different QDs-structures with pyramid or dome shaped QDs as a function of spacer thickness.

It is clear that as the dot separation is narrowed, the dots interact strongly with each other mechanically through the strain field as well as quantum mechanically through wavefunctions overlaps, so the energy level splitting increases. For smaller quantum dots, the coupling effects is more, therefore the levels splitting increase for coupled quantum dots with smaller sizes. The geometry type of quantum dots has straight influence in the rate of energy level splitting. Thanks to high amount of strain field in dome shaped quantum dots, separation

increasing between splitted energy levels expected in compared with pyramidal shape dot.

The typical calculated ground state splitting is about $0 \rightarrow 41$ meV ($0 \rightarrow 10$ THz) and therefore the strongly vertically coupled QDs are promising for fulfill the terahertz range detection due to their energy level splitting. In coupled quantum dots based photodetectors, the sizes of quantum dots, distance between coupled QDs, the geometry types of dots and finally the material composition help designer to detect the special wavelength in terahertz spectrum region.

2.6 Terahertz and Infrared Photodetector Based on Electromagnetically Induced Transparency

The noise source and the dark current inhibit the correct detection of the low-level terahertz signals. A great deal of research has gone into the elimination of the noise source in photodetectors [27, 135]. Until now in practical implementations efforts are usually limited to cooling of the designed devices, which is hard from a practical point of view. The environment temperature controlling is critical and a hard problem especially in room temperature due to high-level dark current. The target radiation detection is limited by the thermionic emission dark current. The photon energy in the terahertz level detection may be in the order of the thermal broadening of electron distribution ($KT \sim 6$ meV at 77 K and 25 meV at 300 K) [1, 86].

However in the electromagnetically induced transparency (EIT) based photodetection [136–138], the electrons are not directly excited by terahertz radiation. On the other hand the absorption characteristic of a short-wavelength probe optical field is affected by terahertz radiation. In this system, the important thermionic dark current can be nearly cancelled out. In this part, the terahertz detection based on EIT process is studied in a multi-level atomic systems which finally realized by quantum well structures. The mathematical background for these structures is developed and then it is shown that the probe field absorption can be controlled by the electromagnetic control and terahertz radiations.

2.6.1 Electromagnetically Induced Transparency Phenomena

During the past two decades, quantum coherence (atomic phase coherence) effects have exhibited many physically interesting phenomena such as electromagnetically induced transparency (EIT) [139]. The control of linear and non-linear optical properties of a material system using resonant electromagnetic

fields has become more and more important in recent years. EIT has proved to be a powerful technique that can be used to eliminate the effect of a medium on a propagating beam of electromagnetic radiation, while retaining the large and desirable nonlinear optical properties associated with the resonant response of a medium [139–141]. Recent remarkable applications include ultraslow light pulse propagation and light storage in atomic vapour systems. The occurrence of EIT in other configurations has also been predicted theoretically. Most of this work has been investigated in the atomic vapour systems, although an extension of these ideas to solid-state systems would be more promising. In the next part the electromagnetically induced transparency are discussed theoretically.

2.6.1.1 Atom–Field Interaction Hamiltonian

An electron with charge e and mass m interacting with an external electromagnetic field is described by a minimal-coupling Hamiltonian as [140]:

$$H = \frac{1}{2}[P - eA(r, t)]^2 + eU(r, t) + V(r) \quad (2.81)$$

where P is the canonical momentum operator, $A(r, t)$ and $U(r, t)$ are the vector and scalar potentials of the external field, respectively and $V(r)$ is an electrostatic potential that is normally the atomic binding potential. In this section, we first derive this Hamiltonian from a gauge invariance point of view, before reducing it to a simple form suitable for describing the interaction of a two-level atom with the radiation field. We examine the problem of an electron bound by a potential $V(r)$ to a force center (nucleus) located at r_0 . The minimal-coupling Hamiltonian for an interaction between an atom and the radiation field can be reduced to a simple form by using the dipole approximation. The entire atom is immersed in a plane electromagnetic wave described by a vector potential $A(r_0 + r, t)$:

$$\begin{aligned} A(r_0 + r, t) &= A(t) \exp(i\mathbf{K} \cdot (r_0 + r)) \\ &= A(t) \exp(i\mathbf{K} \cdot r_0)(1 + i\mathbf{K} \cdot r + \dots) \end{aligned} \quad (2.82)$$

This vector potential may be written in the dipole approximation, $\kappa \cdot r \ll 1$, as:

$$A(r_0 + r, t) \cong A(t) \exp(i\mathbf{K} \cdot r_0) \quad (2.83)$$

The Schrodinger equation for this problem (in the dipole approximation) is given by:

$$\left\{ \frac{\hbar^2}{2m} \left[\nabla - \frac{ie}{\hbar} A(r_0, t) \right]^2 + V(r) \right\} \psi(r, t) = i\hbar \frac{\partial}{\partial t} \Psi(r, t) \quad (2.84)$$

where we are working in the radiation gauge, in which:

$$\begin{aligned} U(r, t) &= 0 \\ \nabla \cdot A &= 0 \end{aligned} \quad (2.85)$$

We have added the term $V(r)$ in the Hamiltonian which arises from the electrostatic potential that binds the electron to the nucleus. For simplicity in Eq. 2.84 we define a new wave function as:

$$\Psi(r, t) = \exp \left[\frac{ie}{\hbar} A(r_0, t) \right] \Phi(r, t) \quad (2.86)$$

By inserting Eq. 2.85 into Eq. 2.84 we have:

$$i\hbar \Phi(r, t) = H\Phi(r, t) \quad (2.87)$$

where

$$H = H_0 + H_1 \quad (2.88)$$

$$H_0 = \frac{p^2}{2m} + V(r) \quad (2.89)$$

$$H_1 = -er \cdot E(r_0 \cdot t) \quad (2.90)$$

In the above equations H_0 is the unpertubated Hamiltonian and H_1 is the pertubated Hamiltonian, respectively.

2.6.1.2 Equation of Motion for the Density Matrix

In many situations we may not know $|\phi\rangle$ only know the probability P_ϕ that the system is in the state $|\phi\rangle$. For such a situation, we define the density operator ρ as [140]:

$$\rho = \sum P_\Psi |\Psi\rangle \langle \Psi| \quad (2.91)$$

We obtain the equation of motion for the density matrix from the Schrodinger equation as:

$$|\dot{\phi}\rangle = -\frac{i}{\hbar} H|\phi\rangle \quad (2.92)$$

With taking the time derivative of ρ we have:

$$\dot{\rho} = \sum_{\phi} P_{\phi} (|\dot{\phi}\rangle \langle \phi| + |\phi\rangle \langle \dot{\phi}|) \quad (2.93)$$

where P_{ϕ} , is time independent. By using Eqs. 2.92 and 2.93 we have:

$$\dot{\rho} = -\frac{i}{\hbar}[H, \rho] \quad (2.94)$$

In the above equation we have not included the decay rates of the atomic levels due to spontaneous emission. The decay rates can be incorporated in the above equation by a relaxation matrix Γ , which is denoted by the equation:

$$\langle n|\Gamma|m\rangle = \gamma_n \delta_{nm} \quad (2.95)$$

With this addition, the density matrix equation of motion becomes:

$$\dot{\rho} = -\frac{i}{\hbar}[H, \rho] - \frac{1}{2}\{\Gamma, \rho\} \quad (2.96)$$

where $\{\Gamma, \rho\} = \Gamma\rho + \rho\Gamma$. In general, the equation of motion becomes as:

$$\dot{\rho}_{ij} = -\frac{i}{\hbar} \sum_k (H_{ik}\rho_{kj} - \rho_{ik}H_{kj}) - \frac{1}{2} \sum_k (\Gamma_{ik}\rho_{kj} + \rho_{ik}\Gamma_{kj}) \quad (2.97)$$

2.6.1.3 Coherent Trapping: Dark States

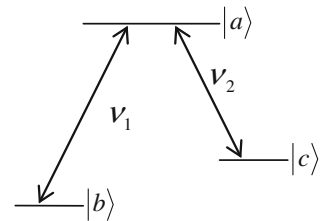
It is possible to cancel absorption or emission under certain conditions. This interesting phenomenon in which a coherent superposition of atomic states is responsible for a novel effect is coherent trapping. If an atom is prepared in a coherent superposition of states, it is possible to cancel absorption or emission under certain conditions. So these atoms are then effectively transparent to the incident field even, the presence of resonant transitions. We discuss the effect of coherent trapping and dark state in three-level atomic systems. Figure 2.51 shows the three level atomic systems where the dark states are shown.

The Hamiltonian for the system, in the rotating-wave approximation, is obtained by:

$$H_0 + H_1 \quad (2.98)$$

$$H_0 = \hbar\omega_a|a\rangle\langle a| + \hbar\omega_b|b\rangle\langle b| + \hbar\omega_c|c\rangle\langle c| \quad (2.99)$$

Fig. 2.51 Interaction of three level atomic systems with two single mode fields



$$H_1 = -\frac{\hbar}{2}(\Omega_{R1}e^{-i\varphi_1}e^{-i\nu_1 t}|a\rangle\langle b| + \Omega_{R2}e^{-i\varphi_2}e^{-i\nu_2 t}|a\rangle\langle c|) + \text{H.c.} \quad (2.100)$$

where $\Omega_{R1}e^{-i\varphi_1}$ and $\Omega_{R2}e^{-i\varphi_2}$ are the complex Rabi frequencies associated with the coupling of the field modes of frequencies ν_1, ν_2 to the atomic transitions $|a\rangle \rightarrow |b\rangle$ and $|a\rangle \rightarrow |c\rangle$. The atomic wave function can be written as:

$$|\Psi\rangle = C_a(t)e^{-i\omega_a t}|a\rangle + C_b(t)e^{-i\omega_b t}|b\rangle + C_c(t)e^{-i\omega_c t}|c\rangle \quad (2.101)$$

The probability amplitudes $C_a(t)$, $C_b(t)$, and $C_c(t)$ can be derived from the Schrödinger equation $i\hbar|\dot{\Psi}\rangle = H|\Psi\rangle$ as:

$$\dot{C}_a = \frac{i}{2}(\Omega_{R1}e^{-i\Phi_1}C_b + \Omega_{R2}e^{-i\Phi_1}C_c) \quad (2.102)$$

$$\dot{C}_b = \frac{i}{2}(\Omega_{R1}e^{-i\Phi_1}C_a) \quad (2.103)$$

$$\dot{C}_c = \frac{i}{2}(\Omega_{R2}e^{-i\Phi_2}C_a) \quad (2.104)$$

By the analytical solution we can find the probability amplitudes as:

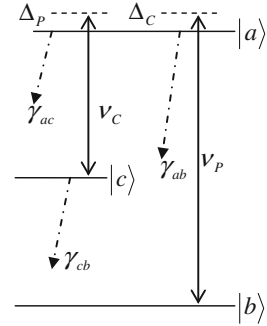
$$\begin{aligned} C_a(t) &= 0 \\ C_b(t) &= \frac{1}{\sqrt{2}} \\ C_c(t) &= \frac{1}{\sqrt{2}}e^{-i\varphi} \end{aligned} \quad (2.105)$$

It is clear that the population is trapped in the lower states and there is no absorption even in the presence of the electromagnetic field. This means that the absorption can be changed by this method. In the present three-level atom, coherent trapping occurs due to the destructive quantum interference between the two transitions. Finally the wave function for this system is obtained as:

$$|\Psi(t)\rangle = \frac{\Omega_{R2}(t)e^{-i\varphi_2}|b\rangle - \Omega_{R1}(t)e^{-i\varphi_1}|c\rangle}{\sqrt{\Omega_{R1}^2 + \Omega_{R2}^2}} \quad (2.106)$$

We discussed the phenomena of coherent population trapping in three-level atom system in which the lower levels are prepared in a coherent superposition state. The other related phenomenon is the EIT. When a pair of near-resonant laser fields interact with the three levels (lambda type), in the condition of two-photon resonance, the populations are coherently trapped in the two lower levels. At this two-photon resonance point, the atom is in a dark state and decoupled with the

Fig. 2.52 The EIT phenomena in three-level atomic systems



applied fields, so the fields transmit the medium without absorption and the EIT occurs. Figure 2.52 shows the three-level atomic system which EIT phenomena are happens.

Due to no absorption at the transparency point, EIT is applied to various low light nonlinear optical processes. The linear and nonlinear susceptibilities have been resonantly enhanced because of the coherent control of quantum states. Based on EIT, various kinds of four-wave and six-wave mixing with high quantum efficiency are investigated.

The dipole moment in quantum mechanics is defined by $P = e\langle\Psi(t)|r|\Psi(t)\rangle$. In this case we obtain dipole moment as [1, 27]:

$$P = \rho_{ab}\wp_{ba} + \rho_{ac}\wp_{ca} + \rho_{cb}\wp_{cb} + \text{c.c.} \quad (2.107)$$

where $\wp_{ij} = \langle i|r|j\rangle$ is the matrix element. In the selection rules theory the transition $|c\rangle \rightarrow |b\rangle$ is not valid, so $\wp_{bc} = \wp_{cb} = 0$. The probe frequency and the transition $|a\rangle \rightarrow |c\rangle$ frequency are different ($\rho_{ab} \rightarrow 0$) so the dipole moment can be written as:

$$P(v) = \rho_{ab}\wp_{ba} + \text{c.c.} \quad (2.108)$$

On the other hand we can write:

$$P(z, t) = \varepsilon_0 \int_0^\infty d\tau \tilde{x}(\tau) E(z, t - \tau) \quad (2.109)$$

where E is flat wave across the z axis, therefore:

$$E(z, t) = 1/2Ee^{-i(vt-kz)} + \text{c.c.} \quad (2.110)$$

Finally we obtain the dipole moment as:

$$\begin{aligned}
P(z, t) &= \frac{\varepsilon_0 E}{2} \int_0^\infty d\tau \tilde{x}(\tau) \left(e^{-i(v(t-\tau)-kz)} + e^{i(v(t-\tau)-kz)} \right) \\
&= \frac{\varepsilon_0 E}{2} \left(\left(\int_0^\infty \tilde{x}(\tau) e^{iv\tau} d\tau \right) e^{-i(vt-kz)} + \left(\int_0^\infty \tilde{x}(\tau) \cdot e^{-iv\tau} d\tau \right) e^{i(vt-kz)} \right) \\
&= \frac{\varepsilon_0 E}{2} \left(\chi(-v) e^{-i(vt-kz)} + \chi(v) e^{i(vt-kz)} \right) \\
&= \frac{\varepsilon_0 E}{2} \chi(v) e^{-i(vt-kz)} + \text{c.c.}
\end{aligned} \tag{2.111}$$

By using Eqs. 2.107 and 2.110 we obtain:

$$\frac{\varepsilon_0 E}{2} \chi(v) e^{-i(vt-kz)} + \text{c.c.} = \rho_{ab} \wp_{ba} + \text{c.c.} \tag{2.112}$$

In a system with atom density N_a we write:

$$\frac{\varepsilon_0 E}{2} \chi(v) e^{ivt} = (\rho_{ab} \wp_{ba})^* N_a \tag{2.113}$$

And finally the susceptibility is equal:

$$\chi(v) = \frac{2}{\varepsilon_0 E} N_a (\rho_{ab} \wp_{ba})^* e^{-ivt} \tag{2.114}$$

For solving above equation we should find the ρ_{ab} from density matrix, so in the three-level atomic system the total Hamiltonian and density matrix can obtain as [136, 140]:

$$H = \hbar \begin{bmatrix} v_b & 0 & -\frac{1}{2} \Omega_p e^{-iv_p t} \\ 0 & v_c & -\frac{i}{2} \Omega_c e^{-iv_p t} \\ -\frac{1}{2} \Omega_p e^{-iv_p t} & -\frac{1}{2} \Omega_c e^{-iv_p t} & v_a \end{bmatrix} \tag{2.115}$$

$$\dot{\rho}_{ab} = -(iv_{ab} + \gamma_{ab}) \rho_{ab} - \frac{i}{2} \Omega_p e^{-iv_p t} (\rho_{aa} - \rho_{bb}) + \frac{i}{2} \Omega_c e^{-iv_c t} \rho_{cb} \tag{2.116}$$

$$\dot{\rho}_{cb} = -(iv_{cb} + \gamma_{cb}) \rho_{cb} - \frac{i}{2} \Omega_p e^{-iv_p t} \rho_{ca} + \frac{i}{2} \Omega_c e^{iv_c t} \rho_{ab} \tag{2.117}$$

$$\dot{\rho}_{ac} = -(iv_{ac} + \gamma_{ac}) \rho_{ac} - i \Omega_c e^{-iv_c t} (\rho_{aa} - \rho_{cc}) + \frac{i}{2} \Omega_p e^{-iv_p t} \rho_{bc} \tag{2.118}$$

With the using Eq. 2.113 we obtain optical susceptibility as:

$$\chi^{(1)}(\nu) = \frac{iN_a \epsilon_0^2 (i[\Delta_p - \Delta_c] + \gamma_{cb})}{\epsilon_0 \hbar [(i\Delta_p + \gamma_{ab})(i[\Delta_p - \Delta_c] + \gamma_{cb}) + \Omega_c^2/4]} \quad (2.119)$$

The linear response of atom for resonant light determined by the first order of susceptibility as [140]:

$$\chi^{(1)} = \chi' + i\chi'' \quad (2.120)$$

The real and imaginary parts of the susceptibility are proportional to absorption coefficient and refractive coefficient, respectively, so we can write:

$$\alpha = \omega_p n_0 \chi'' / c \quad (2.121)$$

$$\beta = \omega_p n_0 \chi' / 2c \quad (2.122)$$

Imaginary and real parts of susceptibility for interaction of three level atomic system with two single mode fields are shown in Fig. 2.53. In the case when to field are resonant because of the dark state and coherent trapping and related EIT phenomena the absorption and refractive characteristic are modified. It is illustrated that we can change the absorption and transmission coefficient of electromagnetic field by another electromagnetic field names control field.

2.6.2 EIT-Based Photodetection

The terahertz photodetection system based on EIT phenomena is schematically shown in Fig. 2.54. This system involves a 4-level atomic system interacting with three fields of control, probe and terahertz electromagnetic signals [136, 138].

The total Hamiltonian in the rotating-wave approximation (keeping only energy conserving terms in Hamiltonian) and in the ignored counter rotating terms case [140], is given as follows:

$$H = H_0 + H_1 \quad (2.123)$$

where

$$H_0 = \hbar\omega_1|1\rangle\langle 1| + \hbar\omega_2|2\rangle\langle 2| + \hbar\omega_3|3\rangle\langle 3| + \hbar\omega_4|4\rangle\langle 4| \quad (2.124)$$

$$H_1 = \hbar\Omega_p|1\rangle\langle 4| + \hbar\Omega_c|2\rangle\langle 4| + \hbar\Omega_{IR1}|2\rangle\langle 3| \quad (2.125)$$

Here Ω_p , Ω_c and Ω_{IR1} are the Rabi frequencies associated with the coupling of the field modes of, probe, control and terahertz signals to the atomic transition states 2–4, 4–1 and 3–2, respectively. If some mathematical rearranging and

Fig. 2.53 **a** Imaginary and **b** real parts of susceptibility for interaction of three level atomic system with two single mode fields

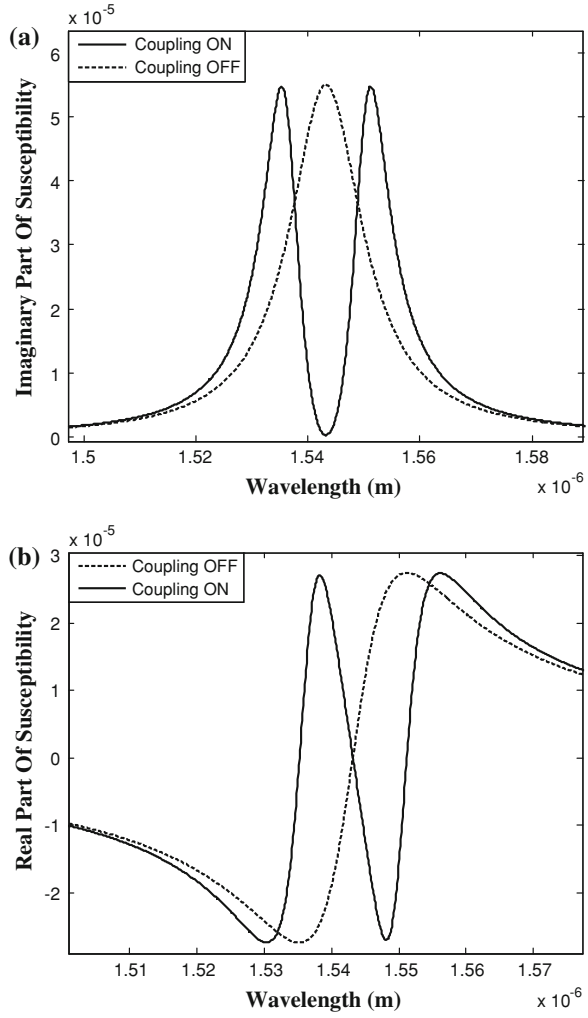
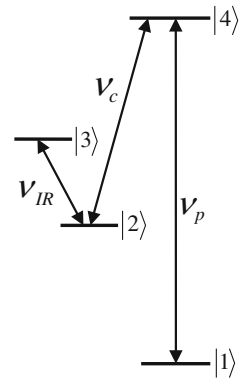


Fig. 2.54 Schematic of terahertz photodetection system based on EIT [136, 138]



manipulation is done, we can obtain the following analytical density matrix time development equations which handle this 4-level atomic system [136, 138, 140]:

$$\dot{\rho}_{41} = -[i\Delta_p + \gamma_{41}]\rho_{41} + i\Omega_p\rho_{11} + i\Omega_c\rho_{21} - i\Omega_p\rho_{44} \quad (2.126)$$

$$\dot{\rho}_{21} = -[i(\Delta_p - \Delta_c) + \gamma_{21}]\rho_{21} + i\Omega_{IR}\rho_{31} + i\Omega_c\rho_{41} - i\Omega_p\rho_{24} \quad (2.127)$$

$$\dot{\rho}_{31} = -[i(\Delta_p + \Delta_{IR} - \Delta_c) + \gamma_{31}]\rho_{31} + i\Omega_{IR}\rho_{21} - i\Omega_p\rho_{34} \quad (2.128)$$

where $\Delta_p = \nu_{41} - \nu_p$, $\Delta_c = \nu_{42} - \nu_c$ and $\Delta_{IR} = \nu_{32} - \nu_{IR}$ are detuning corresponding to probe, control and terahertz signals, respectively. The differential matrix equation can be solved as follow:

$$\dot{R} = -MR + A \quad (2.129)$$

where $A = \begin{bmatrix} i\alpha \\ 0 \\ 0 \end{bmatrix}$ and

$$M = \begin{bmatrix} (i\Delta_p + \gamma_{41}) & -i\Omega_c & 0 \\ -i\Omega_c & [i(\Delta_p - \Delta_c) + \gamma_{21}] & -i\Omega_{IR} \\ 0 & -i\Omega_{IR} & [i(\Delta_p + \Delta_{IR} - \Delta_c) + \gamma_{31}] \end{bmatrix}.$$

Also, γ_{41} , γ_{21} , γ_{31} , Ω_c and Ω_{IR} are decay rate of density matrix equations, Rabi frequency of infrared and control field, respectively, and $R = \begin{bmatrix} \rho_{41} \\ \rho_{21} \\ \rho_{31} \end{bmatrix}$. The exact analytical solution is:

$$R(t) = M^{-1}A \quad (2.130)$$

The optical susceptibility of probe field is obtained by:

$$\chi_{41} = \frac{2N_a\epsilon_0^2/\epsilon_0\hbar \left[\gamma_{21} + i(\Delta_p - \Delta_c) + \frac{\Omega_{IR}^2}{\alpha} \right]}{\left[\Omega_c^2 + [i\Delta_p + \gamma_{41}][i(\Delta_p - \Delta_c) + \gamma_{21}] + \frac{\Omega_{IR}^2(i\Delta_p + \gamma_{41})}{\alpha} \right]} \quad (2.131)$$

where Ω_p and N_a are the Rabi frequency of the probe field and the atomic density, respectively. One should note that the transmission coefficient is proportional to the imaginary part of the calculated susceptibility. In our calculation, the environment temperature effect on the system operation is added by $E_T = \frac{3}{2}KT$ where E_T , K and T are the thermal energy, the Boltzmann constant and temperature in Kelvin, respectively. This energy should be added to the signal energy. On the other hand, the exact behavior of 4-level atomic system can be determined by calculating zeros and poles of matrix M or calculating zeros and poles of ρ_{41} . In the case of without detuning, that is all fields are coupled, we have:

$$\text{poles}(\rho_{41}) = \begin{cases} v_{41} + \sqrt{\Omega_c^2 + \Omega_{\text{IR}}^2} \\ v_{41} - \sqrt{\Omega_c^2 + \Omega_{\text{IR}}^2} \end{cases} \quad \text{and} \quad \text{zeros}(\rho_{41}) = \begin{cases} v_{41} + \Omega_{\text{IR}} \\ v_{41} - \Omega_{\text{IR}} \end{cases} \quad (2.132)$$

$$\text{If } \Omega_{\text{IR}=0} \Rightarrow \text{poles}(\rho_{41}) = \begin{cases} v_{41} + \Omega_c^2 \\ v_{41} - \Omega_c^2 \end{cases} \quad \text{and} \quad \text{zeros}(\rho_{41}) = \begin{cases} v_{41} \\ v_{41} \end{cases} \quad (2.133)$$

However in the presence of detuning, the locations of zeros and poles change and the response of the system is completely different. The important case is, when $\Delta_{\text{IR}} = \Delta_c$ we have the following result:

$$\text{poles}(\rho_{41}) = \begin{cases} v_{41} + \sqrt{\Omega_c^2 + \Omega_{\text{IR}}^2} \\ v_{41} - \sqrt{\Omega_c^2 + \Omega_{\text{IR}}^2} \end{cases} \quad \text{and} \quad \text{zeros}(\rho_{41}) = \begin{cases} v_{41} + \Omega_{\text{IR}} \\ v_{41} - \Omega_{\text{IR}} \end{cases} \quad (2.134)$$

In this section, simulated results including the optical susceptibilities and transmission coefficient in the different proposed atomic systems are presented and discussed. First, we illustrate the effects of infrared and control fields on the real and imaginary parts of the optical susceptibility for 4-level structure (Fig. 2.54) in Fig. 2.55a, b. In Fig. 2.55a, b, it is shown that for a given control field, when the magnitude of infrared field increases the spectrum of the imaginary and real parts of the optical susceptibility are displaced and changed. In the presence of control field, an Autler–Townes doublet is created and when the infrared field is applied, Autler–Townes doublet broadens and another peak appears in the central part of the spectrum of doublet, so three peaks are appeared in the susceptibility spectra. This broadness and central peak increase with increasing of the infrared field intensity. This behavior was expected from the calculation of poles and zeros (Eq. 2.132). As we know, this central peak disappears, when the infrared field is switched off.

It is clear that, the transmission and reflection coefficients are proportional to imaginary and real parts of the susceptibility, respectively. The effect of infrared and control fields on the transmission coefficient of the probe field for 4-level system is shown in Fig. 2.56. It is observed that the Autler–Townes doublet is created with the definite control field and is broadened with increasing of the control field. In the presence of IR field, central absorption peak appears. Thus, measuring of the optical wavelength absorption illustrates the infrared signal level.

Figure 2.57 shows the effect of different IR intensity on the transmission coefficient spectrum. It is observed that with increasing IR intensity the transmission coefficient at central peak also decreases. When IR intensity becomes comparable with control field the width of Autler–Townes doublet increases and is considerable. This behavior was expected from the calculated poles and zeros (Eq. 2.132). It is clear that with changing the IR field intensity, position of the poles and zeros are changed and so the splitting of doublet changes also.

Fig. 2.55 **a** Real and **b** imaginary parts of susceptibility versus wavelength for different Infrared Rabi frequencies ($\Omega_c = 5 \times 10^{12} \text{s}^{-1}$, $\Omega_p = 10^8 \text{s}^{-1}$, $\Delta_{\text{IR}} = \Delta_c = 0$, $N_a = 10^{20} \text{cm}^{-3}$, $\gamma_{41} = 10^{12} \text{s}^{-1}$, $\gamma_{31} = \gamma_{21} = 5 \times 10^9 \text{s}^{-1}$, $\varphi = 10^{-10} \text{e} - \text{cm}$)

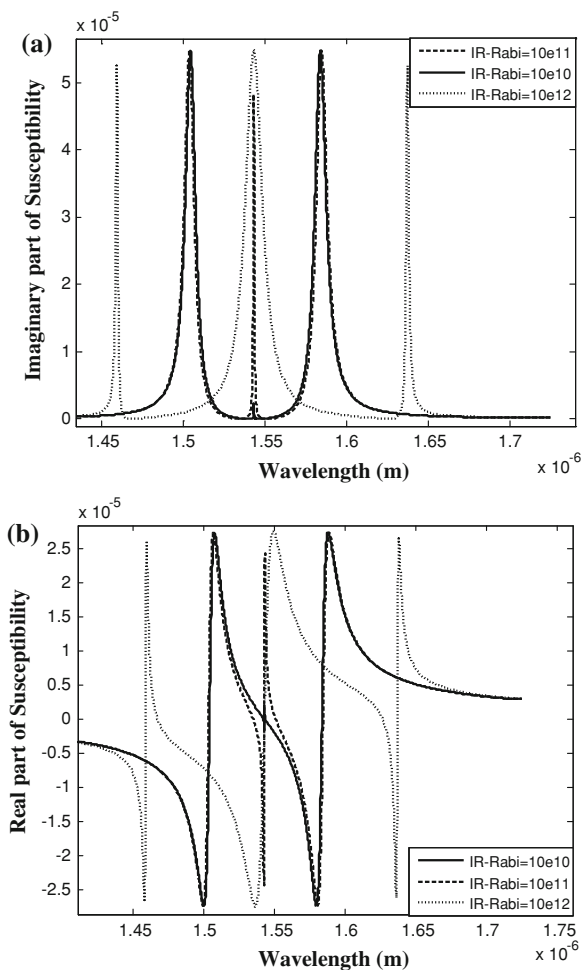


Fig. 2.56 Transmission coefficient versus wavelength with and without IR field [136] ($\Omega_c = 5 \times 10^{12} \text{s}^{-1}$, $\Omega_p = 10^8 \text{s}^{-1}$, $\Delta_{\text{IR}} = \Delta_c = 0$, $N_a = 10^{20} \text{cm}^{-3}$, $\gamma_{41} = 10^{12} \text{s}^{-1}$, $\gamma_{31} = \gamma_{21} = 5 \times 10^9 \text{s}^{-1}$, $\varphi = 10^{-10} \text{e} - \text{cm}$)

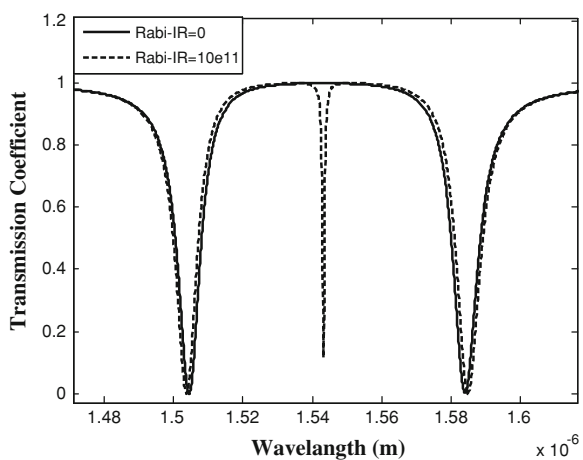


Fig. 2.57 Transmission coefficient versus wavelength with different infrared Rabi frequencies [136] ($\Omega_c = 5 \times 10^{12} \text{s}^{-1}$, $\Omega_p = 10^8 \text{s}^{-1}$, $\Delta_{\text{IR}} = \Delta_c = 0$, $N_a = 10^{20} \text{cm}^{-3}$, $\gamma_{41} = 10^{12} \text{s}^{-1}$, $\gamma_{31} = \gamma_{21} = 5 \times 10^9 \text{s}^{-1}$, $\varphi = 10^{-10} \text{e} - \text{cm}$)

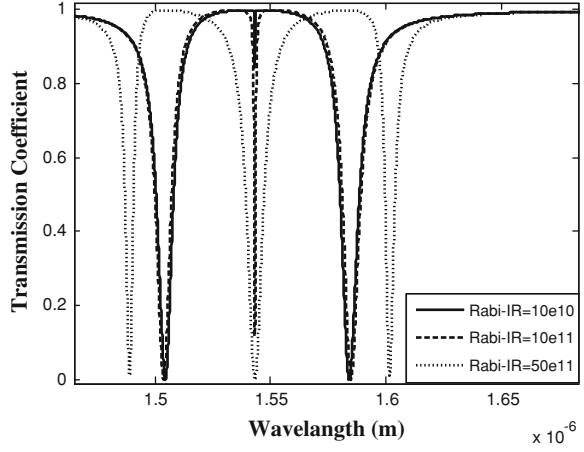
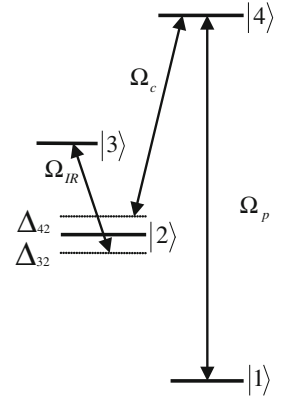


Fig. 2.58 Schematic of 4-levels atomic system with detuned fields [136, 138]



In previous simulations, we assumed that all fields are on resonance and there is not any detuning. However if we consider nonzero detuning for applied electric fields (Fig. 2.54), so, we have the following scheme illustrated in Fig. 2.58.

In this case the position of poles and zeros are changed and so the imaginary and real parts of the susceptibility as well as the transmission coefficient should be changed. The appeared central absorption peak shifts left or right according to positive or negative detuning (Fig. 2.59). It is interesting when $\Delta_{\text{IR}} = \Delta_c$, the central absorption peak is fixed and does not change (Fig. 2.59). Therefore, with control of the control field detuning effect of IR signal level on optical absorption peak displacement can be ignored.

Figure 2.60 shows two different situations. When all three fields are on resonance ($\Delta_{\text{IR}} = 0$), there is an absorption exactly in central part of the transmission band (dashed line). If the IR field is a long-wavelengths infrared field and the probe field an optical field, so, the absorption characteristic of the short-wavelength probe field on resonance translate the absorption characteristic of IR field. These features make

Fig. 2.59 Transmission coefficient versus wavelength with different detuning [136] ($\Omega_c = 5 \times 10^{12} \text{ s}^{-1}$, $\Omega_p = 10^8 \text{ s}^{-1}$, $\Delta_{\text{IR}} = \Delta_c = 0$, $N_a = 10^{20} \text{ cm}^{-3}$, $\gamma_{41} = 10^{12} \text{ s}^{-1}$, $\gamma_{31} = \gamma_{21} = 5 \times 10^9 \text{ s}^{-1}$, $\wp = 10^{-10} \text{ e} - \text{cm}$)

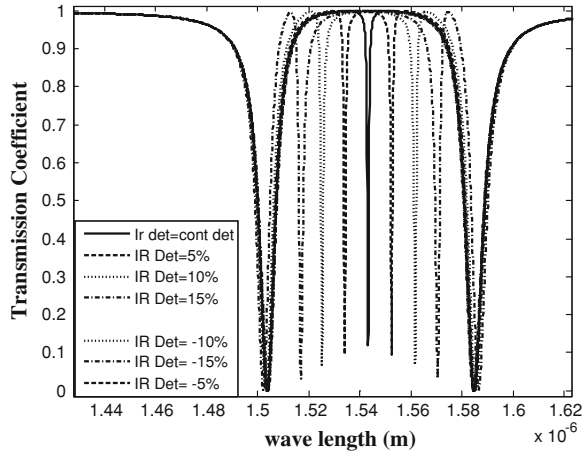
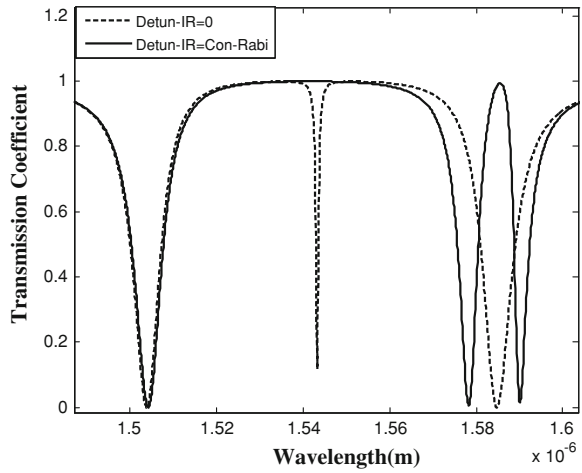


Fig. 2.60 Transmission coefficient versus wavelength without and with Infrared detuning equal with Rabi frequency of control field [136] ($\Omega_c = 5 \times 10^{12} \text{ s}^{-1}$, $\Omega_p = 10^8 \text{ s}^{-1}$, $\Delta_{\text{IR}} = \Delta_c = 0$, $N_a = 10^{20} \text{ cm}^{-3}$, $\gamma_{41} = 10^{12} \text{ s}^{-1}$, $\gamma_{31} = \gamma_{21} = 5 \times 10^9 \text{ s}^{-1}$, $\wp = 10^{-10} \text{ e} - \text{cm}$)



the present system suitable for a kind of detector. If IR field detuning becomes $\Delta_{\text{IR}} \approx \Omega_c$ and other fields are on resonance a new transparency appears near the maximum absorption of the system. Thus it is also possible to turn absorption into transparency.

Figure 2.61 shows the effect of environment temperature on the transparency spectrum of the probe field. The effect of the environment temperature is the same as detuning effect. It is shown that wavelength of the central absorption changes with temperature. It is observed that 7 nm shift of wavelength for 30°C of temperature fluctuation. When refractive index of material increases ($n_{\text{refractive}} = 1 \rightarrow 3.5$ (for GaAs)), the wavelength temperature coefficient decreases ($\Delta\lambda/\Delta T = 0.23 \text{ nm}/^\circ\text{C} \rightarrow 66 \text{ pm}/^\circ\text{C}$) that is so excellent from practical implementation point of view.

Fig. 2.61 Transmission coefficient versus wavelength with different environment temperatures [136] ($\Omega_c = 5 \times 10^{12} \text{ s}^{-1}$, $\Omega_p = 10^8 \text{ s}^{-1}$, $\Delta_{IR} = \Delta_c = 0$, $N_a = 10^{20} \text{ cm}^{-3}$, $\gamma_{41} = 10^{12} \text{ s}^{-1}$, $\gamma_{31} = \gamma_{21} = 5 \times 10^9 \text{ s}^{-1}$, $\wp = 10^{-10} \text{ e} - \text{cm}$)

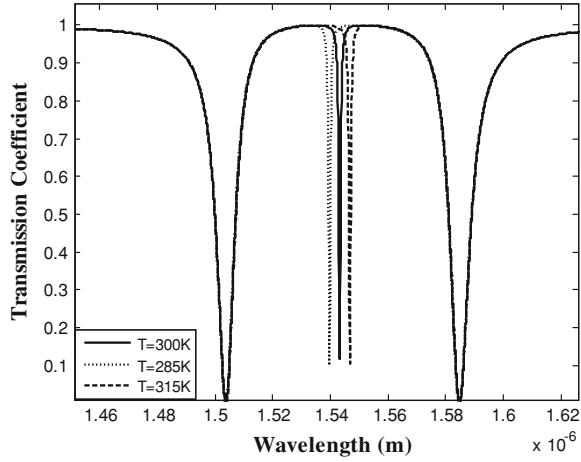
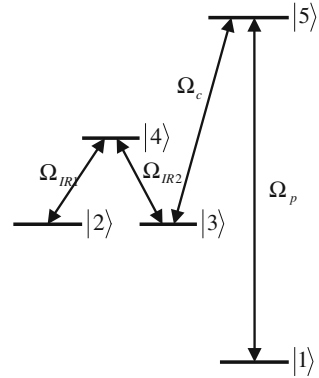
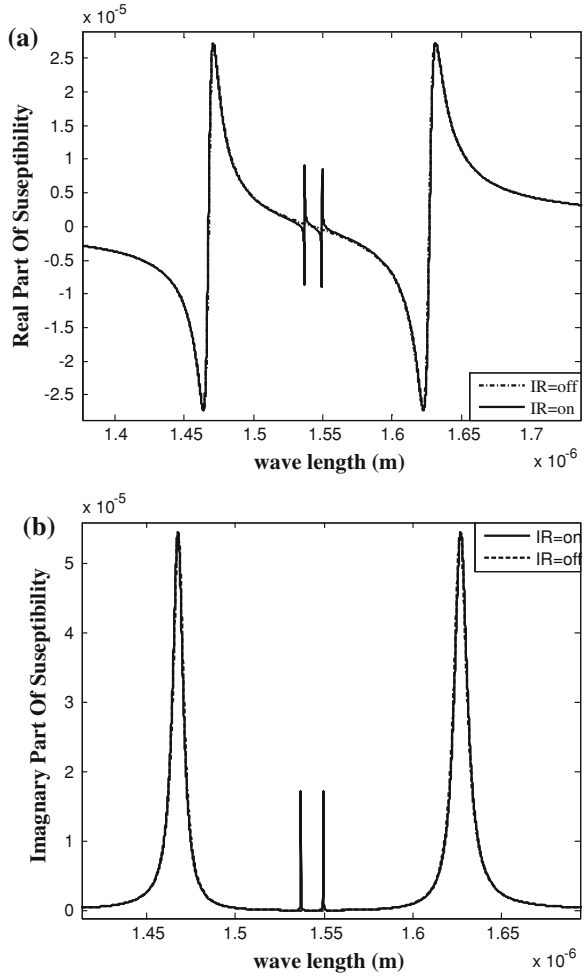


Fig. 2.62 Schematic of 5-levels atomic system [136]



In this part, we investigate interaction of IR, control and probe signals in the case of 5-level atomic system which is proposed in Fig. 2.62. Figure 2.63 shows the effect of infrared radiation on 5-level atomic system. In this system two equal infrared signals are used. In this system control field introduces the Autler-Townes doublet in the real and imaginary parts of the susceptibility as well as the splitting of doublet is proportional to the control Rabi frequency. In the presence of IR field, two new doublets are observed in the band gap. In the next part, we illustrate exact result in some schemes. For managing of thermal problems in detectors, we propose the schematic of 5-level atomic system. In this system the effect of environment temperature is added to the incoming energy of photon and this is like having detuned in the fields. If we consider $\Delta_{IR} = \Delta_c$ in Fig. 2.62, we can cancel out this temperature dependency. In this system, we use two equal states for the incoming IR radiation. This means that the thermal energy that added to the two IR radiations and the detuning of two IR is the same.

Fig. 2.63 **a** Real and **b** imaginary parts of susceptibility versus wavelength with infrared radiation on (solid line) and infrared radiation off (dashed line) [136]
 $\Omega_c = 10^{12} \text{ s}^{-1}$, $\Omega_p = 10^8 \text{ s}^{-1}$,
 $\Omega_{IR} = 5^{11}$, $\Delta_{IR1} = \Delta_{IR2} =$
 $\Delta_c = \Delta_p = 0$, $T = 0 \text{ K}$, $N_a =$
 10^{20} cm^{-3} , $\gamma_{51} = 10^{12} \text{ s}^{-1}$,
 $\gamma_{31} = \gamma_{21} = 5 \times$
 10^9 s^{-1} , $\gamma_{41} = 10^{11}$,
 $\wp = 10^{-10} \text{ e} - \text{cm}$



As disused in the above the optical susceptibility in a five-level atomic system for the probe field can be obtain as:

$$\dot{\rho}_{51} = -[i(\Delta_p) + \gamma_{51}]\rho_{51} + i\Omega_c\rho_{31} + i\Omega_p\rho_{11} - i\Omega_p\rho_{55} \quad (2.135)$$

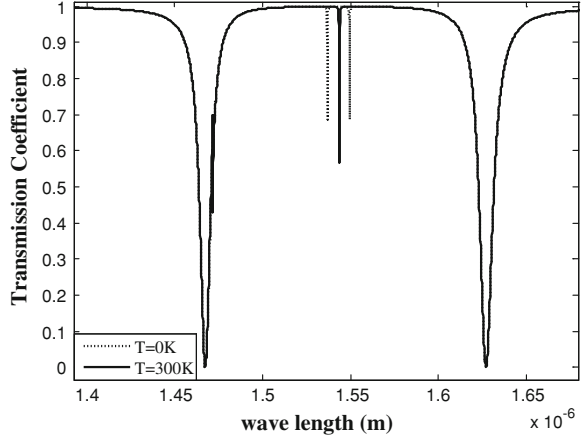
$$\dot{\rho}_{31} = -[i(\Delta_p - \Delta_c) + \gamma_{31}]\rho_{31} + i\Omega_c\rho_{51} + i\Omega_{IR2}\rho_{41} - i\Omega_p\rho_{35} \quad (2.136)$$

$$\dot{\rho}_{41} = -[i(\Delta_p - \Delta_c + \Delta_{IR2}) + \gamma_{41}]\rho_{41} + i\Omega_{IR2}\rho_{31} + i\Omega_{IR1}\rho_{21} - i\Omega_p\rho_{45} \quad (2.137)$$

$$\dot{\rho}_{21} = -[i(\Delta_p - \Delta_c + \Delta_{IR2} - \Delta_{IR1}) + \gamma_{21}]\rho_{21} + i\Omega_{IR1}\rho_{41} - i\Omega_p\rho_{25} \quad (2.138)$$

$$\chi_P^{(1)} = \frac{i2N\wp^2/\epsilon_0\hbar \left[L_2L_3 + \Omega_1^2 + \frac{L_3\Omega_2^2}{L_1} \right]}{\left[L_4L_3L_2 + L_4\Omega_1^2 + L_2\Omega_c^2 + \frac{L_3L_4\Omega_2^2}{L_1} \right]} \quad (2.139)$$

Fig. 2.64 Transmission coefficient versus wavelength with different environment temperature [136] $\Omega_c = 10^{12} \text{ s}^{-1}$, $\Omega_p = 10^8 \text{ s}^{-1}$, $\Omega_{IR} = 5^{11}$, $\Delta_{IR1} = \Delta_{IR2} = \Delta_c = \Delta_p = 0$, $T = 0 \text{ K}$, $N_a = 10^{20} \text{ cm}^{-3}$, $\gamma_{51} = 10^{12} \text{ s}^{-1}$, $\gamma_{31} = \gamma_{21} = 5 \times 10^9 \text{ s}^{-1}$, $\gamma_{41} = 10^{11}$, $\wp = 10^{-10} \text{ e} - \text{cm}$



where $L_1 = [i(\Delta_p - \Delta_c + \Delta_1 - \Delta_2) + \gamma_{ba}]$, $L_2 = [i(\Delta_p - \Delta_c + \Delta_1) + \gamma_{da}]$, $L_3 = [i(\Delta_p - \Delta_c) + \gamma_{ca}]$ and $L_4 = [i(\Delta_p) + \gamma_{ea}]$. In this system, we show that the improper effect of environment temperature on signal energy is reduced. Finally, we cancel out the effect of environment temperature by introducing another atomic system.

Figure 2.64 shows the effect of environment temperature on the operation of this system. The environment temperature energy is added to both of IR radiations. If two infrared radiations are selected to be same therefore effect of thermal energy can be eliminated. It is observed that with increasing the temperature from $T = 0 \text{ K}$ (dashed line) to $T = 300 \text{ K}$ (solid line), one of the central doublet shifts more but the other one shifts as little as 4 nm. If in this case we try to increase the refractive index of mater from 1 to 1.35 [$n_{\text{refractive}} = 1 \rightarrow 3.5$ (for GaAs)], the wavelength shift reduces to 1.1 nm.

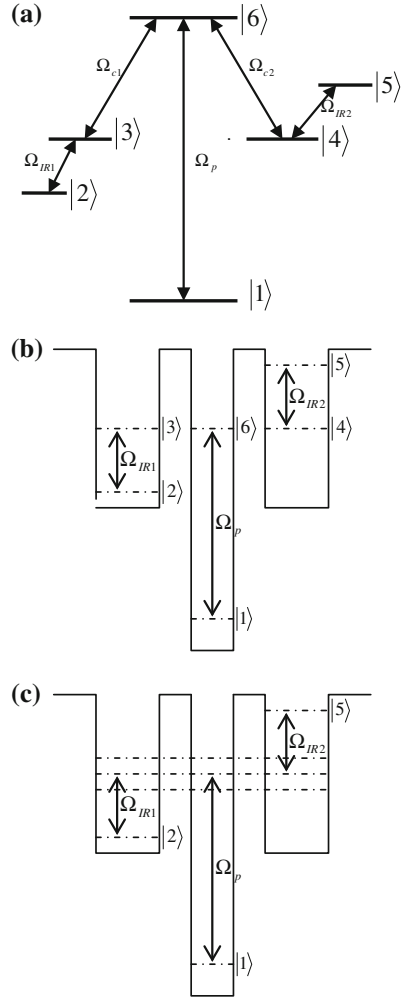
Simulated results for the 5-level atomic system presented that in spite of some limitations, this system shows some promise in canceling out the effect environment temperature. In the above atomic systems, we minimized the environment temperature effect on the operation of the systems and cannot cancel out exactly the environment temperature effect.

Figure 2.65a shows the schematic of 6-level atomic system. In this system, we have two control fields and two IR fields, which both IR fields and control fields are the same. We should isolate the environment thermal energy from incoming infrared radiation. The effect of environment temperature is like a detuning in IR field. If we use two IR fields, we can cancel the effect of detuning, because their thermal energies are the same. This 6-levels system may be realized with an asymmetric multi-quantum well structure such as Fig. 2.65b, c.

According to discussed problems the optical susceptibility in 6-levels atomic system, can be written by [136, 138, 140]:

$$\dot{\rho}_{61} = -[i(\Delta_p) + \gamma_{61}] \rho_{61} + i\Omega_{c1} \rho_{31} + i\Omega_{c2} \rho_{41} + i\Omega_p \rho_{11} - i\Omega_p \rho_{66} \quad (2.140)$$

Fig. 2.65 **a** Schematic of 6-level atomic system, **b** realization of 6-level atomic system with quantum well, and **c** the effect of coupling well on splitting of energy levels [136]



$$\dot{\rho}_{31} = -[i(\Delta_p - \Delta_{c1}) + \gamma_{31}]\rho_{31} + i\Omega_{c1}\rho_{61} + i\Omega_{IR1}\rho_{21} - i\Omega_p\rho_{36} \quad (2.141)$$

$$\dot{\rho}_{41} = -[i(\Delta_p - \Delta_{c2}) + \gamma_{41}]\rho_{41} + i\Omega_{c2}\rho_{61} + i\Omega_{IR2}\rho_{51} - i\Omega_p\rho_{46} \quad (2.142)$$

$$\dot{\rho}_{51} = -[i(\Delta_p - \Delta_{c2}) + \gamma_{51}]\rho_{51} + i\Omega_{IR2}\rho_{41} - i\Omega_p\rho_{56} \quad (2.143)$$

$$\dot{\rho}_{21} = -[i(\Delta_p - \Delta_{c1} - \Delta_{IR1}) + \gamma_{21}]\rho_{21} + i\Omega_{IR1}\rho_{31} - i\Omega_p\rho_{26} \quad (2.144)$$

$$\chi_{41}^{(1)} = \left[\frac{2N\hbar^2/e_0\hbar \left[-L_4L_5 + \frac{-\Omega_{IR1}^2[L_5]}{L_1} + \frac{-\Omega_{IR2}^2[L_4]}{L_2} + \frac{-\Omega_{IR1}^2\Omega_{IR2}^2}{L_1L_2} \right]}{\left[\frac{-L_3\Omega_{IR1}^2\Omega_{IR2}^2}{L_1L_2} \right] + \left[\frac{-L_3L_4\Omega_{IR2}^2}{L_2} \right] + \left[\frac{-L_3L_5\Omega_{IR1}^2}{L_1} \right] + [-L_3L_4L_5] + [-L_4\Omega_{c2}^2] + [-L_5\Omega_{c1}^2] + \left[\frac{-\Omega_{c1}^2\Omega_{IR2}^2}{L_2} \right] + \left[\frac{-\Omega_{c2}^2\Omega_{IR1}^2}{L_1} \right]} \right] \quad (2.145)$$

where $L_1 = [i(\Delta_p - \Delta_{c1} - \Delta_{IR1}) + \gamma_{21}]$, $L_2 = [i(\Delta_p + \Delta_{c1} + \Delta_{IR2}) + \gamma_{61}]$, $L_3 = [i\Delta_p + \gamma_{41}]$, $L_4 = [i(\Delta_p - \Delta_{c1}) + \gamma_{31}]$ and $L_5 = [i(\Delta_p + \Delta_{c2}) + \gamma_{51}]$.

We show that the operation of the photodetector design based on this atomic system is completely independent from the environment temperature.

Now, we show that using 6-level atomic system the effect of environment temperature completely can be removed. This behavior of the new structure is very interesting from the room temperature terahertz detectors point of view. Figure 2.66 shows the effect of these two IR signals on the optical susceptibility. If one of the control fields is on, Autler–Townes doublet is generated and when the other control field becomes also active, Autler–Townes splits more. In the presence of IR fields, we see a small broadness of Autler–Townes doublet. Also it is observed that a sharp impulse in the band gap generated which magnitude of it changes with the Rabi frequency of infrared signal.

Fig. 2.66 **a** Real and **b** imaginary parts of susceptibility versus wavelength where *dashed line curve* corresponds one of the control fields is on, for *dot line* both control fields are on and for *solid line*, both control fields and IR fields are on [136]
 $\Omega_c = 10^{13} \text{ s}^{-1}$, $\Omega_p = 10^8 \text{ s}^{-1}$, $\Omega_{IR} = 5 \times 10^{11}$,
 $\Delta_{IR1} = \Delta_{IR2} = \Delta_c =$
 $\Delta_p = 0$, $T = 0 \text{ K}$, $N_a =$
 10^{20} cm^{-3} , $\gamma_{61} = 10^{12} \text{ s}^{-1}$,
 $\gamma_{21} = 5 \times 10^9 \text{ s}^{-1}$,
 $\gamma_{31} = \gamma_{41} = 10^9 \text{ s}^{-1}$,
 $\gamma_{51} = 10^{11} \text{ s}^{-1}$,
 $\varphi = 10^{-10} \text{ e} - \text{cm}$

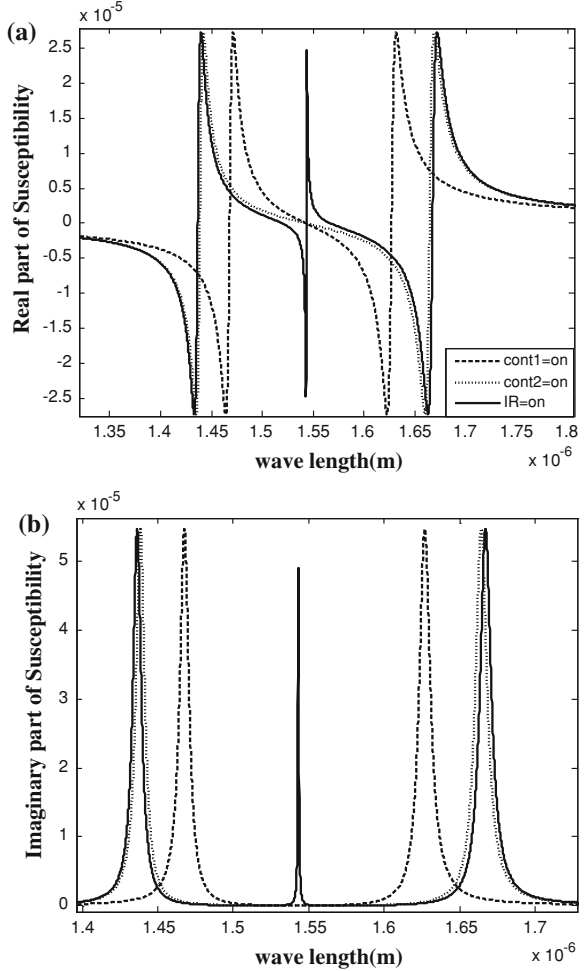


Fig. 2.67 Transmission coefficient versus wavelength with different infrared radiations [136]

$$\begin{aligned}\Omega_c &= 10^{12} \text{ s}^{-1}, \Omega_p = 10^8 \text{ s}^{-1}, \Omega_{IR} = 5 \times 10^{11}, \\ \Delta_{IR1} &= \Delta_{IR2} = \Delta_c = \Delta_p = 0, T = 0 \text{ K}, \\ N_a &= 10^{20} \text{ cm}^{-3}, \gamma_{61} = 10^{12} \text{ s}^{-1}, \\ \gamma_{21} &= 5 \times 10^9 \text{ s}^{-1}, \gamma_{31} = 10^9 \text{ s}^{-1}, \gamma_{51} = 10^{11} \text{ s}^{-1}, \wp = 10^{-10} \text{ e - cm}\end{aligned}$$

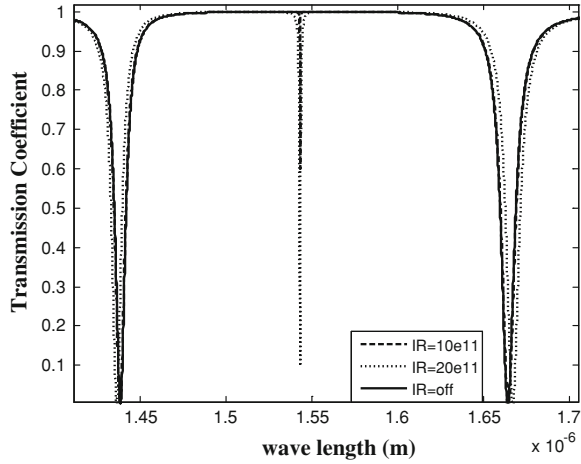


Fig. 2.68 Transmission coefficient versus wavelength with different temperatures [136]

$$\begin{aligned}\Omega_c &= 10^{12} \text{ s}^{-1}, \Omega_p = 10^8 \text{ s}^{-1}, \Omega_{IR} = 5^{11}, \\ \Delta_{IR1} &= \Delta_{IR2} = \Delta_c = \Delta_p = 0, N_a = 10^{20} \text{ cm}^{-3}, \\ \gamma_{61} &= 10^{12} \text{ s}^{-1}, \gamma_{21} = 5 \times 10^9 \text{ s}^{-1}, \gamma_{31} = \gamma_{41} = 10^9 \text{ s}^{-1}, \gamma_{51} = 10^{11} \text{ s}^{-1}, \\ \wp &= 10^{-10} \text{ e - cm}\end{aligned}$$

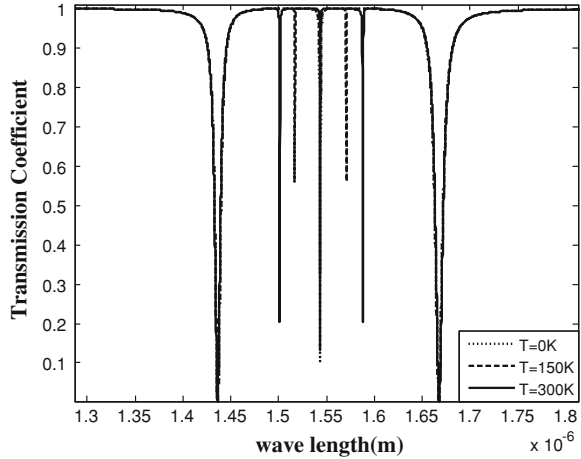


Figure 2.67 shows the effect of different infrared radiations on this atomic system. In this system in the presence of IR signal, it is observed that a sharp impulse generated between the Autler–Townes doublets which magnitude changes with IR radiation. So really IR-photodetector operation is obtained.

Figure 2.68 shows the effect of different environment temperatures on the system operation. It is observed that in presence of temperature two other absorption peaks are appeared and with increasing the applied temperature the observed peaks are broadened. Also, we found that the appeared peak in the central part of the spectrum is independent of temperature. This is interesting for room temperature operation.

In the above section some of simulated results for IR photodetectors based on EIT process were proposed and it was observed that room temperature operation

can be concluded. We think that the proposed structures can be realized by quantum wells and dots.

In the conventional infrared photodetectors, the incoming photon or the environment temperature directly excites the ground state electrons to higher energy levels and in the presence of electric field, these electrons are collected as a photocurrent and thermionic dark current [86, 136, 138]. Therefore in high temperature and terahertz applications, the dark current inhabits the correct detection of signal [136, 138]. However in our proposed EIT-based photodetector, the electromagnetic field of terahertz infrared radiation interfere with the electromagnetic field of short-wavelength (1–2 μm) probe field and modify the absorption characteristic of probe field. Therefore the incoming terahertz IR light and the environment temperature do not directly excite electrons, but affect the absorption characteristics of short-wavelength probe optical field. In fact we convert the incoming terahertz IR signal to short-wavelength optical field through EIT phenomena [138, 140], where such problems are not critical in this rang of detection.

In many aspects the eigen-states in quantum well are like atomic systems [140, 141]. In the atomic systems if two fields are coupled and interfere with each other and one of them be strong, so the optical stark effect is created. There is a shift in absorption characteristic, so we see two new absorptions where there was transparency. In this case we say the atomic states are splitting and this is known as an EIT. However in quantum well structures the stark effect can be created with the coupling two wells and the EIT like condition may be appeared [140, 141].

Figure 2.69 shows a 4-subbands asymmetric double quantum well structure. In Fig. 2.69a an infrared field is applied between states 2, 3 and a probe field is applied between states 1, 4. The barrier potential between two well is too thick that two wells and their wave functions are separated (uncoupled). In other word all states are localized. In this case there is no coupling between infrared field and probe field and therefore the EIT like condition is not happen. Thus we are not able to control the absorption characteristic through infrared field. In Fig. 2.69b the

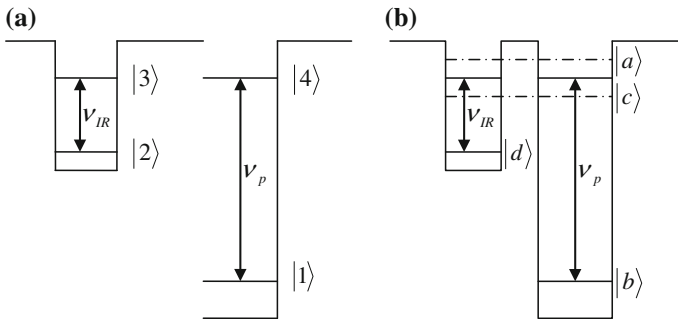


Fig. 2.69 **a** Asymmetric double quantum well with too thick barrier (uncoupled wells) and **b** asymmetric double quantum well with thin barrier (coupled wells) [136]

barrier potential (V_0) between two well is thin (coupled wells) and the eigen-states be in the same energy or in the range of electron–LO phonon scattering or electron–electron scattering, so the wave functions of two wells can see each other through thin barrier (resonant-mode). These two states ($|4\rangle, |3\rangle$) are combined and split by $\langle 3|V_0|4\rangle$, so the two new states ($|a\rangle, |c\rangle$) are created. This effect is like to stark effect in an atomic system which is introduced by strong pump field. In the following we show the EIT like pattern can be observed in this quantum well structure.

Using the density matrix formalism, we begin to describe the dynamic response of the proposed 4-subband quantum well structure. By adopting the standard approach (this method has described the results in several experimental papers [142–144] and has been used in several theoretical papers [145–147]) under the electro-dipole and rotating-wave approximations, we can easily obtain the time-dependent density-matrix equations of motion as follows:

$$H = \hbar \begin{bmatrix} v_b & 0 & -\Omega_p e^{i v_p t} & -q\Omega_p e^{i v_p t} \\ 0 & v_d & -\Omega_{IR} e^{i v_{IR} t} & -k\Omega_{IR} e^{i v_{IR} t} \\ -\Omega_p e^{-i v_p t} & -\Omega_{IR} e^{-i v_{IR} t} & v_c & 0 \\ -q\Omega_p e^{-i v_p t} & -k\Omega_{IR} e^{-i v_{IR} t} & 0 & v_4 \end{bmatrix} \quad (2.146)$$

$$\begin{aligned} \dot{\rho}_{ab} = & -i\left(\Delta_p + \frac{\omega_S}{2} + \Gamma_{ab}\right)\rho_{ab} + iq\Omega_p\rho_{bb} - iq\Omega_p\rho_{aa} \\ & + ik\Omega_{IR}\rho_{db} - i\Omega_p\rho_{ac} \end{aligned} \quad (2.147)$$

$$\begin{aligned} \dot{\rho}_{db} = & -i(\Delta_p - \Delta_{IR} + \Gamma_{db})\rho_{db} + i\Omega_{IR}\rho_{cb} + ik\Omega_{IR}\rho_{ab} \\ & - i\Omega_p\rho_{dc} - iq\Omega_p\rho_{da} \end{aligned} \quad (2.148)$$

$$\begin{aligned} \dot{\rho}_{cb} = & -i\left(\Delta_p - \frac{\omega_S}{2} + \Gamma_{cb}\right)\rho_{cb} + i\Omega_p\rho_{bb} + i\Omega_{IR}\rho_{db} \\ & - iq\Omega_p\rho_{ca} - i\Omega_p\rho_{cc} \end{aligned} \quad (2.149)$$

$$\dot{\rho}_{ac} = -(i\omega_S + \Gamma_{ac})\rho_{ac} - i\Omega_p\rho_{ab} + iq\Omega_p\rho_{bc} - i\Omega_{IR}\rho_{ad} + ik\Omega_{IR}\rho_{dc} \quad (2.150)$$

$$\begin{aligned} \dot{\rho}_{cd} = & -i\left(\Delta_{IR} - \frac{\omega_S}{2} + \Gamma_{cd}\right)\rho_{cd} + i\Omega_p\rho_{bd} + i\Omega_{IR}\rho_{dd} \\ & - i\Omega_{IR}\rho_{cc} - ik\Omega_{IR}\rho_{ca} \end{aligned} \quad (2.151)$$

$$\begin{aligned} \dot{\rho}_{ad} = & -i\left(\Delta_{IR} + \frac{\omega_S}{2} + \Gamma_{ad}\right)\rho_{ad} + iq\Omega_p\rho_{bd} + ik\Omega_{IR}\rho_{dd} \\ & - ik\Omega_{IR}\rho_{aa} - i\Omega_{IR}\rho_{ac} \end{aligned} \quad (2.152)$$

where $\omega_s = v_{ab} - v_{cb}$, $v_0 = \frac{v_{ab} + v_{cb}}{2}$, $v'_0 = \frac{v_{ad} + v_{cd}}{2}$ and $\Delta_p = v_0 - v_p$, $\Delta_{IR} = v'_0 - v_{IR}$. The population and dephasing decay rates are added phenomenologically in the above density matrix equations. The population decay rate for subband $|j\rangle$ (due to LO-phonon emission events) is denoted by γ_j . The total decay rates are given by:

$$\begin{aligned}
\Gamma_{cb} &= \gamma_c + \gamma_{cb}^{\text{dph}}, \\
\Gamma_{ab} &= \gamma_a + \gamma_{ab}^{\text{dph}}, \\
\Gamma_{db} &= \gamma_d + \gamma_{db}^{\text{dph}} \quad (\gamma_d = \gamma_{cd} + \gamma_{ad}), \\
\Gamma_{ac} &= \gamma_a + \gamma_c + \gamma_{ac}^{\text{dph}}, \Gamma_{cd} = \gamma_c + \gamma_d + \gamma_{cd}^{\text{dph}} \quad \text{and} \\
\Gamma_{ad} &= \gamma_a + \gamma_d + \gamma_{ad}^{\text{dph}}
\end{aligned} \tag{2.153}$$

In these expressions γ_{ij} (determined by electron–electron, interfaces roughness, and phonon scattering process) is the dephasing decay rate of the $|i\rangle \leftrightarrow |j\rangle$ transition. In this case the probe field interacts with both the sub band transitions $|b\rangle \leftrightarrow |c\rangle$ and $|b\rangle \leftrightarrow |a\rangle$ simultaneously with the Rabi frequencies Ω_p and $q\Omega_p$ ($q = \mu_{ab}/\mu_{cb}$ is dipole moment of relevant transition). On the other hand the terahertz-infrared field interacts with both $|d\rangle \leftrightarrow |c\rangle$ and $|d\rangle \leftrightarrow |a\rangle$ with the Rabi frequencies Ω_{IR} and $K\Omega_p$ (where $K = \mu_{ad}/\mu_{cd}$ is dipole moment of relevant transition). The optical susceptibility can be written as:

$$\chi = \frac{P}{\varepsilon_0 E} = \frac{2N_a(\wp_{ab}^2 \rho_{ab} + q\wp_{cb}^2 \rho_{cb})}{\varepsilon_0 \Omega_p \hbar} \tag{2.154}$$

where Ω_p and N_a are the Rabi frequency of the probe field and the carrier density, respectively. The environment average thermal energy is considered as follows:

$$E_{\text{thermal}} = \frac{3}{2}KT \tag{2.155}$$

where K and T are the thermal energy, the Boltzmann constant and temperature in Kelvin, respectively. The effect of the above energy on the system operation is considered by adding this energy to the signal energy as follow:

$$E_T = E_{\text{IR}} + E_{\text{thermal}} \tag{2.156}$$

This section shows simulated results including transmission coefficient in proposed 4-subband quantum well structure. The transmission coefficient of probe field is proportional to the imaginary part of susceptibility [140]. Figure 2.70 shows the transmission coefficient of this structure. According to the matrix density equations, when the IR radiation is off, we will see two sharp absorption (Autler–Townes doublet) in the system transmission coefficient which are related to the transition, $|b\rangle \leftrightarrow |a\rangle$ and $|b\rangle \leftrightarrow |c\rangle$ respectively. The width of this Autler–Townes doublet is proportional to the splitting energy ($\langle 3|V_0|4\rangle$).

Figure 2.71 shows the effect of IR radiation on transmission coefficient of probe field in proposed asymmetric quantum well system. In the presence of IR radiation, a new sharp absorption is created in between the Autler–Townes doublet (for $K = 1$, $q = 1$ where K and q are the dipole moments). Solving the Schrödinger equation for this 4-subbands quantum well shows that the splitting energy is

Fig. 2.70 Transmission coefficient versus wavelength for double asymmetric quantum wells systems ($\Omega_{IR} = 0 \text{ s}^{-1}$, $\Omega_p = 10^8 \text{ s}^{-1}$, $\Delta\Omega_{IR} = 0$, $E_S = 100 \text{ meV}$, $N_a = 10^{18} \text{ cm}^{-3}$, $\Gamma_{ab} = \gamma_a + \gamma_{ab}^{dph} \approx 4.9 \text{ meV}$, $\Gamma_{cb} = \gamma_b + \gamma_{cb}^{dph} \approx 4.2 \text{ meV}$, $\Gamma_{ac} = \gamma_a + \gamma_c + \gamma_{ac}^{dph} \approx 8.3 \text{ meV}$, $K = \frac{\mu_{ad}}{\mu_{cd}} = 1$, $q = \frac{\mu_{ab}}{\mu_{cb}} = 1$, $T = 0 \text{ K}$)

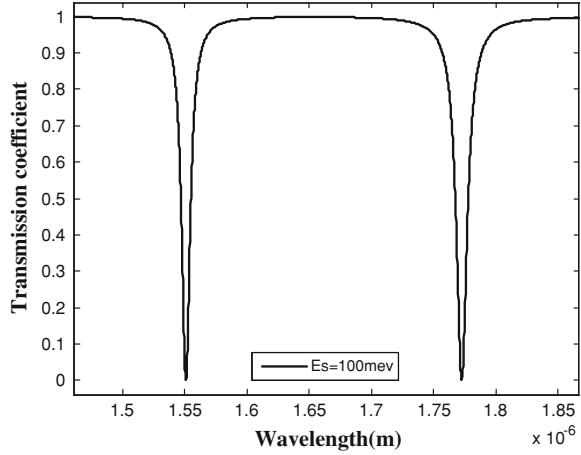
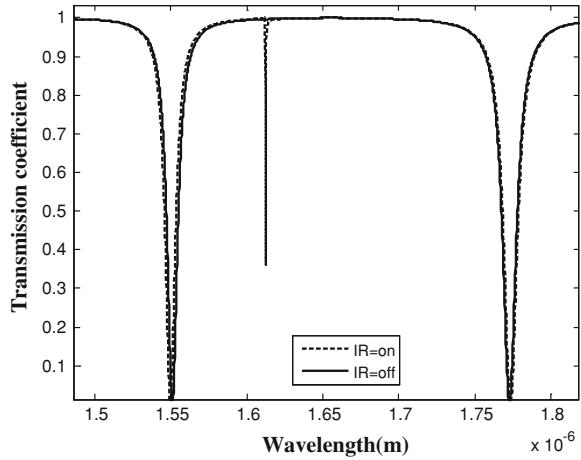


Fig. 2.71 Transmission coefficient versus wavelength for IR signal off (*solid line*) and IR signal on (*dash line*) with $K = 1$, $q = 1$ ($\Omega_{IR} = 20 * 10^{11} \text{ s}^{-1}$, $\Omega_p = 10^8 \text{ s}^{-1}$, $\Delta\Omega_{IR} = 20\%$, $E_S = 100 \text{ meV}$, $N_a = 10^{18} \text{ cm}^{-3}$, $\Gamma_{ab} = \gamma_a + \gamma_{ab}^{dph} \approx 4.9 \text{ meV}$, $\Gamma_{cb} = \gamma_b + \gamma_{cb}^{dph} \approx 4.2 \text{ meV}$, $\Gamma_{ac} = \gamma_a + \gamma_c + \gamma_{ac}^{dph} \approx 8.3 \text{ meV}$, $K = \frac{\mu_{ad}}{\mu_{cd}} = 1$, $q = \frac{\mu_{ab}}{\mu_{cb}} = 1$, $T = 0 \text{ K}$)



not so much (10–100 meV), so the magnitude of dipole moments K and q are closer to one.

Figure 2.72 shows the effect of IR intensity on the transmission coefficient of optical probe field. It is clear that the magnitude of this new absorption is sensitive to the infrared intensity. Therefore this asymmetric double quantum well structure can be used as a novel basic cell for terahertz-photodetectors.

Figure 2.73 shows the effect of IR-detuning on the transmission coefficient. When detuning is zero (IR field and probe field are coupled to the center of states $|a\rangle$ and $|b\rangle$) there is no absorption in the transmission coefficient. In fact due to symmetric case of system, the interaction of optical electromagnetically field with two states are the same and cancel out each other. Otherwise when the IR field and probe field are detuned, the new sharp absorption peaks are observed and their magnitudes are sensitive to the IR intensity.

Fig. 2.72 Transmission coefficient versus wavelength for different IR intensity with $K = 1, q = 1$ ($\Omega_p = 10^8 \text{ s}^{-1}, \Delta\Omega_{\text{IR}} = 20\%, E_S = 100 \text{ meV}, N_a = 10^{18} \text{ cm}^{-3}, \Gamma_{ab} = \gamma_a + \gamma_{ab}^{\text{dph}} \approx 4.9 \text{ meV}, \Gamma_{cb} = \gamma_b + \gamma_{cb}^{\text{dph}} \approx 4.2 \text{ meV}, \Gamma_{ac} = \gamma_a + \gamma_c + \gamma_{ac}^{\text{dph}} \approx 8.3 \text{ meV}, K = \frac{\mu_{ad}}{\mu_{cd}} = 1, q = \frac{\mu_{ab}}{\mu_{cb}} = 1, T = 0 \text{ K}$)

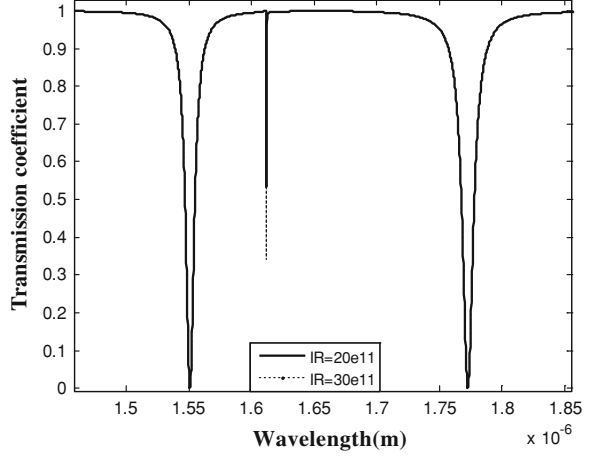
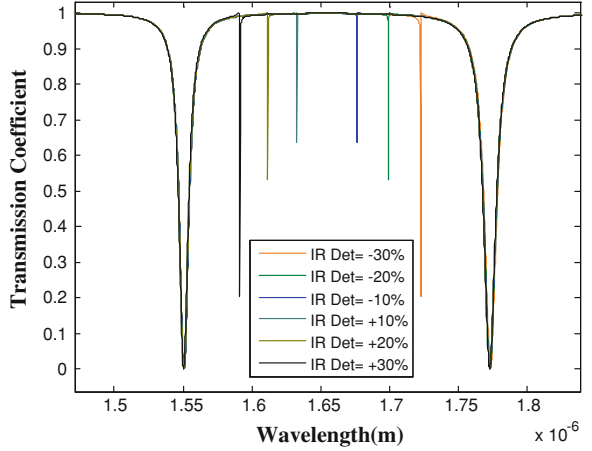


Fig. 2.73 Transmission coefficient versus wavelength for different IR detuning with $K = 1, q = 1$ ($\Omega_{\text{IR}} = 20 * 10^{11} \text{ s}^{-1}, \Omega_p = 10^8 \text{ s}^{-1}, E_S = 100 \text{ meV}, N_a = 10^{18} \text{ cm}^{-3}, \Gamma_{ab} = \gamma_a + \gamma_{ab}^{\text{dph}} \approx 4.9 \text{ meV}, \Gamma_{cb} = \gamma_b + \gamma_{cb}^{\text{dph}} \approx 4.2 \text{ meV}, \Gamma_{ac} = \gamma_a + \gamma_c + \gamma_{ac}^{\text{dph}} \approx 8.3 \text{ meV}, K = \frac{\mu_{ad}}{\mu_{cd}} = 1, q = \frac{\mu_{ab}}{\mu_{cb}} = 1, T = 0 \text{ K}$)



If we are able to change the dipole moment ratios, we can see some interesting cases. Figure 2.74 shows the effect of IR signal on the transmission coefficient for $K = 2.5$ and $q = 1$. It is clear that the new peak appears in center of spectrum and its magnitude is related to the IR intensity. In this case the interaction of electromagnetic field with two states is different and can not cancel out each other. Therefore a new absorption peak can be occurred.

There is another interesting case. Figure 2.75 shows the effect of IR radiation on the transmission coefficient when the IR field is resonant with the transition energy $|d\rangle \leftrightarrow |a\rangle$ or $|d\rangle \leftrightarrow |c\rangle$ (detuning $= \pm 50\%$). We see a new sharp transparency in the spectrum where there was absorption. Figure 2.76 shows the magnitude of this new transparency is changed when the IR intensity changes.

Finally we investigate the effect of environment temperature on operation of the proposed quantum well structure. The environment thermal energy may be added

Fig. 2.74 Transmission coefficient versus wavelength with different IR intensity for $K = 2.5$, $q = 1$ ($\Omega_{IR} = 20 * 10^{11} \text{ s}^{-1}$, $\Omega_p = 10^8 \text{ s}^{-1}$, $\Delta\Omega_{IR} = 0\%$, $E_S = 100 \text{ meV}$, $N_a = 10^{18} \text{ cm}^{-3}$, $\Gamma_{ab} = \gamma_a + \gamma_{ab}^{dph} \approx 4.9 \text{ meV}$, $\Gamma_{cb} = \gamma_b + \gamma_{cb}^{dph} \approx 4.2 \text{ meV}$, $\Gamma_{ac} = \gamma_a + \gamma_c + \gamma_{ac}^{dph} \approx 8.3 \text{ meV}$, $K = \frac{\mu_{ad}}{\mu_{cd}} = 2.5$, $q = \frac{\mu_{ab}}{\mu_{cb}} = 1$, $T = 0 \text{ K}$)

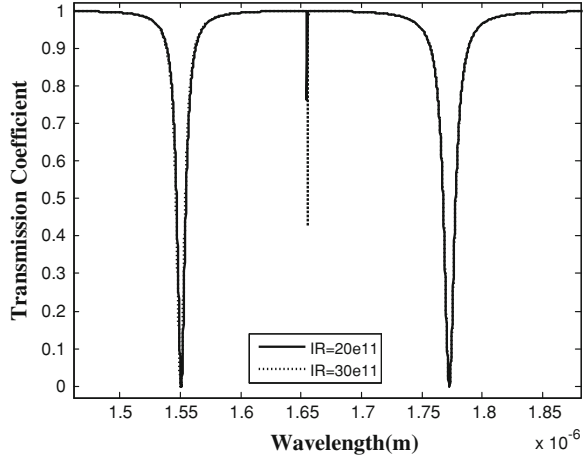
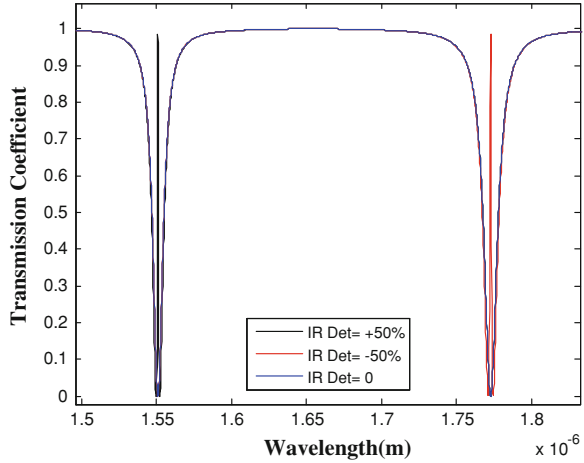


Fig. 2.75 Transmission coefficient versus wavelength for IR transition $|d\rangle \leftrightarrow |a\rangle$ and $|d\rangle \leftrightarrow |c\rangle$ (detuning = $\pm 50\%$) ($\Omega_{IR} = 20 * 10^{11} \text{ s}^{-1}$, $\Omega_p = 10^8 \text{ s}^{-1}$, $\Delta\Omega_{IR} = 50\%$, $E_S = 100 \text{ meV}$, $N_a = 10^{18} \text{ cm}^{-3}$, $\Gamma_{ab} = \gamma_a + \gamma_{ab}^{dph} \approx 4.9 \text{ meV}$, $\Gamma_{cb} = \gamma_b + \gamma_{cb}^{dph} \approx 4.2 \text{ meV}$, $\Gamma_{ac} = \gamma_a + \gamma_c + \gamma_{ac}^{dph} \approx 8.3 \text{ meV}$, $K = \frac{\mu_{ad}}{\mu_{cd}} = 2.5$, $q = \frac{\mu_{ab}}{\mu_{cb}} = 1$, $T = 0 \text{ K}$)



to the incoming target IR signal and this effect inhibits the correct IR detection in the conventional photodetectors. However we show that this problem is not critical in our proposed EIT-based 4-subbands asymmetric quantum well structure. In the EIT-based structure the environment thermal energy cannot directly excite electrons (state $|b\rangle$ is populated but state $|d\rangle$ is not) but it causes some detuning in IR field. Figure 2.77 shows the effect of environment temperature on the transmission coefficient. If we couple IR without detuning, the environment temperature is added to IR signal and case a detuning (for $T = 0 \text{ K} \rightarrow 300 \text{ K}$, $\Delta\lambda \approx 80 \text{ nm}$). Now the effect of room temperature variations is considered. The 4 nm shift of wavelength for 20°C of room temperature variation is observed. It should be mentioned that when the refractive index of material increased ($n_{\text{refractive}} = 1 \rightarrow$

Fig. 2.76 Transmission coefficient versus infrared Rabi frequency for transition $|d\rangle \leftrightarrow |a\rangle$ and $|d\rangle \leftrightarrow |c\rangle$ ($\Omega_p = 10^8 \text{ s}^{-1}$, $\Delta\Omega_{\text{IR}} = 50\%$, $E_S = 100 \text{ meV}$, $N_a = 10^{18} \text{ cm}^{-3}$, $\Gamma_{ab} = \gamma_a + \gamma_{ab}^{\text{dph}} \approx 4.9 \text{ meV}$, $\Gamma_{cb} = \gamma_b + \gamma_{cb}^{\text{dph}} \approx 4.2 \text{ meV}$, $\Gamma_{ac} = \gamma_a + \gamma_c + \gamma_{ac}^{\text{dph}} \approx 8.3 \text{ meV}$, $K = \frac{\mu_{ad}}{\mu_{cd}} = 1$, $q = \frac{\mu_{ab}}{\mu_{cb}} = 1$, $T = 0 \text{ K}$)

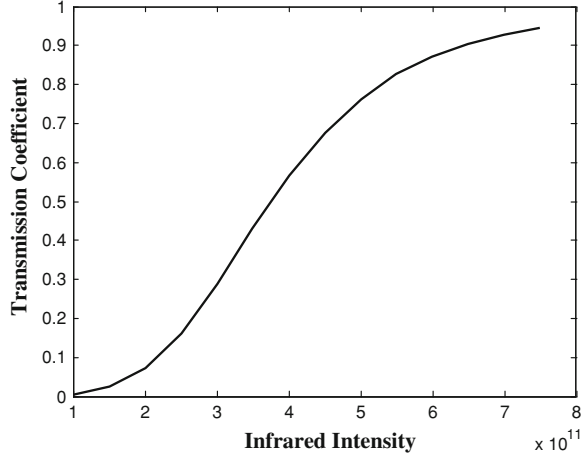
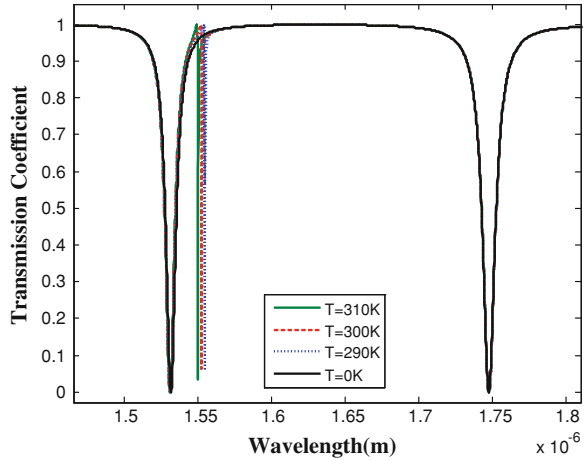


Fig. 2.77 Transmission coefficient versus wavelength for different room temperature with $K = 1$, $q = 1$ ($\Omega_{\text{IR}} = 20 * 10^{11} \text{ s}^{-1}$, $\Omega_p = 10^8 \text{ s}^{-1}$, $\Delta\Omega_{\text{IR}} = 0\%$, $E_S = 100 \text{ meV}$, $N_a = 10^{18} \text{ cm}^{-3}$, $\Gamma_{ab} = \gamma_a + \gamma_{ab}^{\text{dph}} \approx 4.9 \text{ meV}$, $\Gamma_{cb} = \gamma_b + \gamma_{cb}^{\text{dph}} \approx 4.2 \text{ meV}$, $\Gamma_{ac} = \gamma_a + \gamma_c + \gamma_{ac}^{\text{dph}} \approx 8.3 \text{ meV}$, $K = \frac{\mu_{ad}}{\mu_{cd}} = 1$, $q = \frac{\mu_{ab}}{\mu_{cb}} = 1$, $T = 300 \text{ K}$)



3.5(for GaAs)), the wavelength temperature coefficient can be decreased ($\Delta\lambda/\Delta T = 0.2 \text{ nm}/^\circ\text{C} \rightarrow 60 \text{ pm}/^\circ\text{C}$) that is so excellent from practical implementation point of view.

2.6.3 Terahertz Quantum Cascade Photodetector Based on Electromagnetically Induced Transparency

In spite of the numerous reports on QCDs especially in mid-infrared region, there is still lack of studies in terahertz quantum cascade devices since the thermal energy directly excites the ground state electrons to higher energy levels and in the

presence of transport ladder, leads to thermionic dark current [1, 27, 86, 135]. This problem deteriorates the performance of QCD.

A great number of the reported works on QCDs up to now are generally realized in III–V material system [3, 148]. However due to special features of GaN-based material system such as large conduction band offset in III-nitride heterostructures (which provides operation at much shorter wavelengths than other III–V QCDs), III-nitride heterostructures are highly suitable for implementation of such devices. On the other hand, the large lattice mismatch between AlN and GaN (as a deficiency) is not an impediment in QCDs since the barriers throughout the structure must be thin to obtain strong coupling between the wells.

Also, the improvement in the device performance due to the use of a phonon ladder is expected to be largely enhanced in the III-nitride material system, where the LO–phonon interaction is an order of magnitude stronger than in other III–V materials.

One can utilize the interference effect between the terahertz electromagnetic field and the short-wavelength probe field in a QCD active region to modify the absorption characteristic of probe field and achieve to coherence based photo detection [150]. Therefore, the incoming terahertz signal and the thermal energy do not directly excite ground state electrons and the thermionic dark current cancels out. In fact, we interpret the absorption of incoming terahertz signal as the absorption of short-wavelength probe signal by means of EIT Phenomenon [140, 150].

The EIT-based QCD considered in this section is a GaN/AlGaIn heterostructure where the first quantum well of the period is n doped in order to populate the first energy level $E1$ in the conduction band with electrons (the nominal doping concentration of $5 \times 10^{11} \text{ cm}^{-2}$ has been considered). Figure 2.78 presents wave functions associated with each energy subband, in one period of the device. The layer widths in one period from left to right (active region and ladder) are: 20, 16, 10, 22, 10, 30, 20, 6, 20, 6, 20, 7, 20, 8, 20, 10, 20, 11, 20, 13, 20 and 15 Å, respectively.

Fig. 2.78 Schematic of the conduction band profile, wave functions and associated energy levels of the EIT-based terahertz quantum cascade photodetector

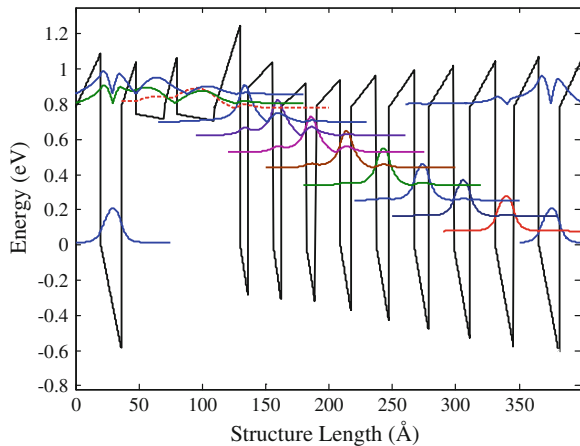
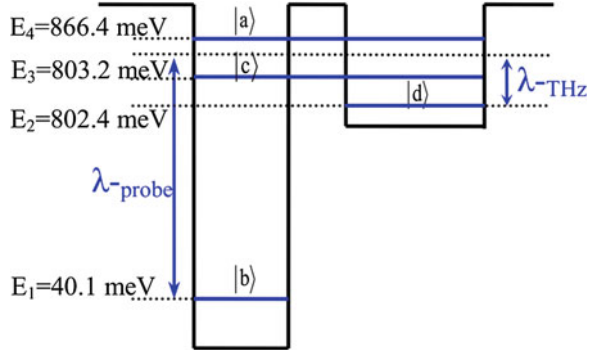


Fig. 2.79 Simplified band diagram of the active region with schematically shown probe and terahertz signal wavelengths



In Fig. 2.79 the active region of the QCD structure is schematically presented of which consist two coupled asymmetric quantum wells. The probe and THz signal wavelengths have been considered to be about 1.55 and 40 μm , respectively. It should be noted that the mid barrier inside the shallow well in Fig. 2.78 is placed to control the THz signal wavelength as a freedom degree of design.

In the interaction picture, the total Hamiltonian for this 4-subband quantum well structure can be written as [140]:

$$H = \hbar \begin{bmatrix} v_b & 0 & -\Omega_p e^{i v_p t} & -q \Omega_p e^{i v_p t} \\ 0 & v_d & -\Omega_{\text{IR}} e^{i v_{\text{IR}} t} & -k \Omega_{\text{IR}} e^{i v_{\text{IR}} t} \\ -\Omega_p e^{-i v_p t} & -\Omega_{\text{IR}} e^{-i v_{\text{IR}} t} & v_c & 0 \\ -q \Omega_p e^{-i v_p t} & -k \Omega_{\text{IR}} e^{-i v_{\text{IR}} t} & 0 & v_4 \end{bmatrix} \quad (2.157)$$

It is assumed that the Rabi frequencies of the probe signal (Ω_p) and THz-signal (Ω_{THz}) to be real. Using the density matrix formalism, one may describe the dynamic response of the proposed 4-subband quantum well structure. Under the electro-dipole and rotating-wave approximations (this method has described the results in experimental reports [142–144] and has been used in several theoretical papers [145–147]), the time-dependent density-matrix equations of motion can be obtained as [140]:

$$\begin{aligned} \dot{\rho}_{ab} = & -[i(\Delta_p + \omega_S/2) + \Gamma_{ab}] \rho_{ab} + iq \Omega_p \rho_{bb} - iq \Omega_p \rho_{aa} \\ & + ik \Omega_{\text{IR}} \rho_{db} - i \Omega_p \rho_{ac} \end{aligned} \quad (2.158)$$

$$\begin{aligned} \dot{\rho}_{cb} = & -[i(\Delta_p - \omega_S/2) + \Gamma_{cb}] \rho_{cb} + i \Omega_p \rho_{bb} + i \Omega_{\text{IR}} \rho_{db} \\ & - iq \Omega_p \rho_{ca} - i \Omega_p \rho_{cc} \end{aligned} \quad (2.159)$$

$$\begin{aligned} \dot{\rho}_{dc} = & -[i(\Delta_{\text{IR}} + \omega_S/2) + \Gamma_{dc}] \rho_{dc} - i \Omega_p \rho_{db} - i \Omega_{\text{IR}} \rho_{dd} \\ & + i \Omega_{\text{IR}} \rho_{cc} + ik \Omega_{\text{IR}} \rho_{ac} \end{aligned} \quad (2.160)$$

$$\begin{aligned} \dot{\rho}_{db} = & -i(\Delta_p + \Delta_{IR} + \Gamma_{db})\rho_{db} + i\Omega_{IR}\rho_{cb} + ik\Omega_{IR}\rho_{ab} \\ & - i\Omega_p\rho_{dc} - iq\Omega_p\rho_{da} \end{aligned} \quad (2.161)$$

$$\begin{aligned} \dot{\rho}_{da} = & -[i(\Delta_{IR} - \omega_s/2) + \Gamma_{da}]\rho_{da} - iq\Omega_p\rho_{db} - ik\Omega_{IR}\rho_{dd} \\ & + ik\Omega_{IR}\rho_{aa} + i\Omega_{IR}\rho_{ca} \end{aligned} \quad (2.162)$$

$$\dot{\rho}_{ac} = -[i\omega_s + \Gamma_{ac}]\rho_{ac} - i\Omega_p\rho_{ab} + iq\Omega_p\rho_{bc} - i\Omega_{IR}\rho_{ad} + ik\Omega_{IR}\rho_{dc} \quad (2.163)$$

where $\omega_s = v_{ab} - v_{cb}$, $v_0 = (v_{ab} + v_{cb})/2$, $v'_0 = (v_{ad} + v_{cd})/2$, $\Delta_p = v_0 - v_p$, $\Delta_{THz} = v'_0 - v_{THz}$ and $q = \mu_{ab}/\mu_{cb}$, $K = \mu_{ad}/\mu_{cd}$. In the above density matrix equations the total decay rates are denoted by Γ_{ij} . In terms of the density matrix notation, the optical polarization is expressed as [140]:

$$P(z, t) = \left[\wp_{ab}(\rho_{ab(z,t)} + \text{c.c.}) + \wp_{cb}(\rho_{cb(z,t)} + \text{c.c.}) \right] \quad (2.164)$$

where \wp_{ij} is dipole moment matrix element between states $|i\rangle$, $|j\rangle$. The linear susceptibility can be calculated from the optical polarization as follows [140]:

$$\chi_p^{(1)} = \frac{2N/\epsilon_0\hbar [\wp_{ab}^2(L_1L_2 + \Omega_{IR}^2) + \wp_{cb}^2(-K\Omega_{IR}\Omega_{IR} + qL_3L_2 + qK\Omega_{IR}^2)]}{L_1L_2L_3 + L_3\Omega_{IR}^2 + L_1 + K^2\Omega_{IR}^2} \quad (2.165)$$

where $L_1 = [i(\Delta_p - \omega_s/2) + \Gamma_{cb}]$, $L_2 = [i(\Delta_p + \Delta_{THz}) + \Gamma_{db}]$, $L_3 = [i(\Delta_p + \omega_s/2) + \Gamma_{ab}]$, $K = \mu_{da}/\mu_{dc}$ and $q = \mu_{ab}/\mu_{cb}$.

The transmission coefficient of probe field is proportional to the imaginary part of susceptibility [149, 150].

Figure 2.80 shows the simulated transmission coefficient of probe field. According to the matrix density equations, when the terahertz radiation is off (Fig. 2.80a), two sharp absorption (like Autler–Townes doublet in atomic system) are appeared which are related to $|b\rangle \leftrightarrow |a\rangle$ and $|b\rangle \leftrightarrow |c\rangle$ transitions, respectively. The energy gap between two absorption peaks is proportional to the splitting energy ($E_4 - E_3$). Figure 2.80b–d show the effect of terahertz radiation intensity on transmission coefficient. In the presence of terahertz radiation, a new sharp absorption is created between the two absorption peaks (interferential state). It is clear that the magnitude of this new absorption is sensitive to the terahertz intensity. Therefore this asymmetric double quantum well structure can be used as a novel active-region cell for terahertz photo-detection. In this feature, the THz signal does not manipulate the active region carriers directly (unlike the conventional THz quantum well photo-detectors) but the interference of the probe and THz signals modifies the absorption coefficient of the active region. This phenomenon may be described as the translation of the THz to probe short wavelength. Thus the cascade ladder coupled to the interferential state of the active region extracts the probe-excited carriers and transport them to consequent period.

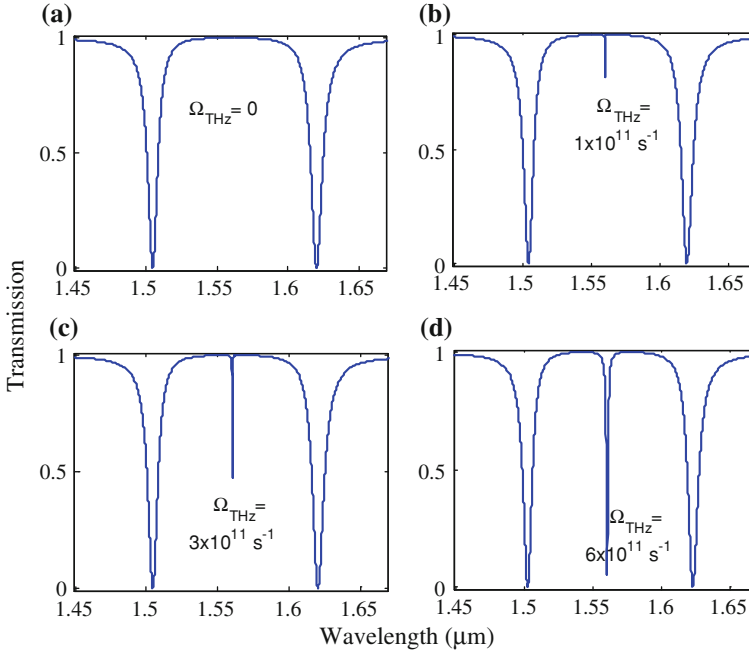
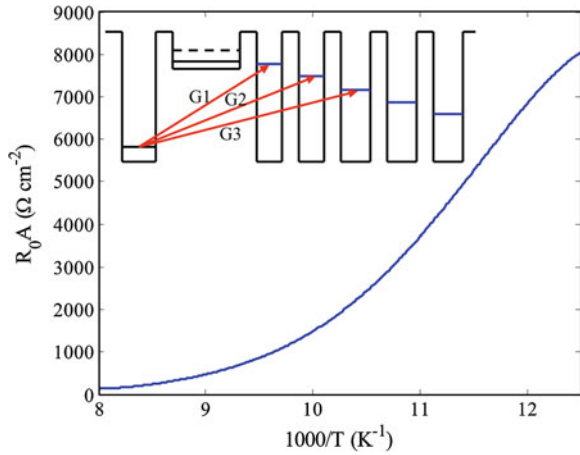


Fig. 2.80 Transmission coefficient of the active region versus wavelength for different THz-Rabi frequencies (Ω_{THz})

Fig. 2.81 Resistivity as a function of $1000/T$. The inset is a schematic of the three dominant transitions (highest transition rates in one period of the structure)



As previous discussions, in a photovoltaic detector, the zero voltage resistance, R_0A (which characterize the dark current-measured in the absence of illumination-and the deduced Johnson noise limited detectivity) should be calculated from $R_0A = k_B T / q^2 \sum_{i \in A} \sum_{j \in B} G_{ij}$, where the term G_{ij} is the phonon mediated global

Table 2.7 Quantities of the three largest transition rates for three sample temperatures in $\text{m}^{-2}\text{s}^{-1}$

Temperature (K)	$G1$	$G2$	$G3$
80	0.83×10^{17}	1.1×10^{13}	2.3×10^8
100	0.6×10^{18}	1.7×10^{14}	3.2×10^9
120	5.7×10^{18}	1.1×10^{15}	1.8×10^{10}

transition rate from a subband i of a cascade A to a subband j of a cascade B (in $\text{m}^{-2} \text{s}^{-1}$) [4, 5]. R_{0A} can usually be described with an activation energy E_a , corresponding to the energy of the transition responsible for electron transfer from one contact to the other.

Figure 2.81 presents the resistivity at R_{0A} as a function of $1,000/T$ where T is the temperature of the sample for the structure. The inset of the Fig. 2.68 schematically illustrates the three largest G_{ij} quantities ($G1$, $G2$ and $G3$) obtained in the simulation where the values are reported in Table 2.7 in 80, 100 and 120 K as sample temperatures.

References

1. Levine, B.F.: Quantum-well infrared photodetectors. J. Appl. Phys. **74**, R1–R81 (1993)
2. Graf, M.: Design and characterization of far- and mid-infrared quantum cascade detector. Trafford Publishing, Bloomington (2007)
3. Koeniguer, C., Dubois, G., Gomez, A., Berger, V.: Electronic transport in quantum cascade structures at equilibrium. Phys. Rev. B. **74**(23), 235325-1–235325-6 (2006)
4. Radovanović, J., Milanović, V., Ilkonić, Z., Indjin, D., Harrison, P.: Electron–phonon relaxation rate. J. Appl. Phys. **97**, 103109-1–103109-5 (2005)
5. Ferreira, R., Bastard, G.: Evaluation of some scattering times for electrons in unbiased and biased signal- and multiple quantum well structures. Phys. Rev. B. **40**, 1074–1086 (1989)
6. Ozturk, E., Sokmen, I.: Intersubband transitions in quantum wells. Appl. Phys. D. **36**, 2457–2464 (2003)
7. Rosencher, E., Vinter, B.: Optoelectronics. Cambridge University Press, Cambridge (2002)
8. Beck, W.A.: Photoconductive gain and generation-recombination noise in multiple-quantum-well infrared detectors. Appl. Phys. Lett. **63**, 3589–3591 (1993)
9. Levine, B.F., Bethea, C.G., Choi, K.K., Walker, J., Malik, R.J.: Tunneling lifetime broadening of the quantum well intersubband photoconductivity spectrum. Appl. Phys. Lett. **53**, 231–233 (1988)
10. Suzuki, N., Iizuka, N., Kaneko, K.: Simulation of ultrafast GaN/AlN intersubband optical switches. IEICE Trans. Electron. **E88**–C, 342–348 (2005)
11. Liu, H.C.: Quantum dot infrared photodetector. Optoelectron. Rev. **11**, 1–5 (2003)
12. Su, X., Chakrabarti, S., Bhattacharya, P., Ariyawansa, G., Unil Perera, A.G.: A resonant tunneling quantum-dot infrared photodetector. IEEE J. Quantum Electron. **41**, 974–979 (2005)
13. Choi, K.K.: The physics of quantum well infrared photodetectors. World Scientific, Singapore (1997)
14. Gunapala, S.D., Bandara, S.V.: Quantum well infrared photodetector (QWIP) focal plane arrays. Semicond. Semimet. Ser. **62**, 1–83 (1999)
15. Steiner, T. (ed.): Semiconductor Nanostructures for Optoelectronic Applications. Artech House, Inc., Boston (2004)

16. Koeniguer, C., Gendron, L., Berger, V.: Analysis of performances of quantum cascade detectors. In: Proceedings of SPIE, vol. 5957, pp. 595704-1–595704-9 (2005)
17. Sarusi, G., Carbone, A., Gunapala, S.D., Liu, H.C. (eds.): High resistance narrow band quantum cascade photodetectors. In: Proceedings of the workshop on quantum well infrared photodetectors QWIP, Castello di Pavone, Torino, Italy, pp. 13–17 (2002)
18. Bastard, G.: Resonant carrier capture by semiconductor QW. *Phys. Rev. B* **33**, 1420–1423 (1986)
19. Brum, J.A., Weil, T., Nagle, J., Vinter, B.: Calculation of capture time of QW in graded-index separate-confinement heterostructures. *Phys. Rev. B* **34**, 2381–2384 (1986)
20. Rosencher, E., Vinter, B., Luc, F., Thibaudau, L., Bois, P., Nagle, J.: Emission and capture of electrons in multiquantum-well structures. *IEEE J. Quantum Electron.* **30**, 2875–2888 (1994)
21. Liu, H.C.: Photoconductive gain mechanism of quantum-well intersubband infrared detectors. *Appl. Phys. Lett.* **60**, 1507–1509 (1992)
22. Kastalsky, A.: Photovoltaic in GaAs/AlGaAs. *Appl. Phys. Lett.* **52**, 1320–1322 (1988)
23. Goossen, K.W., Lyon, S.A.: Performance aspects of a QW detectors. *J. Appl. Phys.* **63**, 5149–5153 (1988)
24. Schneider, H., Larkins, E.C.: Space-charge effects in photovoltaic double barrier quantum well infrared detectors. *Appl. Phys. Lett.* **63**, 782–784 (1993)
25. Schonbein, C.: A GaAs/AlGaAs intersubband photodetector operating at zero bias voltage. *Appl. Phys. Lett.* **68**, 973–975 (1996)
26. Schneider, H., Koidl, P., Schönbein, C., Ehret, S., Larkins, E.C., Bihlmann, G.: Capture dynamics and far-infrared response in photovoltaic quantum well intersubband photodetectors. *Superlatt. Microstruct.* **19**, 347–356 (1996)
27. Schneider, H., Liu, H.C.: *Quantum Well Infrared Photodetectors*. Springer, Berlin (2007)
28. Schneider, H., Schönbein, C., Walther, M., Schwarz, K., Fleissner, J., Koidl, P.: Photovoltaic QWIP the four-zone. *Appl. Phys. Lett.* **71**, 246–248 (1997)
29. Schneider, H., Koidl, P., Walther, M., Fleissner, J., Rehm, R., Diwo, E., Schwarz, K., Weimann, G.: Ten years of QWIP development at Fraunhofer IAF. *Infrared Phys. Tech.* **42**, 283–289 (2001)
30. Berger, V.: French patent, Détecteurs à cascade quantique. National reference number 0109754 (2001)
31. Koehler, R., et al.: Terahertz semiconductor-heterostructure laser. *Nature* **417**, 156–159 (2002)
32. Rostami, A., Motmaen, A., Baghban, H., Rasooli Saghari, H.: Dual-color mid-infrared quantum cascade photodetector in a coupled quantum well structure. In: Proceedings of SPIE-OSA-IEEE Asia communications and photonics, vol. 7631, pp. 76310L–76310L-10 (2009)
33. Ariyawansa, G., Perera, A.G.U., Su, X.H., Chakrabarti, S., Bhattacharya, P.: Multi-color tunneling quantum dot infrared photodetectors operation at room temperature. *Infrared Phys. Tech.* **50**, 156–161 (2007)
34. Chamberlin, D., Robrish, P., Trutna, W., Scallari, G., Giovannini, M., Ajili, L., Faist, J., Beere, H., Ritchie, D.: Dual-wavelength THz imaging with quantum cascade lasers. *Proc. SPIE* **5727**, 107–114 (2005)
35. Ariyawansa, G., Apalkov, V., Perera, A.G.U., Matsik, S.G., Huang, G., Bhattacharya, P.: Bias-selectable tricolor tunneling quantum dot infrared photodetector for atmospheric windows. *Appl. Phys. Lett.* **92**, 111104-1–111104-3 (2008)
36. Kock, A., Gornik, E., Abstreiter, G., Böhm, G., Walther, M., Weimann, G.: Double wavelength selective GaAs/AlGaAs infrared detector device. *Appl. Phys. Lett.* **60**, 2011–2013 (1992)
37. Gravié, I., Shakouri, A., Kruze, N., Yariv, A.: Voltage-controlled tunable GaAs/AlGaAs multistack quantum well infrared photodetector. *Appl. Phys. Lett.* **60**, 2362–2364 (1992)
38. Liu, H.C., Li, J., Thompson, J.R., Wasilewski, Z.R., Buchanan, M., Simmons, J.G.: Multicolor voltage-tunable quantum-well infrared photodetector. *IEEE Electron Device Lett.* **14**, 566–568 (1993)

39. Tidrow, M.Z., Chiang, J.C., Li, S.S., Bacher, K.: A high strain two-stack two-color quantum well infrared photodetector. *Appl. Phys. Lett.* **70**, 859–861 (1997)
40. Tsai, K.L., Chang, K.H., Lee, C.P., Huang, K.F., Tsang, J.S., Chen, H.R.: Two-color infrared photodetector using GaAs/AlGaAs and strained InGaAs/AlGaAs multiquantum wells. *Appl. Phys. Lett.* **62**, 3504–3506 (1993)
41. Wang, Y.H., Chiang, J.C., Li, S.S., Ho, P.: A GaAs/AlAs/AlGaAs and GaAs/AlGaAs stacked quantum well infrared photodetector for 3–5 and 8–14 μm detection. *J. Appl. Phys.* **76**, 2538–2540 (1994)
42. Zhang, Y., Jiang, D.S., Xia, J.B., Cui, L.Q., Song, C.Y., Zhou, Z.Q., Ge, W.K.: A voltage-controlled tunable two-color infrared photodetector using GaAs/AlAs/GaAlAs and GaAs/GaAlAs stacked multiquantum wells. *Appl. Phys. Lett.* **68**, 2114–2116 (1996)
43. Beck, W.A., Faska, T.S.: Current status of quantum well focal plane arrays. In: *Proceedings of the SPIE, infrared technology and applications XXII*, vol. 2744, pp. 193–206 (1996)
44. Berger, V., Vojjdani, N., Bois, P., Vinter, B., Delaitre, S.: Switchable bicolor infrared detector using an electron transfer infrared modulator. *Appl. Phys. Lett.* **61**, 1898–1900 (1992)
45. Martinet, E., Rosencher, E., Luc, F., Bois, P., Costard, E., Delaitre, S.: Switchable bicolor (5.5–9.0 μm) infrared detector using asymmetric GaAs/AlGaAs multiquantum well. *Appl. Phys. Lett.* **61**, 246–248 (1992)
46. Chiang, J.C., Li, S.S., Tidrow, M.Z., Ho, P., Tsai, M., Lee, C.P.: A voltage-tunable multicolor triple-coupled InGaAs/GaAs/AlGaAs quantum-well infrared photodetector for 8–12 μm detection. *Appl. Phys. Lett.* **69**, 2412–2414 (1996)
47. Schneider, H., Liu, H.C., Winnerl, S., Song, C.Y., Drachenko, O., Walther, M., Faist, J., Helm, M.: Quadratic detection with two-photon quantum well infrared photodetectors. *Infrared Phys. Tech.* **52**, 419–423 (2009)
48. Schneider, H., Liu, H.C., Winnerl, S., Song, C.Y., Walther, M., Helm, M.: Terahertz two-photon quantum well infrared photodetector. *Opt. Express* **17**(15), 12279–12284 (2009)
49. Rosencher, E., Fiore, A., Vinter, B., Berger, V., Bois, P.h., Nagle, J.: Quantum engineering of optical nonlinearities. *Science* **271**, 168–173 (1996)
50. Schneider, H., Maier, T., Liu, H.C., Walther, M., Koidl, P.: Ultra-sensitive femtosecond two-photon detector with resonantly enhanced nonlinear absorption. *Opt. Lett.* **30**, 287–289 (2005)
51. Maier, T., Schneider, H., Walther, M., Koidl, P., Liu, H.C.: Resonant two-photon photoemission in quantum well infrared photodetectors. *Appl. Phys. Lett.* **84**, 5162–5164 (2004)
52. Schneider, H., Liu, H.C.: *Quantum Well Infrared Photodetectors: Physics and Applications*. Springer, Berlin (2006)
53. Cristea, P., Fedoryshyn, Y., Holzman, J.F., Robin, F., Jäckel, H., Müller, E., Faist, J.: Tuning the intersubband absorption in strained AlAsSb/InGaAs quantum wells towards the telecommunications wavelength range. *J. Appl. Phys.* **100**, 116104-1–116104-3 (2006)
54. Luo, H., Liu, H.C., Song, C.Y., Wasilewski, Z.R.: Background-limited terahertz quantum-well photodetector. *Appl. Phys. Lett.* **86**, 231103-1–231103-3 (2005)
55. Tonouchi, M.: Cutting-edge terahertz technology. *Nat. Photon.* **1**, 97–105 (2007)
56. Liu, H.C., Song, C.Y., Wasilewski, Z.R., Gupta, J.A., Buchanan, M.: Fano resonance mediated by intersubband-phonon coupling. *Appl. Phys. Lett.* **91**, 131121-1–131121-3 (2007)
57. Schneider, H., Drachenko, O., Winnerl, S., Helm, M., Walther, M.: Quadratic autocorrelation of free-electron laser radiation and photocurrent saturation in two-photon quantum-well infrared photodetectors. *Appl. Phys. Lett.* **89**, 133508-1–133508-3 (2006)
58. Stier, O., Grundmann, M., Bimberg, D.: Electronic and optical properties of strained quantum dots modeled by 8-band $k\cdot p$ theory. *Phys. Rev. B* **59**, 5688–5701 (1999)
59. Sun, S.J., Chang, Y.C.: Modeling self-assembled quantum dots by the effective bond-orbital method. *Phys. Rev. B* **62**, 13631–13640 (2000)

60. Ryzhii, V.: Negative differential photoconductivity in quantum-dot infrared photodetectors. *Appl. Phys. Lett.* **78**, 3346–3348 (2001)
61. Boucaud, P., Sauvage, S.: Infrared photodetection with semiconductor self-assembled quantum dots. *C. R. Phys.* **4**, 1133–1154 (2003)
62. Xu, S.J., et al.: Characteristics of InGaAs quantum dot infrared photodetectors. *Appl. Phys. Lett.* **73**, 3153–3155 (1998)
63. Blick, R.H., Haug, R.J., Weis, J., Pfannkuche, D., Klitzing, K.V., Eberl, K.: Single-electron tunneling through a double quantum dot: the artificial molecule. *Phys. Rev. B* **53**, 7899–7902 (1996)
64. Sikorski, C., Merkt, U.: Spectroscopy of electronic states in InSb quantum dots. *Phys. Rev. Lett.* **62**, 2164–2167 (1989)
65. Demel, T., Heitmann, D., Grambow, P., Ploog, K.: Nonlocal dynamic response and level crossings in quantum-dot structures. *Phys. Rev. Lett.* **64**, 788–791 (1990)
66. Stranski, I.N., Krastanov, L.: Zur Theorie der orientierten Ausscheidung von Ionenkristallen aufeinander. *Sitzungsber. Akad. Wiss. Wien, Math. Naturwiss. K1 Abt. 2B* **146**, 797–810 (1938)
67. Goldstein, L., Glas, F., Marzin, J.Y., Charasse, M.N., Le Roux, G.: Growth by molecular beam epitaxy and characterization of InAs/GaAs strained-layer superlattices. *Appl. Phys. Lett.* **47**, 1099–1101 (1985)
68. Mo, Y.W., Savage, D.E., Swartzentruber, B.S., Lagally, M.G.: Kinetic pathway in Stranski–Krastanov growth of Ge on Si(001). *Phys. Rev. Lett.* **65**, 1020–1023 (1990)
69. Gérard, J.M., Marzin, J.Y., Zimmermann, G., Ponchet, A., Cabrol, O., Barrier, D., Jusserand, B., Sermage, B.: InAs/GaAs quantum boxes obtained by self-organized growth: intrinsic electronic properties and applications. *Solid State Electron.* **40**, 807–814 (1996)
70. Grundmann, M., Stier, O., Bimberg, D.: InAs/GaAs pyramidal quantum dots: strain distribution, optical phonons, and electronic structure. *Phys. Rev. B* **52**, 11969–11981 (1995)
71. Lee, H., Lowe-Webb, R., Yang, W., Sercel, P.C.: Determination of the shape of self-organized InAs/GaAs quantum dots by reflection high energy electron diffraction. *Appl. Phys. Lett.* **72**, 812–814 (1998)
72. Haller, E.E.: Advanced far-infrared detectors. *Infrared Phys.* **35**, 127–146 (1994)
73. Suzuki, M., Tonouchi, M.: Fe-implanted InGaAs photoconductive terahertz detectors triggered by 1.56 μm femtosecond optical pulses. *Appl. Phys. Lett.* **86**, 163504-1–163504-3 (2005)
74. Rinzan, M.B.M., Perera, A.G.U., Matsik, S.G., Liu, H.C., Wasilewski, Z., Buchanan, M.: AlGaAs emitter/GaAs barrier terahertz detector with a 2.3 THz threshold. *Appl. Phys. Lett.* **86**, 071112-1–071112-3 (2005)
75. Lü, J., Shur, M.S.: Terahertz detection by high-electron-mobility transistor: enhancement by drain bias. *Appl. Phys. Lett.* **78**, 2587–2588 (2001)
76. Liu, H.C., Song, C.Y., Spring Thorpe, A.J., Cao, J.C.: Terahertz quantum-well photodetector. *Appl. Phys. Lett.* **84**, 4068–4070 (2004)
77. Phillips, J., Bhattacharya, P., Kennerly, S.W., Beekman, D.W., Dutta, M.: Self-assembled InAs–GaAs quantum-dot intersubband detectors. *IEEE J. Quantum Electron.* **35**, 936–943 (1999)
78. Kim, E., Madhukar, A., Ye, Z., Campbell, J.C.: High detectivity InAs quantum dot infrared photodetectors. *Appl. Phys. Lett.* **84**, 3277–3279 (2004)
79. Krishna, S., Raghavan, S., Von Winckel, G., Stintz, A., Ariyawansa, G., Matsik, S.G., Perera, A.G.U.: Three-color (λ_{p1} 3.8 μm , λ_{p2} 8.5 μm , and λ_{p3} 23.2 μm) InAs/InGaAs quantum-dots-in-a-well detector. *Appl. Phys. Lett.* **83**, 2745–2747 (2003)
80. Chakrabarti, S., Stiff-Roberts, A.D., Bhattacharya, P., Gunapala, S.D., Bandara, S., Rafol, S.B., Kennerly, S.W.: High-temperature operation of InAs/GaAs quantum dot infrared photodetectors with large responsivity and detectivity. *IEEE Photonics Technol. Lett.* **16**, 1361–1363 (2004)

81. Berryman, K.W., Lyon, S.A., Segev, M.: Mid-infrared photoconductivity in InAs quantum dots. *Appl. Phys. Lett.* **70**, 1861–1863 (1997)
82. Liu, J.L., Wu, W.G., Balandin, A., Jin, G.L., Wang, K.L.: Intersubband absorption in boron-doped multiple Ge quantum dots. *Appl. Phys. Lett.* **74**, 185–187 (1999)
83. Chua, Y.C., Decuir, E.A., Passmore, B.S., Sharif, K.H., Manasreha, M.O., Wang, Z.M., et al.: Tuning In_{0.3}Ga_{0.7}As/GaAs multiple quantum dots for long-wavelength infrared detectors. *Appl. Phys. Lett.* **85**, 1003–1005 (2004)
84. Chakrabarti, S., Bhattacharya, P., Stiff-Roberts, A.D., Lin, Y.Y., Singh, J., Lei, Y., et al.: Intersubband absorption in annealed InAs/GaAs quantum dots: a case for polarization-sensitive infrared detection. *J. Phys. D Appl. Phys.* **36**, 1794–1797 (2003)
85. Barseghyan, M.G., Kirakosyan, A.A.: Light absorption by a two-dimensional quantum dot superlattice. *Physica E* **27**, 474–480 (2005)
86. Etteh, N.E.I., Harrison, P.: Carrier scattering approach to the origins of dark current in mid and far-infrared (terahertz) quantum-well intersubband photodetectors (QWLPs). *IEEE J. Quantum Electron.* **37**, 672–675 (2001)
87. Phillips, J., Kamath, K., Bhattacharya, P.: Characteristics of InAs/AlGaAs self-organized quantum dot modulation doped field effect transistors. *Appl. Phys. Lett.* **72**, 3509–3511 (1998)
88. Kim, S., Mohseni, H., Erdtmann, M., Michel, E., Jelen, C., Razeghi, M.: Growth and characterization of InGaAs/InGaP quantum dots for midinfrared photoconductive detector. *Appl. Phys. Lett.* **73**, 963–965 (1998)
89. Pan, D., Towe, E., Kennerly, S.: A five-period normal-incidence (In, Ga)As/GaAs quantum-dot infrared photodetector. *Appl. Phys. Lett.* **75**, 2719–2721 (1999)
90. Kim, J.W., Oh, J.E., Hong, S.C., Park, C.H., Yoo, T.K.: Room temperature far infrared ($8 \sim 10 \mu\text{m}$) photodetectors using self-assembled InAs quantum dots with high detectivity. *IEEE Electron. Device Lett.* **21**, 329–331 (2000)
91. Liu, H.C., Gao, M., McCaffrey, J., Wasilewski, Z.R., Fafard, S.: Quantum dot infrared photodetectors. *Appl. Phys. Lett.* **78**, 79–81 (2001)
92. Stiff, A.D., Krishna, S., Bhattacharya, P., Kennerly, S.W.: Normal-incidence, high-temperature, mid-infrared, InAs-GaAs vertical quantum-dot infrared photodetector. *IEEE J. Quantum Electron.* **37**, 1412–1419 (2001)
93. Stiff, A.D., Krishna, S., Bhattacharya, P., Kennerly, S.: High-detectivity, normal-incidence, mid-infrared ($\lambda \sim 4 \mu\text{m}$) InAs/GaAs quantum-dot detector operating at 150 K. *Appl. Phys. Lett.* **79**, 421–423 (2001)
94. Ye, Z., Campbell, J.C., Chen, Z., Kim, E., Madhukar, A.: Normal-incidence InAs self-assembled quantum-dot infrared photodetectors with a high detectivity. *IEEE J. Quantum Electron.* **38**, 1234–1237 (2002)
95. Ye, Z., Campbell, J.C., Chen, Z., Kim, E.T., Madhukar, A.: InAs quantum dot infrared photodetectors with In_{0.15}Ga_{0.85}As strain-relief cap layers. *J. Appl. Phys.* **92**, 7462–7468 (2002)
96. Lee, S.W., Hirakawa, K., Shimada, Y.: Bound-to-continuum intersubband photoconductivity of self-assembled InAs quantum dots in modulation-doped heterostructures. *Appl. Phys. Lett.* **75**, 1428–1430 (1999)
97. Chu, L., Zrenner, A., Bichler, M., Abstreiter, G.: Quantum-dot infrared photodetector with lateral carrier transport. *Appl. Phys. Lett.* **79**, 2249–2251 (2001)
98. Hsu, B.C., Chang, S.T., Chen, T.C., Kuo, P.S., Chen, P.S., Pei, Z., et al.: A high efficient 820 nm MOS Ge quantum dot photodetector. *IEEE Electron. Device Lett.* **24**, 318–320 (2003)
99. Su, X.H., Yang, J., Bhattacharya, P., Ariyawansa, G., Perera, A.G.U.: Terahertz detection with tunneling quantum dot intersublevel photodetector. *Appl. Phys. Lett.* **89**, 031117-1–031117-3 (2006)
100. Esaev, D.G., Rinzan, M.B.M., Matsik, S.G., Perera, A.G.U., Liu, H.C., Zvonkov, B.N., Gavrilenko, V.I., Belyanin, A.A.: High performance single emitter homojunction interfacial workfunction far infrared detectors. *J. Appl. Phys.* **95**, 512–519 (2004)

101. Hofer, S., Hirner, H., Bratschitsch, R., Strasser, G., Unterrainer, K.: Photoconductive response of InAs/GaAs quantum dot stacks. *Physica E* **13**, 190–193 (2002)
102. Grundmann, M., Weber, A., Goede, K., Ustinov, V.M., Zhukov, A.E., Ledentsov, N.N., Kop'ev, P.S., Alferov, Z.I.: Midinfrared emission from near-infrared quantum-dot lasers. *Appl. Phys. Lett.* **77**, 4–6 (2000)
103. Wingreen, N.S., StaLord, C.A.: Quantum-dot cascade laser: proposal for an ultralow-threshold semiconductor laser. *J. Quantum Electron.* **33**, 1170–1173 (1997)
104. Bayer, M., Hawrylak, P., Hinzer, K., Fafard, S., Korkusinski, M., Wasilewski, R., Stern, O., Forchel, A.: Coupling and entangling of quantum states in quantum dot molecules. *Science*. **291**, 451–453 (2001)
105. Bastard, G.: Theoretical investigations of superlattice band structure in the envelope-function approximation. *Phys. Rev. B* **25**, 7584–7597 (1982)
106. Pan, D., Towe, E., Kennerly, S.: Normal-incidence intersubband (In, Ga)As/GaAs quantum dot infrared photodetectors. *Appl. Phys. Lett.* **73**, 1937–1939 (1998)
107. Chu, L., Zrenner, A., Bohm, G., Abstreiter, G.: Normal-incident intersubband photocurrent spectroscopy on InAs/GaAs quantum dots. *Appl. Phys. Lett.* **75**, 3599–3601 (1999)
108. Yu, L.S., Li, S.S.: A metal grating coupled bound-to-miniband transition GaAs multiquantum well/superlattice infrared detector. *Appl. Phys. Lett.* **59**, 1332–1334 (1991)
109. Yu, L.S., Wang, H., Li, S.S., Ho, P.: Low dark current step-bound-to-miniband transition InGaAs/GaAs/AlGaAs multiquantum-well infrared detector. *Appl. Phys. Lett.* **60**, 992–994 (1992)
110. Carr, G.L., Martin, M.C., McKinney, W.R., Jordan, K., Neil, G.R., Williams, G.P.: High-power terahertz radiation from relativistic electrons. *Nat.* **420**, 153–156 (2002)
111. Sherwin, M.: Terahertz power. *Nat.* **420**, 131–133 (2002)
112. Mittleman, D.M., Jacobsen, R.H., Nuss, M.C.: T-Ray imaging'. *IEEE J. Select. Topics. Quantum Electronics*. **2**, 679–692 (1996)
113. Siegel, P.H.: Terahertz technology in biology and medicine. *IEEE Tran. Microwave. Theory and Techniques* **52**, 2438–2447 (2004)
114. Siegel, P.H.: THz applications for outer and inner space. In: 17th International Zurich Symposium on Electromagnetic Compatibility, 1–4 (2006)
115. Dai, J.H., Lee, J.H., Lee, S.C.: Annealing effect on the formation of In(Ga)As quantum rings from InAs quantum dots. *IEEE Photon. Technol. Lett.* **20**, 165–167 (2008)
116. Lee, J.H., Dai, J.H., Chang, Y.T., Chan, C.F., Lee, S.C.: In(Ga)As quantum ring terahertz photodetector. *Solid State Devices and Materials (SSDM 2008)*. Ibaraki, Japan (2008)
117. Kochman, B., Stiff-Roberts, A.D., Chakrabarti, S., Phillips, J.D., Krishna, S., Singh, J., et al.: Absorption, carrier lifetime, and gain in InAs–GaAs quantum-dot infrared photodetectors. *IEEE J. Quantum Electron.* **39**, 459–467 (2003)
118. Ryzhii, V., Khmyrova, I., Ryzhii, M., Mitin, V.: Comparison of dark current, responsivity and detectivity in different intersubband infrared photodetectors. *Semicond. Sci. Technol.* **19**, 8–16 (2004)
119. Rostami, A., Rasooli Saghahi, H.: A novel proposal for ultra-high optical nonlinearity in GaN/AlGaIn spherical centered defect quantum dot (SCDQD). *Microelectron. J.* **38**, 342–351 (2007)
120. Rostami, A., Rasooli Saghahi, H., Sadoogi, N., Baghban, H.: Proposal for ultra-high performance infrared quantum dot. *Opt. Express* **16**, 2752–2763 (2008)
121. Rostami, A., Rasooli Saghahi, H., Baghban, H.: A proposal for enhancement of absorption coefficient and electroabsorption properties in GaN/AlGaIn centered defect quantum box (CDQB) nanocrystal. *Phys. B* **403**, 2789–2796 (2008)
122. Rostami, A., Rasooli Saghahi, H., Baghban, H.: A proposal for enhancement of optical nonlinearity in GaN/AlGaIn centered defect quantum box (CDQB) nanocrystal. *Solid State Electron.* **52**, 1075–1081 (2008)
123. Sadoogi, N., Rasooli Saghahi, H., Rostami, A., Ghafoori Fard, H.: Electron transport in array of centered defect quantum dots. *Phys. E* **41**, 269–277 (2008)

124. Harrison, P., Gadir, M.A., Etteh, N.E.I., Soref, R.A.: The physics of THz QWIPs. In: Proceedings of the 9th international conference on THz electronics, the 10th IEEE international conference on terahertz electronics (2002)
125. Rasooli Saghai, H., Sadoogi, N., Rostami, A., Baghban, H.: Ultra-high detectivity room temperature THz IR-photodetector based on resonant tunneling spherical centered defect quantum dot (RT-SCDQD). *Optic. Comm.* **282**, 3499–3508 (2009)
126. Rostami, A., Rasooli Saghai, H., Baghban Asghari Nejad, H., Sadoogi, N.: Tailoring of quantum dot basic cell towards high detectivity THz-IR photodetector. In: Luo, Y., Buus, J., Koyama, F., Lo, Y.-H. (eds.) *Optoelectronic Materials and Devices III*. Proc. of SPIE, vol. 7135, pp. 71352Z-1–71352Z-9 (2008)
127. Arfken, G.B., Weber, H.J.: *Mathematical Methods for Physicists*. Harcourt Academic Press, San Diego (2001)
128. Peyghambarian, N., Koch, S.W., Mysyrowicz, A.: *Introduction to Semiconductor Optics*. Prentice-Hall, Englewood Cliffs (1993)
129. Basu, P.K.: *Theory of Optical Processes in Semiconductors*. Clarendon Press, Oxford (1997)
130. Asgari, A., Kalafi, M., Faraone, L.: The effects of GaN capping layer thickness on two-dimensional electron mobility in GaN/AlGaIn/GaN heterostructures. *Phys. E* **25**, 431–437 (2005)
131. Guo, K.X., Yu, Y.B.: Nonlinear optical susceptibilities in Si/SiO₂ parabolic quantum dots. *Chin. J. Phys.* **43**, 932–940 (2005)
132. Liu, J., Bai, J., Xiong, G.: Studies of the second-order nonlinear optical susceptibilities of GaN/AlGaIn quantum well. *Phys. E* **23**, 70–74 (2004)
133. Adawi, A.M., Zibik, E.A., Wilson, L.R., Lemaitre, A., Cockburn, J.W., Skolnick, M.S., Hopkinson, M., et al.: Strong in-plane polarised intersublevel absorption in vertically aligned InGaAs/GaAs quantum dots. *Appl. Phys. Lett.* **82**, 3415–3417 (2003)
134. Kerr, W.E., Pancholi, A., Stoleru, V.G.: Quantum dot molecules: a potential pathway towards terahertz devices. *Phys. E* **35**, 139–145 (2006)
135. Paiella, R.: *Intersubband Transitions in Quantum Structures*. McGraw-Hill, NY (2006)
136. Zyaei, M., Rasooli Saghai, H., Abbasian, K., Rostami, A.: Long wavelength infrared photodetector design based on electromagnetically induced transparency. *Optic. Comm.* **281**, 3739–3747 (2008)
137. Rostami, A., Zyaei, M., Rasooli Saghai, H.: Room temperature terahertz quantum well infrared photodetector based on electromagnetically induced transparency (EIT). In: Proceedings of the IASTED International Conference, Greece Nanotechnology and Application (NANA), vol. 615-050, pp. 95–100 (2008)
138. Rostami, A., Zyaei, M., Rasooli Saghai, H., Sharifi, F.J.: Terahertz asymmetric quantum well infrared photodetector design based on electromagnetically induced transparency. In: *Optomechatronic technologies*, SPIE, vol. 7266, pp. 72660Z-1–72660Z-9 (2008)
139. Harris, S.E.: Electromagnetically induced transparency. *Phys. Today* **50**(7), 36–42 (1997)
140. Scully, M.O., Zubairy, M.S.: *Quantum Optics*. Cambridge University Press, Cambridge (1997)
141. Phillips, C.C., Paspalakis, E., Serapiglia, G.B., Sirtori, C., Vodopyanov, K.L.: Observation of electromagnetically induced transparency and measurements of subband dynamics in a semiconductor quantum well. *Phys. E* **7**, 166–173 (2000)
142. Faist, J., Capasso, F., Sirtori, C., West, K., Pfeiffer, L.N.: Controlling the sign of quantum interference by tunnelling from quantum wells. *Nature* **390**, 589–591 (1997)
143. Schmidt, H., Campman, K.L., Gossard, A.C., Imamoglu, A.: Tunneling induced transparency: fano interference in intersubband transitions. *Appl. Phys. Lett.* **70**, 3455–3457 (1997)
144. Frogley, M.D., Dynes, J.F., Beck, M., Faist, J., Phillips, C.C.: Gain without inversion in semiconductor nanostructures. *Nat. Mater.* **5**, 175–178 (2006)
145. Schmidt, H., Imamoglu, A.: Nonlinear optical devices based on a transparency in semiconductor intersubband transitions. *Optic. Commun.* **131**, 333–338 (1996)

- 146. Lee, C.R., Li, Y.C., Men, F.K., Pao, C.H., Tsai, Y.C., Wang, J.F.: Model for an inversionless two-color laser. *Appl. Phys. Lett.* **86**, 201112-1–201112-3 (2004)
- 147. Dyns, J.F., Frogley, M.D., Rodger, J., Phillips, C.C.: Optically mediated coherent population trapping in asymmetric semiconductor quantum wells. *Phys. Rev. B* **72**, 085323-1–085323-7 (2005)
- 148. Giorgetta, F.R., Baumann, A.E., Hofstetter, D., Manz, C., Yang, Q., Köhler, K., Graf, M.: InGaAs/AlAsSb quantum cascade detectors operating in the near infrared. *Appl. Phys. Lett.* **91**, 111115-1–111115-3 (2007)
- 149. Yelin, S.F., Hemmer, P.R.: Resonantly enhanced nonlinear optics in semiconductor quantum wells: an application to sensitive infrared detection. *Phys. Rev. A* **66**, 013803-1–013803-5 (2002)
- 150. Fleischhauer, M., Imamoglu, A., Marangos, J.P.: Electromagnetically induced trans



<http://www.springer.com/978-3-642-15792-9>

Terahertz Technology

Fundamentals and Applications

Rostami, A.; Rasooli, H.; Baghban, H.

2011, XIV, 246 p., Hardcover

ISBN: 978-3-642-15792-9